

TRAPPING AND SORTING OF CIRCULATING TUMOR CELLS IN A MICROFLUIDIC FILTER ARRAY

by

Saeedur Rahman
(1015102072)

Submitted in partial fulfilment of the requirements for the degree of Master of
Science in Mechanical Engineering

Under the supervision of

Dr. A.B.M. Toufique Hasan

Professor

Department of Mechanical Engineering

Bangladesh University of Engineering and Technology (BUET)

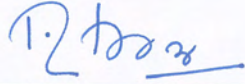


DEPARTMENT OF MECHANICAL ENGINEERING
BANGLADESH UNIVERSITY OF ENGINEERING AND TECHNOLOGY (BUET)
DHAKA-1000, BANGLADESH

September, 2021

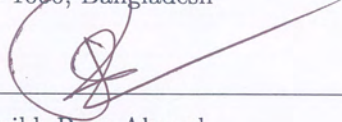
Certificate of Approval

The thesis titled "Trapping and Sorting of Circulating Tumor Cells in a Microfluidic Filter Array", submitted by Saeedur Rahman, Student No.: 1015102072, Session: October-2015, has been accepted as satisfactory in partial fulfillment of the degree of Master of Science in Mechanical Engineering on September 29, 2021.



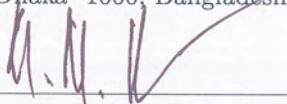
Dr. A.B.M. Toufique Hasan
Professor
Department of Mechanical Engineering
Bangladesh University of Engineering and Technology
Dhaka- 1000, Bangladesh

Chairman
(Supervisor)



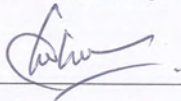
Dr. Shaikh Reaz Ahmed
Professor and Head
Department of Mechanical Engineering
Bangladesh University of Engineering and Technology
Dhaka- 1000, Bangladesh

Member
(Ex-Officio)



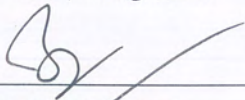
Dr. Muhammed Mahbubur Razaque
Professor
Department of Mechanical Engineering
Bangladesh University of Engineering and Technology
Dhaka- 1000, Bangladesh

Member



Dr. Mohammad Mamun
Professor
Department of Mechanical Engineering
Bangladesh University of Engineering and Technology
Dhaka- 1000, Bangladesh

Member



Dr. A.K.M. Sadrul Islam
Professor (Retired)
Department of Mechanical Engineering
Bangladesh University of Engineering and Technology, Dhaka
Apt. A4, House No. 110, Road 9/A, Dhanmondi
Dhaka- 1209, Bangladesh

Member
(External)

Candidate's Declaration

This is hereby declared that this thesis or any part of this thesis has not been submitted elsewhere for award of any degree or diploma.

Saeedur Rahman

Saeedur Rahman

Dedication

To my family

Acknowledgements

Praise be to the Almighty Allah for all the blessings He has bestowed upon us.

I want to express heartfelt gratitude to my supervisor Dr. A.B.M. Toufique Hasan, for his unwavering patience and support throughout this study. This work would not have come to fruition without his guidance.

I would like to thank the Head of the Department of Mechanical Engineering, BUET, for the approval to carry out this research work. I would also like to extend my gratitude to the Head of the Department of Biomedical Engineering, BUET, for the access to the computational facilities. Furthermore, I would like to thank my colleagues at the Department of Biomedical Engineering, BUET, for their continuous support, inspiration, and cooperation.

Last but not least, I would like to acknowledge the love and the sacrifices of my family members throughout my life.

Abstract

The presence and enumeration of Circulating Tumor Cells (CTCs) in peripheral blood has been identified as an indicator for early detection and treatment efficacy of various forms of cancer. Physical property-based isolation techniques of CTCs by microfluidic filters have emerged as a method capable of providing viable cells suitable for further study. Numerical simulations of a cell passing through microfilters provide insight into cell deformation and filter device operating characteristics. In this study, a microfluidic filter array device is proposed to sort the CTCs according to their physical properties along with isolation. The array device consists of three conical filter funnels having decreasing pore size connected in series. Cell passage through the filter funnels was computationally simulated by two-phase fluid flow with the cell modeled as a Newtonian droplet having constant cortical tension and viscosity. The CTCs were considered to be suspended in the blood plasma medium. Cell trapping and sorting phenomena in the filter array device based on cell size and cortical tension were investigated for different filter inlet driving pressures. The properties were selected to reflect the physical properties of RT4 bladder cancer cell, nontumorigenic breast cell MCF-10A and breast cancer cells MDA-MB-231 and MDA-MB-468. CTCs were found to be trapped and sorted in the filter funnels according to their physical properties. Stiffer and larger cells were trapped early in funnels within a larger pore radius. Whereas softer and smaller cells can travel forward to be trapped in funnels with smaller pore sizes. An increase in the driving pressure resulted in a different sorting pattern, with all the cells being able to move further towards smaller funnels. Some of the cells passed through all the funnels to the exit chamber. Cell deformation in funnels was also quantified to show larger deformation in funnels with smaller pore radius. To characterize the filter array device, the threshold pressure required for passing through filters of different pore sizes was also investigated. The threshold pressure showed variation with filter pore size and cell physical properties. Smaller-sized filter funnels were found to require higher pressure to pass. The threshold pressure was also high for cells with large size and cortical tension. Based on the threshold passing pressures, filter characteristics were established to show that for a given filter geometry, different inlet driving pressure can be used to sort CTCs by different ranges of physical properties. The results provide a framework to customize microfluidic filter array device design and operation for selective detection and physical property-based sorting of CTCs, which have significant clinical importance in cancer diagnosis and treatment.

Contents

Abstract	v
List of Figures	viii
List of Tables	xiii
Glossary	xiv
1 Introduction	1
1.1 Background	1
1.2 CTC detection: literature review	4
1.3 Objectives	14
1.4 Organization of the thesis	14
2 Physical Model and Numerical Method	15
2.1 Problem description	15
2.1.1 Physical properties of tumor cells	15
2.1.2 Modeling of cell behavior	17
2.1.3 CTC filter construction	18
2.1.4 Filter geometry	19
2.1.5 Computational parameters	20
2.2 Governing equations	22
2.3 Boundary conditions	24
2.3.1 Inlet boundary conditions	24
2.3.2 Wall boundary condition	26
2.3.3 Outlet boundary condition	26
2.3.4 Axis boundary condition	27
2.4 Cortical tension modeling	27
2.4.1 Wall adhesion	29
2.5 Numerical simulation	29
2.5.1 Pressure-based segregated algorithm	30
2.5.2 Spatial discretization	31
2.5.3 Pressure velocity coupling	34
2.5.4 Temporal Discretization	34
2.6 Interface capturing	35
2.6.1 The VOF model	35

2.6.1.1	The volume fraction equation	36
2.6.2	The geometric reconstruction scheme	37
2.7	Discretization of the computational domain	38
2.8	Validation and verification	39
3	CTC Isolation and Sorting by Pressure Driven Flow	43
3.1	CTC passing phenomena in a filter funnel: deformability analysis	43
3.1.1	CTC deformation under constant flow rate	43
3.1.2	CTC deformation in pressure driven flow	44
3.2	CTC trapping in a microfluidic filter array	46
3.3	Quantification of cell deformation	81
3.4	Cell sorting and trapping in filter array	83
4	Establishment of Filter Characteristics from Threshold CTC Passing Pressure	86
4.1	Pressure signatures for CTC passing through a filter funnel	86
4.2	Threshold pressure dependence on filter geometry and cell physical property	105
4.3	Establishment of filter characteristics	108
5	Conclusions	112
5.1	Summary	112
5.2	Contributions	114
5.3	Possible application of the filter array device	115
5.4	Limitations and scope of future work	116
	Bibliography	117

List of Figures

1.1	Size distribution of blood cells and comparison with CTCs [14].	4
1.2	Principle of deterministic lateral displacement where small particles can follow the streamline around obstacles but large particles get shifted to different streamlines and are separated [29].	6
1.3	Design and principle of vortex based chip from [46]. Larger cells are trapped in the camber. The bottom row shows separation of cancer cells.	7
1.4	Membrane filters showing micropores with the bottom row showing captured human prostate adenocarcinoma LNCaP cells [47].	8
1.5	(a) Schematic of the microfluidic filter device used by [51] showing varying channel gaps, (b) Capturing of MDA-MB-231, SW620 and HEK293 cells which have different physical properties.	11
1.6	(a) Schematic and design principle of the device used by [45] that separates CTCs using Dean Flow Fractionation (DFF), (b) MCF-7 cells in their focusing position in the microchannel.	12
1.7	(a) Schematic of the ratchet cell sorting device used by [62], (b) separation of larger and stiff UC13 cancer cells from smaller and deformable leukocytes. Leukocytes traelled to the top while UC13 cells are trapped at the bottom.	13
2.1	(a) 3D physical model of single filter, (b) 2D sketch showing geometric parameters.	19
2.2	(a) 3D physical model of filter array, (b) 2D sketch showing dimensions in μm	21
2.3	Boundary conditions.	25
2.4	Overview of the pressure based segregated algorithm.	31
2.5	Control volume for illustrating spatial discretization of the momentum equation.	32
2.6	Interface calculation by the geometric reconstruction scheme.	38
2.7	Mesh of the filter array computational domain.	39
2.8	Comparison of threshold pressure required to deform a blood granulocyte.	40
2.9	(a) Inlet pressure history for grids of three different resolution, (b) Calculated range of convergence.	41

3.1	Pressure-deformability behavior of a CTC passing through a single conical microfilter. Insets a- e shows cell deformation states at various instants.	45
3.2	Flow rate-deformability behavior of a CTC passing through a single conical microfilter. Insets a- f shows cell deformation states at various instants.	46
3.3	(a) flow rate and cell position history for the case: $P_{in} = 100$ Pa, $\sigma = 0.2$ mN/m and $D = 16$ μ m, (b)-(h) cell volume fraction showing cell position and deformation at different times during passage through the filter. (cont.)	49
3.3	(a) flow rate and cell position history for the case: $P_{in} = 100$ Pa, $\sigma = 0.2$ mN/m and $D = 16$ μ m, (b)-(h) cell volume fraction showing cell position and deformation at different times during passage through the filter.	50
3.4	(a) flow rate and cell position history for the case: $P_{in} = 300$ Pa, $\sigma = 0.2$ mN/m and $D = 16$ μ m, (b)-(h) cell volume fraction showing cell position and deformation at different times during passage through the filter. (cont.)	51
3.4	(a) flow rate and cell position history for the case: $P_{in} = 300$ Pa, $\sigma = 0.2$ mN/m and $D = 16$ μ m, (b)-(h) cell volume fraction showing cell position and deformation at different times during passage through the filter.	52
3.5	(a) flow rate and cell position history for the case: $P_{in} = 100$ Pa, $\sigma = 0.4$ mN/m and $D = 20$ μ m, (b)-(h) cell volume fraction showing cell position and deformation at different times during passage through the filter. (cont.)	53
3.5	(a) flow rate and cell position history for the case: $P_{in} = 100$ Pa, $\sigma = 0.4$ mN/m and $D = 20$ μ m, (b)-(h) cell volume fraction showing cell position and deformation at different times during passage through the filter.	54
3.6	(a) flow rate and cell position history for the case: $P_{in} = 300$ Pa, $\sigma = 0.4$ mN/m and $D = 20$ μ m, (b)-(h) cell volume fraction showing cell position and deformation at different times during passage through the filter. (cont.)	55
3.6	(a) flow rate and cell position history for the case: $P_{in} = 300$ Pa, $\sigma = 0.4$ mN/m and $D = 20$ μ m, (b)-(h) cell volume fraction showing cell position and deformation at different times during passage through the filter.	56
3.7	(a) flow rate and cell position history for the case: $P_{in} = 100$ Pa, $\sigma = 1.1$ mN/m and $D = 16$ μ m, (b)-(h) cell volume fraction showing cell position and deformation at different times during passage through the filter. (cont.)	57
3.7	(a) flow rate and cell position history for the case: $P_{in} = 100$ Pa, $\sigma = 1.1$ mN/m and $D = 16$ μ m, (b)-(h) cell volume fraction showing cell position and deformation at different times during passage through the filter.	58

3.8	(a) flow rate and cell position history for the case: $P_{in} = 300$ Pa, $\sigma = 1.1$ mN/m and $D = 16$ μ m, (b)-(h) cell volume fraction showing cell position and deformation at different times during passage through the filter. (cont.)	59
3.8	(a) flow rate and cell position history for the case: $P_{in} = 300$ Pa, $\sigma = 1.1$ mN/m and $D = 16$ μ m, (b)-(h) cell volume fraction showing cell position and deformation at different times during passage through the filter.	60
3.9	(a) flow rate and cell position history for the case: $P_{in} = 100$ Pa, $\sigma = 2$ mN/m and $D = 12$ μ m, (b)-(h) cell volume fraction showing cell position and deformation at different times during passage through the filter. (cont.)	61
3.9	(a) flow rate and cell position history for the case: $P_{in} = 100$ Pa, $\sigma = 2$ mN/m and $D = 12$ μ m, (b)-(h) cell volume fraction showing cell position and deformation at different times during passage through the filter.	62
3.10	(a) flow rate and cell position history for the case: $P_{in} = 300$ Pa, $\sigma = 2$ mN/m and $D = 12$ μ m, (b)-(h) cell volume fraction showing cell position and deformation at different times during passage through the filter. (cont.)	63
3.10	(a) flow rate and cell position history for the case: $P_{in} = 300$ Pa, $\sigma = 2$ mN/m and $D = 12$ μ m, (b)-(h) cell volume fraction showing cell position and deformation at different times during passage through the filter.	64
3.11	(a) flow rate and cell position history for the case: $P_{in} = 100$ Pa, $\sigma = 0.2$ mN/m and $D = 12$ μ m, (b)-(c) cell volume fraction showing cell position and deformation at the initial and final time.	65
3.12	(a) flow rate and cell position history for the case: $P_{in} = 300$ Pa, $\sigma = 0.2$ mN/m and $D = 12$ μ m, (b)-(c) cell volume fraction showing cell position and deformation at the initial and final time.	66
3.13	(a) flow rate and cell position history for the case: $P_{in} = 100$ Pa, $\sigma = 0.2$ mN/m and $D = 20$ μ m, (b)-(c) cell volume fraction showing cell position and deformation at the initial and final time.	67
3.14	(a) flow rate and cell position history for the case: $P_{in} = 300$ Pa, $\sigma = 0.2$ mN/m and $D = 20$ μ m, (b)-(c) cell volume fraction showing cell position and deformation at the initial and final time.	68
3.15	(a) flow rate and cell position history for the case: $P_{in} = 100$ Pa, $\sigma = 0.4$ mN/m and $D = 12$ μ m, (b)-(c) cell volume fraction showing cell position and deformation at the initial and final time.	69
3.16	(a) flow rate and cell position history for the case: $P_{in} = 300$ Pa, $\sigma = 0.4$ mN/m and $D = 12$ μ m, (b)-(c) cell volume fraction showing cell position and deformation at the initial and final time.	70
3.17	(a) flow rate and cell position history for the case: $P_{in} = 100$ Pa, $\sigma = 0.4$ mN/m and $D = 16$ μ m, (b)-(c) cell volume fraction showing cell position and deformation at the initial and final time.	71

3.18	(a) flow rate and cell position history for the case: $P_{in} = 300$ Pa, $\sigma = 0.4$ mN/m and $D = 16$ μ m, (b)-(c) cell volume fraction showing cell position and deformation at the initial and final time.	72
3.19	(a) flow rate and cell position history for the case: $P_{in} = 100$ Pa, $\sigma = 1.1$ mN/m and $D = 12$ μ m, (b)-(c) cell volume fraction showing cell position and deformation at the initial and final time.	73
3.20	(a) flow rate and cell position history for the case: $P_{in} = 300$ Pa, $\sigma = 1.1$ mN/m and $D = 12$ μ m, (b)-(c) cell volume fraction showing cell position and deformation at the initial and final time.	74
3.21	(a) flow rate and cell position history for the case: $P_{in} = 100$ Pa, $\sigma = 1.1$ mN/m and $D = 20$ μ m, (b)-(c) cell volume fraction showing cell position and deformation at the initial and final time.	75
3.22	(a) flow rate and cell position history for the case: $P_{in} = 300$ Pa, $\sigma = 1.1$ mN/m and $D = 20$ μ m, (b)-(c) cell volume fraction showing cell position and deformation at the initial and final time.	76
3.23	(a) flow rate and cell position history for the case: $P_{in} = 100$ Pa, $\sigma = 2$ mN/m and $D = 16$ μ m, (b)-(c) cell volume fraction showing cell position and deformation at the initial and final time.	77
3.24	(a) flow rate and cell position history for the case: $P_{in} = 300$ Pa, $\sigma = 2$ mN/m and $D = 16$ μ m, (b)-(c) cell volume fraction showing cell position and deformation at the initial and final time.	78
3.25	(a) flow rate and cell position history for the case: $P_{in} = 100$ Pa, $\sigma = 2$ mN/m and $D = 20$ μ m, (b)-(c) cell volume fraction showing cell position and deformation at the initial and final time.	79
3.26	(a) flow rate and cell position history for the case: $P_{in} = 300$ Pa, $\sigma = 2$ mN/m and $D = 20$ μ m, (b)-(c) cell volume fraction showing cell position and deformation at the initial and final time.	80
3.27	Deformed length, l_d for quantifying cell deformation.	81
3.28	(a) Axial deformation, ϵ history for different cases: (a) $P_{in} = 100$ Pa and (b) $P_{in} = 300$ Pa.	83
3.29	Trapping and sorting of CTCs under (a) 100 Pa and (b) 300 Pa driving pressure.	84
4.1	(a) Inlet pressure signature for the case: $r_f = 6$ μ m, $\sigma = 0.2$ mN/m and $D = 16$ μ m, (b)-(i) cell volume fraction showing cell position and deformation at different times during passage through the filter. (cont.)	89
4.1	(a) Inlet pressure signature for the case: $r_f = 6$ μ m, $\sigma = 0.2$ mN/m and $D = 16$ μ m, (b)-(i) cell volume fraction showing cell position and deformation at different times during passage through the filter.	90
4.2	(a) Inlet pressure signature for the case: $r_f = 2$ μ m, $\sigma = 0.4$ mN/m and $D = 20$ μ m, (b)-(i) cell volume fraction showing cell position and deformation at different times during passage through the filter. (cont.)	91

4.2	(a) Inlet pressure signature for the case: $r_f = 2 \mu\text{m}$, $\sigma = 0.4 \text{ mN/m}$ and $D = 20 \mu\text{m}$, (b)-(i) cell volume fraction showing cell position and deformation at different times during passage through the filter.	92
4.3	(a) Inlet pressure signature for the case: $r_f = 4 \mu\text{m}$, $\sigma = 1.1 \text{ mN/m}$ and $D = 16 \mu\text{m}$, (b)-(i) cell volume fraction showing cell position and deformation at different times during passage through the filter. (cont.)	93
4.3	(a) Inlet pressure signature for the case: $r_f = 4 \mu\text{m}$, $\sigma = 1.1 \text{ mN/m}$ and $D = 16 \mu\text{m}$, (b)-(i) cell volume fraction showing cell position and deformation at different times during passage through the filter.	94
4.4	(a) Inlet pressure signature for the case: $r_f = 2 \mu\text{m}$, $\sigma = 2 \text{ mN/m}$ and $D = 12 \mu\text{m}$, (b)-(i) cell volume fraction showing cell position and deformation at different times during passage through the filter. (cont.)	95
4.4	(a) Inlet pressure signature for the case: $r_f = 2 \mu\text{m}$, $\sigma = 2 \text{ mN/m}$ and $D = 12 \mu\text{m}$, (b)-(i) cell volume fraction showing cell position and deformation at different times during passage through the filter.	96
4.13	Threshold pressure dependence on filter pore radius and cell cortical tension for (a) $D = 12 \mu\text{m}$, (b) $D = 16 \mu\text{m}$ and (c) $D = 20 \mu\text{m}$	107
4.14	Threshold pressure dependence on cell cortical tension for different pore radius and cell size.	109
4.15	Filter characteristic chart for (a) $D = 12 \mu\text{m}$, (b) $D = 16 \mu\text{m}$, (c) $D = 20 \mu\text{m}$	110

List of Tables

1.1	Comparison of concentration of CTCs with different cells normally found in human blood [14].	5
2.1	Cortical tension of blood cells and relevant cancer cells.	16
2.2	Size of blood cells and relevant cancer cells.	17
2.3	Geometric parameters of single filter.	20
2.4	Computational parameters.	22
2.5	Summary of boundary conditions.	27
2.6	Number of cells for the grids used for grid convergence test.	40

Greek letters

α	Cell volume fraction
ϵ	Axial deformation index
θ_w	Wall contact angle
θ	Pore half angle
λ	Viscosity ratio between the two phases in two phase flow
μ	Fluid viscosity
μ_c	CTC viscosity
μ_p	Plasma viscosity
ρ	Fluid density
ρ_c	CTC density
ρ_p	Plasma density
σ	Cell cortical tension

Roman letters

A	Area vector
Ca	Capillary number
D	Deformation rate tensor
D	Cell diameter
e	Lubrication film thickness
F	Source term in the momentum conservation equation
g	Gravitational acceleration vector
I	Unit tensor
\vec{n}	Volume fraction gradient
Q	Flow rate
r	Radial coordinate
R	Radius of cylindrical channel
t	Time
T	Viscous stress tensor
v	Velocity vector
x	Axial coordinate

Subscripts

A_f	Face area of computational cell
F_{CSS}	Force due to cortical tension
J_f	Mass flux through a face of computational cell
l_d	Length of deformed cell
l_{en}	Entrance chamber length
l_{ex}	Exit chamber length
l_f	Filter pore length
P	Static pressure
P_0	Total pressure
P_{in}	Inlet total pressure
$P_{viscous}$	Pressure difference due to viscous effects
$P_{cortical-tension}$	Pressure difference due to cell cortical tension
$P_{threshold}$	Threshold pressure
r_{en}	Entrance chamber radius
r_{ex}	Exit chamber radius
r_f	Filter pore radius
r_g	Grid refinement ratio
v_n	Normal velocity
v_r	Radial component of the velocity vector
v_x	Axial component of the velocity vector
\mathbf{v}_{wall}	Velocity at wall
V	Volume of computational cell
S_m	Source term in the continuity equation

Acronyms

2D	Two dimensional
3D	Three dimensional
AFM	Atomic force microscopy
CTC	Circulating tumor cell
CT	Computed tomography
DACS	Dielectrophoresis activated cell sorter
DLD	Deterministic Lateral displacement
FDA	Food and drug administration of the USA
MCA	Microcavity array
MLC	Mouse lymphoma cell
PBMC	Peripheral blood mononuclear cell

Chapter 1

Introduction

1.1 Background

Cancer is a large group of diseases that involves uncontrollable cell growth. It is one of the leading causes of death around the world, with nearly 10 million deaths in 2020 [1]. There are many different types of cancer, with breast, lung, colon and rectum amongst the most common ones [2]. Cancer can originate in many different sites of the body. However, the primary tumor site is rarely the cause of death. Cancer spreads from the initial primary site to different parts of the body by emitting tumor cells, called circulating tumor cells (CTCs) [3, 4]. These tumor cells can travel by the circulatory or the lymphatic system. Traveling to a new site, they extravasate and form secondary tumor sites. This process is called metastasis [5, 6].

Cancer cannot be accurately diagnosed with a single test. Diagnostic testing is complemented by history and physical examination. Sometimes, other conditions like an infection may present similar symptoms of cancer. The diagnostic methods involve lab tests, imaging, endoscopic examination, genetic tests, and tumor biopsies. Blood tests, urinalysis, and the detection of biomarkers indicating cancer are the types of lab tests that are performed. Biomarkers are substances produced by cancer or other cells in response to cancer.

Medical imaging can detect tumors or any other abnormality in the body noninvasively. The types of imaging used for cancer detection are X-rays, CT scan, bone scan, mammogram, which is used for breast tumor detection, ultrasound imaging, and magnetic resonance imaging (MRI). In nuclear medicine, radioactive nuclear particles are introduced in the body, which can accumulate in the cancerous site. The presence of cancerous tissue is detected through their emission. The bone scan is a type of nuclear scan that looks for abnormal areas in bone through the emission of accumulated nuclear materials. Positron Emission Tomography (PET) scan is another imaging technique where radioactive glucose injected into a vein is taken up by cancer cells. Detailed 3-D images of high uptake areas inside the body can be produced from emission.

Examples of endoscopic examinations include colonoscopy for detecting colorectal cancer and bronchoscopy for the examination of the trachea, bronchi, and lungs. In genetic testing, cancer susceptible genes are tested for mutations. On the other hand, biopsy involves the removal of tissue from the body that is further examined under a microscope to determine the presence of malignancy. The removal is performed by surgery or through a needle. After the diagnosis, generally, more tests are performed for the planning of treatments. It is essential to know the extent of cancer (stage) and the grade of abnormality of cancer cells in the body for effective treatment planning.

Many different treatment options are available for cancer like chemotherapy [7], radiotherapy [8], immunotherapy [9] and surgery. Chemotherapy involves the use of cytotoxic antineoplastic drugs. These drug agents kill cells that show rapid cell division. Many different types of drugs or their combinations are used. Targeted therapy is used for many common types of cancer where such a drug is used that targets specific molecular differences between cancer and normal cells. Radiation therapies use ionizing radiation to damage cancer cells. X-ray beams are normally used. In contrast, In nuclear medicine, radioisotopes are used, which are specifically absorbed in tumors and damage cancer cells by radiation emission. Focused ultrasound has also been proposed to destroy tumors within the body noninvasively. On the other hand, cancer immunotherapy works by artificially stimulating the body's

own immune system to recognize cancer cells having tumor antigens. Success rates of the treatments vary depending on the cancer type and cancer stage. Early detection and treatment can enhance survival rate for some types of cancer [10–12].

CTCs can share the characteristics of the primary tumor [4] and have important prognostic relevance [13, 14]. CTCs are heterogeneous in their morphology and physical properties. Their properties vary depending on cancer types [15]. They are typically larger than erythrocytes but have a size overlap with leukocytes [14]. Physical properties of CTCs will be reviewed in Section 2.1.1. They are typically stiffer than blood cells. However, metastatic cancer cells have been found to be softer [16, 17]. CTCs have been detected to form multi-cell clusters with variations in shape [18]. They were found to have both high and low nuclear to cytoplasmic ratios [19]. They have the potential to detect colorectal [20] and lung [21] cancer at early stages. CTCs have been shown to predict survival in breast cancer patients with the detection of CTC after chemotherapy, signifying increased risk of relapse [22]. Survival in colorectal cancer [23] and metastatic neuroendocrine tumor [24] have been linked with CTC count. CTCs have been detected in breast cancer patients a long time after surgery, indicating a dormant state of the cancer [25]. For many types of cancer like bladder, liver, and esophageal cancer, CTC count has been correlated with metastatic relapse [13]. For breast, prostate, and colorectal cancer, CTC enumeration has been shown to predict response to therapy [26, 27]. All these point to the fact that detection and subsequent analysis of CTCs play a very important role in cancer detection, determining disease progression, and treatment management.

Many of the cells used in cancer research are cultured cells that retain most of the properties of their origin [28]. They work as a model system in the study of the properties of the cells and drug discovery. Over the years, many different cell culture lines have been established. The relevant cell lines for this study are MCF-7, MDA-MB-231, MDA-MB-468, MCF-10 A, RT4, and HL60. MCF-7, MDA-MB-231, and MDA-MB-468 are all breast cancer cell lines. The acronym MCF stands for Michigan Cancer Foundation. MCF-10A is a nontumorigenic breast cell line. The HL-60 is a human leukemia cell line, while RT4 is a bladder cancer cell line. Cultured

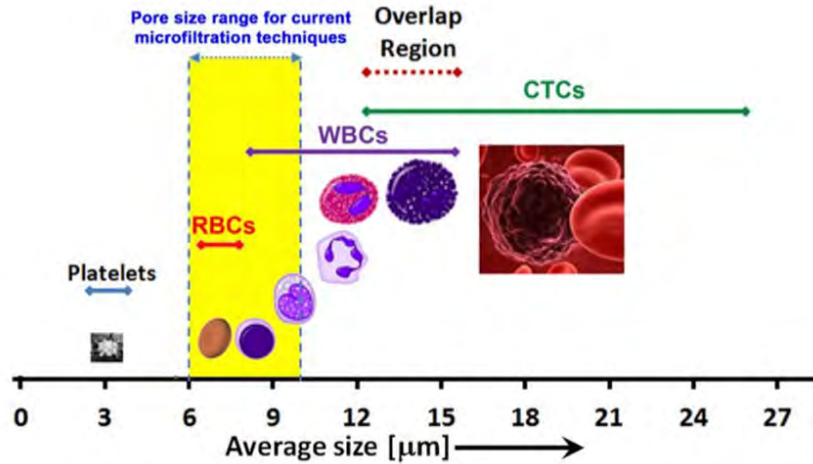


Figure 1.1: Size distribution of blood cells and comparison with CTCs [14].

cells are homogeneous with stable properties [29]. However, tumor cells derived from patients show significant variation in properties depending on the cancer type, and patient [15, 30]. Meng et al. [25] found CTCs from metastatic breast cancer patients to have a similar size and nuclear to cytoplasmic ratio. However, separate studies have found CTCs from breast cancer patients to have a larger size compared to cultured cells [31].

1.2 CTC detection: literature review

CTC detection from blood samples is challenging because of their extremely low concentration [18]. Table 1.1 shows the comparison of the concentration of CTCs with normal blood cells. Different approaches have been employed for isolating tumor cells from blood samples. The techniques can be broadly divided into two: biochemical and biophysical approach [29]. Biochemical approaches use the binding of target cells and biochemical labels. Current technologies use epithelial cell adhesion molecule (EpCAM) antibodies to separate CTCs. FDA-approved commercial system CellSearch uses this technique where anti-EpCAM antibody-conjugated magnetic beads are used for CTC capture [32]. However, biochemical methods can

Table 1.1: Comparison of concentration of CTCs with different cells normally found in human blood [14].

Cell type	Concentration of cells/ml
Red blood cells	$4.2- 6.2 \times 10^9$
Platelets	$1.5- 4 \times 10^8$
Neutrophils	$3- 5.8 \times 10^6$
Eosinophils	$5- 25 \times 10^4$
Basophils	$1.5- 5 \times 10^4$
Lymphocytes	$1- 3 \times 10^6$
Monocytes	$3- 5 \times 10^5$
CTCs	1-10

be unreliable due to several reasons [33]. Some metastatic cancer cells undergo epithelial to mesenchymal transition (EMT), which results in the loss of the epithelial marker expression.

In contrast, physical CTC separation techniques exploit the difference in physical properties like size, shape, density, deformability, and electrical polarizability [34]. Density gradient centrifugation has been employed to separate CTCs from blood cells [35, 36]. However, heterogeneity in normal blood cells and CTCs mean other large benign cells may be identified as cancer cells [37]. Cell dielectric properties depend on cell morphology, and membrane surface area [38]. When subjected to an electric field, cells move towards or away from a strong field region [29]. Thus cells having different dielectric properties can be separated in this process. Alazzam et al. [39] separated breast cancer cell MDA-MB-231 after mixing with normal blood cells using dielectrophoresis. Acoustophoresis is another technique that uses acoustic forces to separate cells based on their density and deformability [40, 41]. Li et al. [42] used an acoustic-based microfluidic device to separate cancer cells from cell culture lines with a very high recovery rate. They also used their device to separate cancer cells from blood samples collected from breast cancer patients.

Hydrodynamic separation techniques use the difference in hydrodynamic forces on a particle to separate it from other particles [43]. Hydrodynamic forces depend on particle size. One of the most used designs is the Deterministic Lateral Displacement (DLD) device, where particles/cells face obstructions in flow. The principle is shown in Figure 1.2. Small cells follow the streamline of the flow, whereas large cells may

shift to a different streamline while encountering the obstruction and get separated from other cells [44].

When a cell flows through a curved microchannel, it is subjected to drag force along with wall effect lift and shear gradient lift force [29]. Balance of these forces causes different-sized cells to occupy different equilibrium trajectories. Hou et al. [45] isolated CTCs from lung cancer patients using spiral microchannel. Sollier et al. [46] used a vortex-based chip that separated larger cells that deviated from the initial streamline to a trap containing vortices. The design and principle of the device are shown in Figure 1.3.

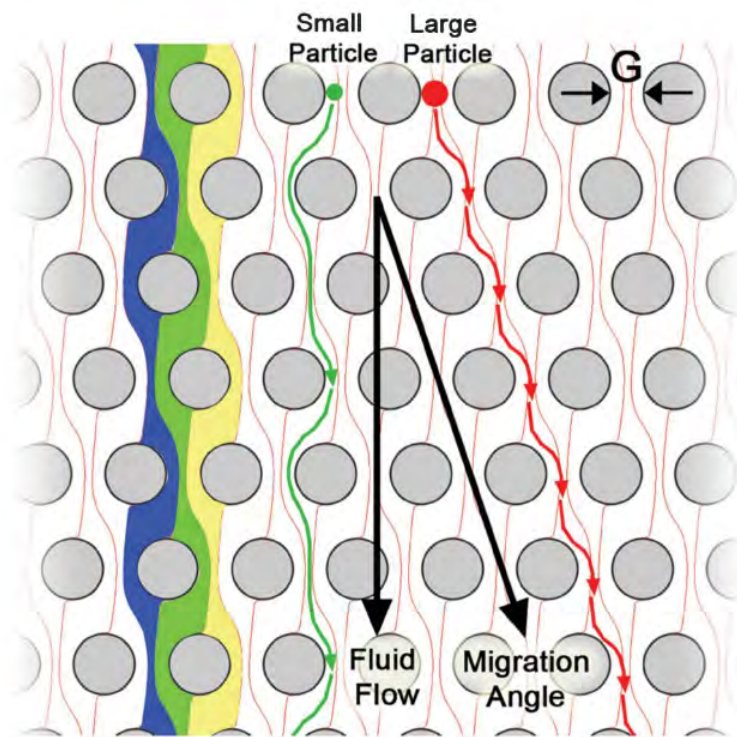


Figure 1.2: Principle of deterministic lateral displacement where small particles can follow the streamline around obstacles but large particles get shifted to different streamlines and are separated [29].

Microfiltration devices isolate tumor cells by using the flow of blood samples through microstructures like micropores [47], micropillars [48] or microfilters on a microfluidic chip. Filtration of cells depend both on their size[46] and deformability [49]. Figure 1.4 shows a membrane filter device containing micropores to trap LNCaP cells. Mohamed et al. [50, 51] developed a filter device consisting of columns with

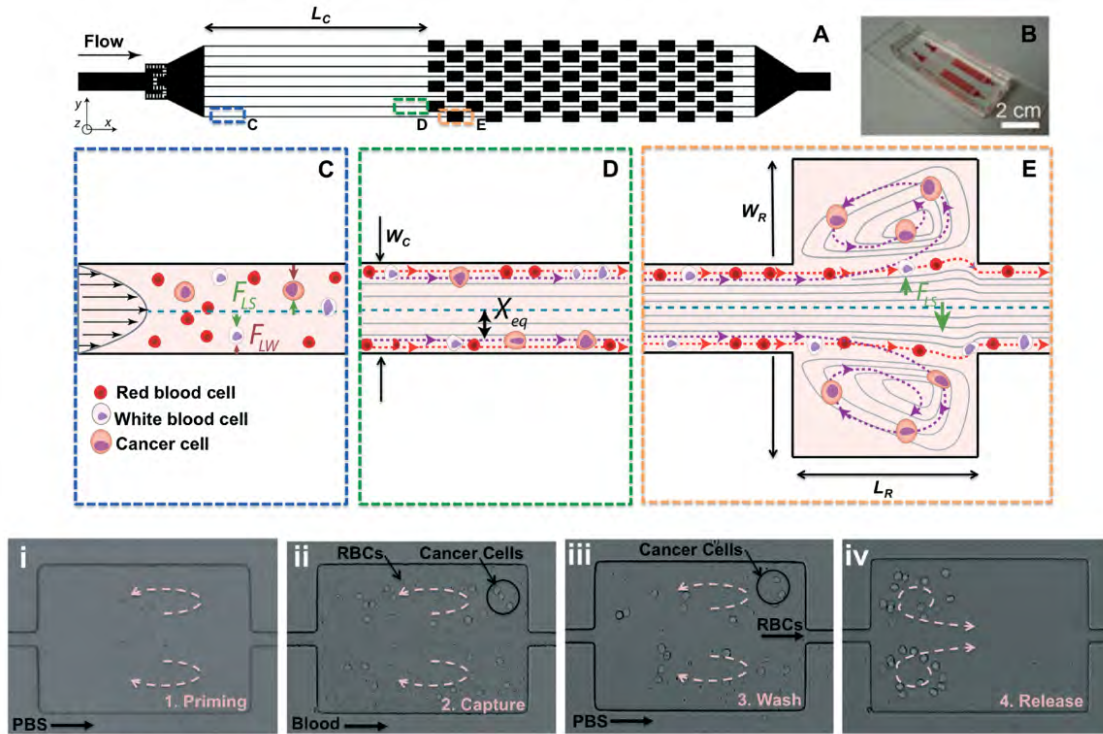


Figure 1.3: Design and principle of vortex based chip from [46]. Larger cells are trapped in the chamber. The bottom row shows separation of cancer cells.

varying gaps in the range of 20 to 5 μm (Figure 1.5). They filtered human blood mixed with neuroblastoma cells based on cell size.

Deformability-based separation techniques make use of the fact that CTCs are usually stiffer than normal blood cells [25, 52]. The force required to deform a cell in order to pass through the microstructures depends on its deformability. These devices can not only sort cells according to their stiffness, but they can also be used to measure the deformability of cell samples. Beech et al. [53] used a DLD device to sort cells by deformability in addition to shape and size. They incorporated deformability by considering shear stress on a cell by the carrier fluid, which makes them elongated. Ahmmed et al. [54] used flow-induced deformability to separate strongly metastatic breast and prostate cancer cells from weakly metastatic ones. They found that strongly metastatic breast cancer cells are more deformable than weakly metastatic breast cancer cells. However, they found the opposite to be true for prostate cancer cells. Pang et al. [55] used a microfluidic device that used staggered microstructures to separate MCF-7, MDA-MB-231, and MDA231-LM2

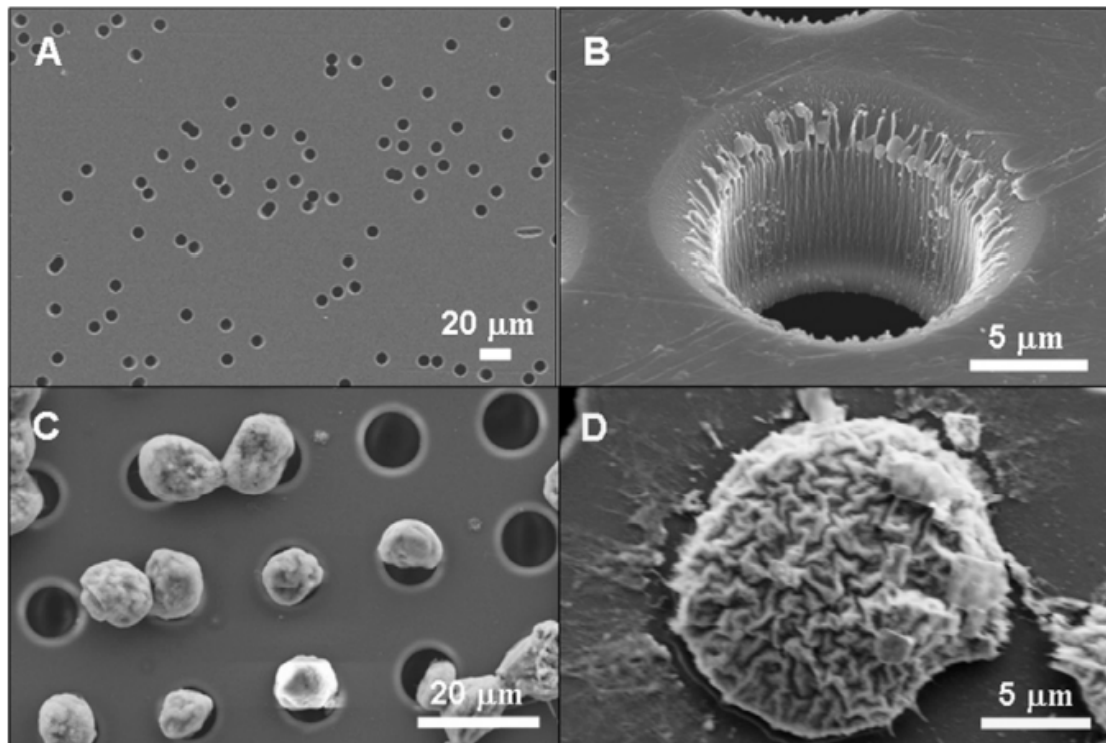


Figure 1.4: Membrane filters showing micropores with the bottom row showing captured human prostate adenocarcinoma LNCaP cells [47].

cancer cells based on their size and deformability. Their device can also isolate cancer cells from blood samples.

Cancer cells have been characterized by Byun et al. [56] by their deformability and surface friction according to the cells' transit time through microconstrictions. They found that cells with higher metastatic potential show faster velocities. They also found that reduced surface friction may be important for invasive cancer cells to squeeze through confined spaces. Hou et al. [57] used a simple microfluidic channel device to differentiate malignant cells from non-malignant cells using their entry time and transit velocity through the microchannel.

Guo et al. [58] constructed a microfluidic ratchet device consisting of a chain of microscale funnel constrictions. Individual rectangular funnels were tapered, which led to pressure asymmetry for driving cells along and against the direction of the taper. They also discovered rectified motion under unbiased oscillatory flow for cells passing through the chain of funnel constrictions. Using similar devices, they also measured deformability of normal blood and cancer cells [59, 60].

A practical filtration device consisting of multiple rows of filter funnels with progressively decreasing pore size in a single row was constructed by McFaul et al. [61] Under forward flow, the cells get trapped in funnels based on their size and stiffness. One of the drawbacks of microfilter devices is clogging by cells. They used reverse flow to unclog the cells from funnels, and a simultaneous cross-flow is used to drive the cells towards a reservoir from where the cells can be collected for further analysis. L1210 mouse lymphoma cells (MLCs) and human peripheral blood mononuclear cells (PBMCs) were used to represent two types of cells with different mechanical properties. They showed their device to achieve very high separation efficiency. Lin et al. [62] used a similar device to separate UM-UC13 bladder cancer cells from the blood. They added a hydrodynamic concentrator to get rid of the fluid in the blood and a portion of leukocytes using their size. The schematic of their ratchet cell sorting device and the capture and separation of UC13 cells from leukocytes are shown in Figure 1.7. Cell viability after sorting through filters is important for subsequent analysis or culture of cells. Contact with the filter wall and hydrodynamic forces can render cells damaged, or even dead [63, 64].

Experimental techniques to separate CTC from blood samples focus on device design, fabrication, and operation. Numerical methods offer an alternative way to simulate the filtration process in filter devices. Insight into the underlying physics of filtration can help to establish filter characteristics and operating conditions for isolating cells of particular physical property. Numerical methods also offer a pathway to device optimization without costly experimental setups. For deformability-based filters, it can lead to the understanding of the fundamentals of cell deformation and filtration through filter funnels and the effect of physical properties like cell stiffness and filter funnel geometric parameters.

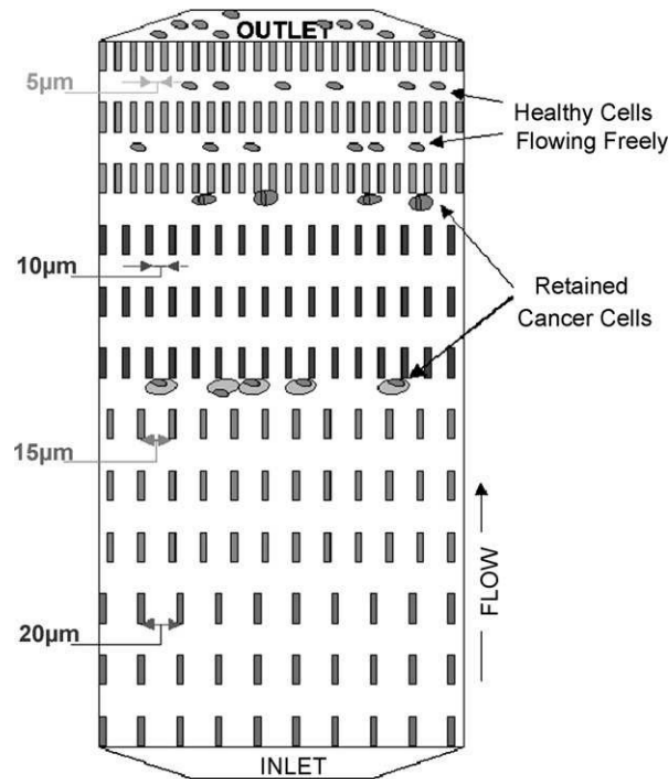
Various numerical studies have been conducted for optimizing cell filtering devices [65]. Kabacaoglu et al. [66] used numerical simulation to optimize a DLD cell filtering device. Li et al. [67] performed a numerical optimization of a microfluidic CTC filtering chip. They considered cell damage by membrane area strain and investigated pore shape for damage limitation. Aghaamoo et al. [68] proposed deterministic dielectrophoresis that combines DLD and traditional insulator-based

dielectrophoresis. Using numerical simulation, they investigated different operational and geometrical parameters of their design.

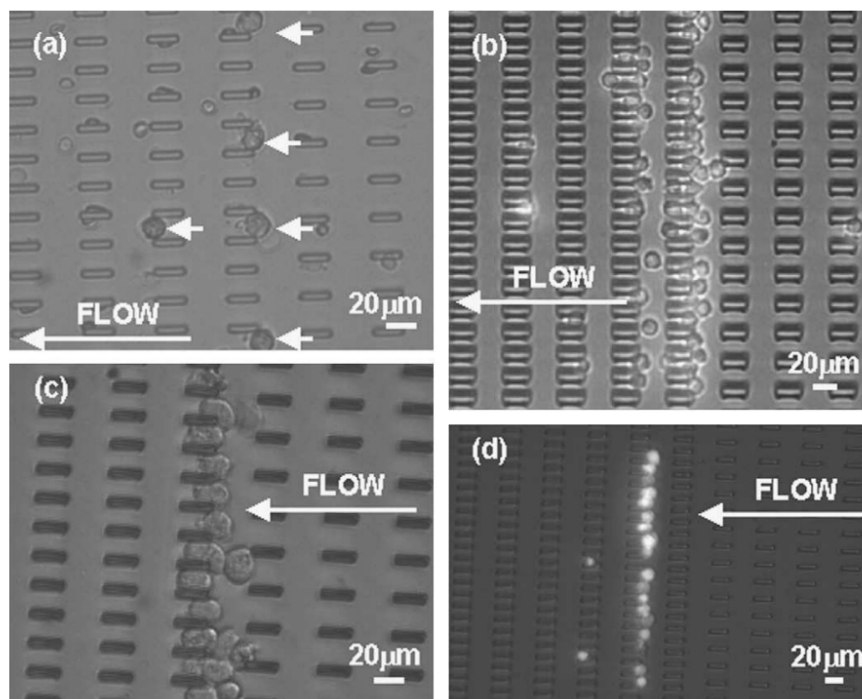
Computational methods have been used to understand cell deformation and separation in microfluidic devices. Wu et al. [69] determined threshold pressure for the passage of an RBC through a contracting microfluidic channel similar to [58]. They modeled the RBC membrane as a triangular particle- spring meshwork with bending elasticity between neighboring triangles. Aljaghtham et al. [70] used combined solid and fluid mechanical simulation to probe the possibility of using cell stiffness difference for isolating rare cells.

CTC squeezing process through a narrow channel of different geometry was studied by Zhang et al. [71]. They considered the cell as a Newtonian droplet with cortical tension and obtained pressure signature and threshold pressure for CTC passing. In a separate study, passing pressure dependence on the thin film between CTC and the filter wall was studied [72]. Aghaamoo et al. [73] conducted a numerical study of a cell passing through single and short conical funnel arrays having the same pore size. They also kept the physical property of the tumor cell constant. Effect of pore half angle on pressure asymmetry and effect of oscillating pressure frequency and duty cycle on system performance was reported.

Different experimental studies have demonstrated the capabilities of microfluidic filter array devices in separating cancer cells. These experiments mostly use two or more types of cells as surrogates of cell types having distinct physical properties. On the other hand, computational studies so far have mostly focused on cell deformation and pressure characteristics in single filter funnels. But the effect of CTC physical properties in determining cell trapping in specific funnels of a filter array device is still unknown. The in-depth study of the cell trapping characteristics in a filter array device under different operating conditions is also elusive. The present study investigates cell trapping in a microfluidic filter array device based on physical properties. Trapping in specific funnels can lead to the sorting of the captured cells. Moreover, a method is established from single filter pressure characteristics to predict trapping and sorting under different operating conditions.

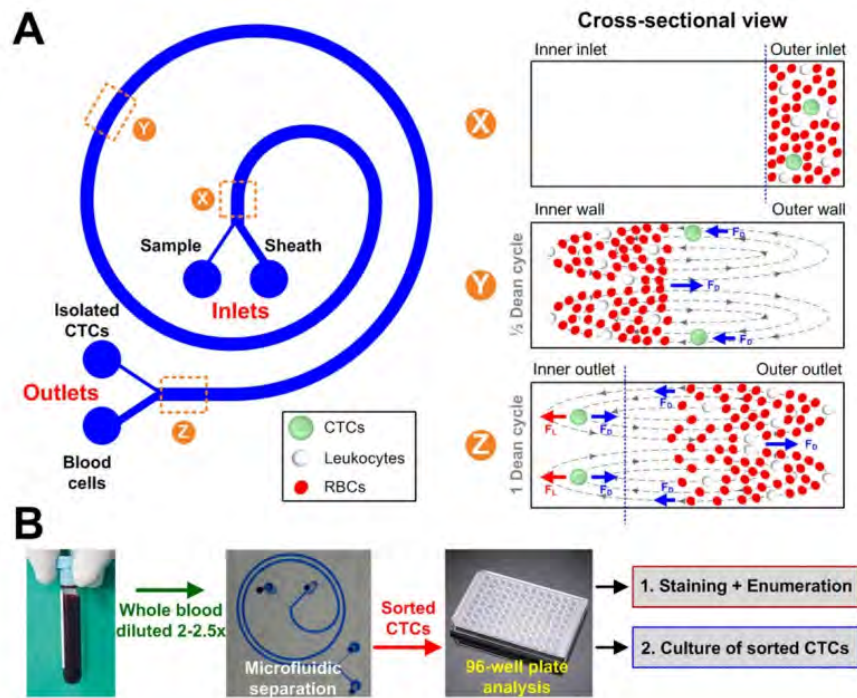


(a)

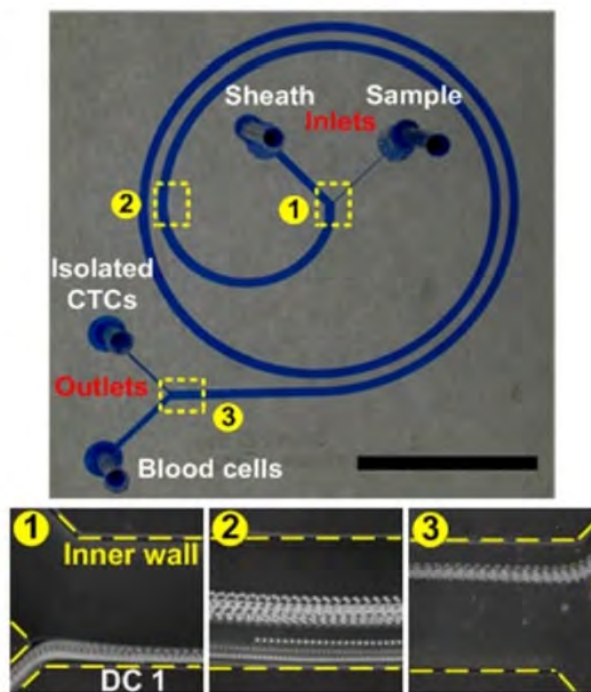


(b)

Figure 1.5: (a) Schematic of the microfluidic filter device used by [51] showing varying channel gaps, (b) Capturing of MDA-MB-231, SW620 and HEK293 cells which have different physical properties.

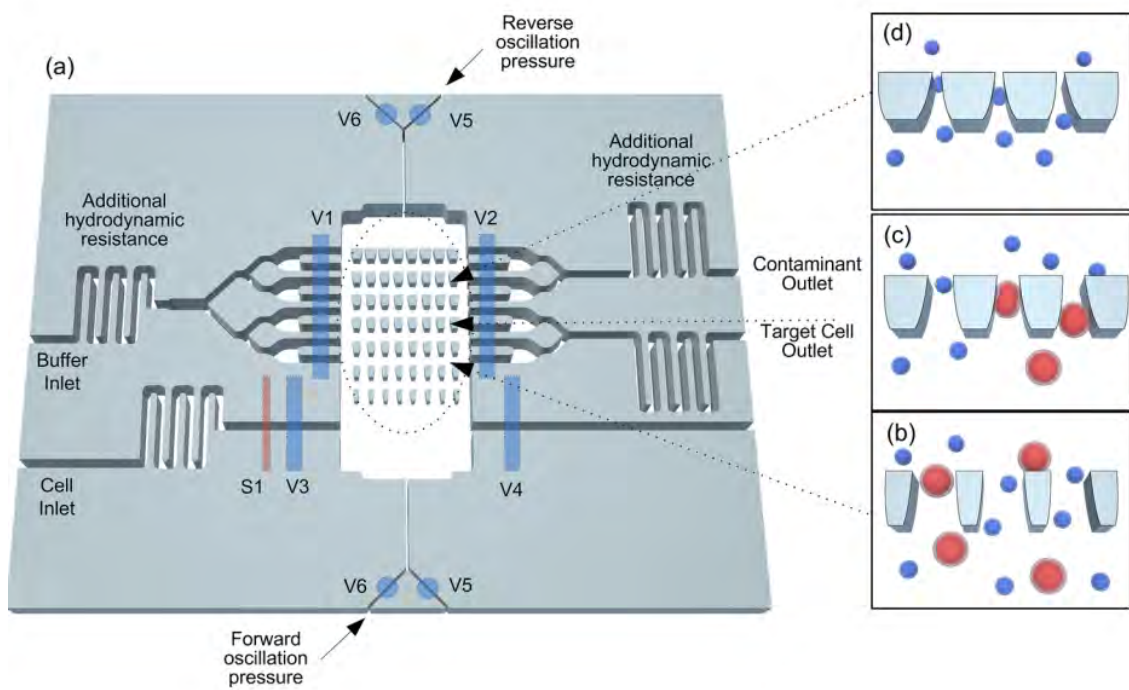


(a)

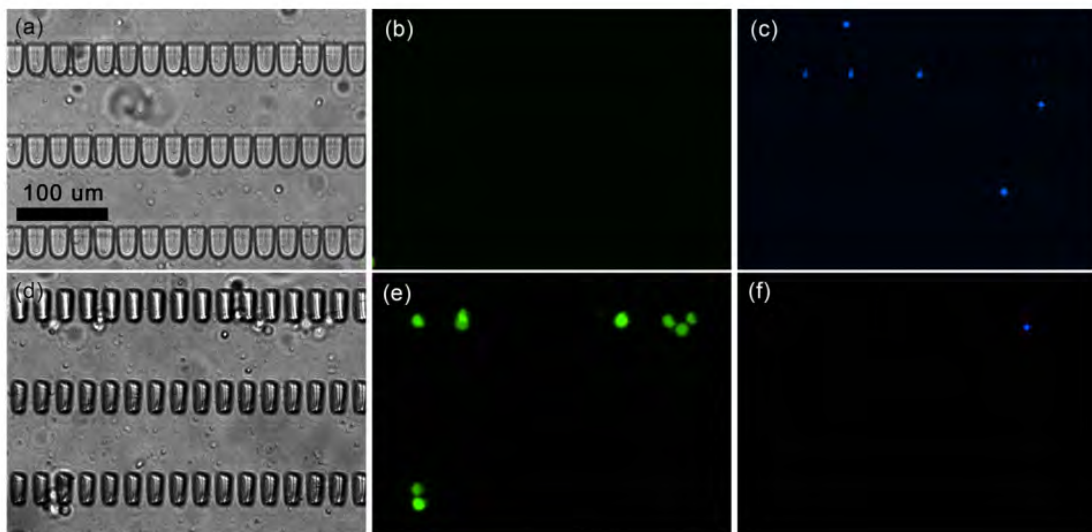


(b)

Figure 1.6: (a) Schematic and design principle of the device used by [45] that separates CTCs using Dean Flow Fractionation (DFF), (b) MCF-7 cells in their focusing position in the microchannel.



(a)



(b)

Figure 1.7: (a) Schematic of the ratchet cell sorting device used by [62], (b) separation of larger and stiff UC13 cancer cells from smaller and deformable leukocytes. Leukocytes travelled to the top while UC13 cells are trapped at the bottom.

1.3 Objectives

The objectives of this study are:

1. To develop a computer model to identify the deformation and threshold pressure characteristics of CTCs while passing through a microfluidic filter device and validate the model.
2. To investigate the microfluidic filter funnel array with varying pore size to achieve physical property-based cell trapping and sorting under pressure-driven flow.
3. Establishing filter operating characteristics from threshold passing pressure of CTCs with a range of cell physical properties (cortical tension and diameter).

1.4 Organization of the thesis

This thesis consists of five chapters. Chapter 1 presents the clinical significance of circulating tumor cells (CTCs) in cancer and a review of the existing CTC detection methods and complementary numerical studies. In chapter 2, relevant CTC physical properties are listed along with the physical model of the CTC and an outline of the numerical method used in this study. Chapter 3 presents the results of numerical simulations demonstrating both CTC isolation and sorting under pressure-driven flow. Filter operating characteristic is established in chapter 4 from the results of threshold CTC passing pressure for a range of cell physical properties. Finally, the outcomes of this work are summarized in chapter 5, along with suggestions for future work based on the findings of this study.

Chapter 2

Physical Model and Numerical Method

2.1 Problem description

2.1.1 Physical properties of tumor cells

Many different experimental techniques have been employed to measure the mechanical properties of biological cells. Currently used techniques include atomic force microscopy (AFM), magnetic twisting cytometry, micropipette aspiration, optical tweezers, shear flow, substrate stretching, etc. [74, 75] Amongst typical blood cells, Evans et al. [76] measured cortical tension of blood granulocytes by micropipette aspiration. Red blood cell cortical tension was measured by Guo et al. [60] with a microfluidic funnel device. Cross et al. [16] reported stiffness by AFM of the lung, breast, and pancreatic carcinoma cells. Stiffness of non-tumorigenic epithelial breast cell line MCF-10A, breast cancer cell lines MCF-7 and MDA-MB-231 were reported in many different studies using AFM [77, 78]. Li et al. [79] studied effect of loading rate in AFM on breast cancer cells MCF-7 and MCF-10A. They found that the apparent Young's modulus increases with the loading rate. Hosseini et al. [80] used AFM cell confinement to measure mechanical properties of the actin

Table 2.1: Cortical tension of blood cells and relevant cancer cells.

Cell	Cortical Tension (mN/m)
Red blood cell	0.011-0.012 [60]
Neutrophil	0.035 [76]
Lymphocyte	0.075 [59]
HL-60	0.155 [81]
RT4 bladder cancer cell	0.185 [59]
MCF-7	0.28 [80]
MCF-10A	0.4 [80]
MDA-MB-231	1.1 [83]
MDA-MB-468	2 [83]

cortex of cancer cells MCF-7 and MCF-10A during interphase and mitosis. They reported cell cortical tension of the cancer cells based on their studies. Using AFM, Rosenbluth et al. [81] measured cell stiffness of human leukemia cell line HL60, Jurkat, and neutrophils. They also evaluated equivalent cortical tension of the cells using a liquid drop model of the cell. Lekka et al. [82] reported Young's modulus of cancerous human bladder cells using scanning force microscopy. Guo et al. [59] also reported cortical tension of RT4 bladder cancer cells using a microfluidic funnel device similar to [60]. Using micropipette aspiration, Mohammadalipour [83] experimentally determined cortical tension of breast cancer cell lines MDA-MB-231 and MDA-MB-468. The current study considers cortical tension in the range of 0.2 to 2 mN/m. Relevant tumor cell cortical tensions are reported in Table 2.1. It is evident that tumor cells are stiffer than normal blood cells.

There is a considerable variation in tumor cell size. Even cells from the same family can vary over a large range. Relevant tumor cell diameters are enlisted in Table 2.2. Although tumor cells are larger than red blood cells and many white blood cells, there is some overlap between larger white blood cells and tumor cells [84]. For this reason, tumor cell isolation methods based on only cell size may not purely capture CTCs. The cancer cell diameter values show variation over a range of 10- 24 μm . There are differences in reported values for the same type of cell. The current study considers cell diameter in the range of 12 to 20 μm .

Cancer cells have been filtered by centrifuging, which takes advantage of the fact that some cancer cells are less dense (specific gravity 1.056) than normal blood cells [35]. Healthy erythrocytes have a density in the range of 1.1- 1.12 g/mL [88]. HL-60

Table 2.2: Size of blood cells and relevant cancer cells.

Cell	Diameter (μm)
Red blood cell	5.6 ± 0.2 [85]
Neutrophil	12- 14
Monocyte	upto 20
HL-60	16.84 ± 6.40 [15]
	18.5 ± 2.3 [55]
MCF-7	18.16 ± 7.42 [15]
	16.25- 24.38 [86]
	22.5 [87]
MCF-10A	15.63- 22.50 [86]
	17.74- 18.18 [83]
MDA-MB-231	17.9 ± 2.5 [55]
	12.40 ± 1.16 [15]
	12.4 ± 1.16 [85]
MDA-MB-468	16.76- 19.04 [83]

leukemia cells were measured to have a density in the range 1.05- 1.09 g/mL [89]. The blood plasma density is dependent upon temperature. At 37°C plasma was found to have density of 1.02 g/mL [90]. For the present study, tumor cell density was set at 1.06 g/mL, and plasma density was set at 1.02 g/mL.

Biological cells are highly viscous. Plasma viscosity is 0.0012- 0.0013 Pas at 37°C [91]. Whereas neutrophil cytoplasm has a viscosity of 183 Pas, and its nucleus has a viscosity of 232.3 Pas [92]. Cancer cells can be more viscous than normal blood cells. Coumans et al. [93] measured the apparent viscosity of MDA-MB-231 cells to be 1600 ± 200 Pas using passage time of cells passing through 5 μm pores. In contrast, they found red blood cell and white blood cell apparent viscosity to be 0.035 ± 0.010 and 3.2 ± 2.5 Pas respectively.

2.1.2 Modeling of cell behavior

Cell behavior under external forces can be modeled in many different ways considering many different levels of complexity [94]. These models can be broadly divided into two approaches: micro/nanostructural approach and continuum approach [95]. The first approach treats the cytoskeleton as the main structural component and considers cell behavior at the subcellular level. On the other hand, the continuum approach considers the cell to be made of a material having continuum properties.

Even within the continuum approach, there are many different models of cell behavior stemming from many different types of experiments. Experimental techniques like micropipette aspiration are described by cortical shell liquid core model [76, 96], or the solid model [97, 98]. On the other hand, AFM indentation is described by the solid model [99] or the power-law structural damping model [100]. Solid models are applicable for small deformations, but for large deformations, liquid drop models are more suitable [101].

CTCs in this study are modeled as Newtonian liquid droplets with constant viscosity. Cell cortical stiffness is simulated by the surface tension effect. Although this approach neglects internal cell structure, molecular deformation, or sub-cellular response, it provides a description of large deformations at the cellular level [95]. Previous experimental studies have shown the adequacy of the liquid drop model for the prediction of threshold pressure required for cell passing through microconstrictions [58]. Numerical studies have also been performed adopting the model for prediction of pressure signature for cancer cells passing through microfluidic channels [71, 73, 102].

2.1.3 CTC filter construction

Different filtration techniques based on CTC physical properties have been previously discussed in Section 1.2. Guo et al. [58] fabricated a microfluidic ratchet device for selective transport of cells based on their internal mechanics. The device consisted of a chain of funnel constrictions with pore sizes ranging from 11 μm to 3 μm . The funnel length was 30 μm with 35 μm long intermediate chambers. The half angle of the funnels were 10°, 5° and 0°. The funnel shape of the filters creates an asymmetry in the threshold pressure for forward and backward motion. Backward threshold pressures are larger for a particular filter funnel. A similar device was also used to measure the deformability of single cells [59, 60]. Based on this ratchet device, McFaul et al. [61] constructed a device that combined parallel arrays of funnel constrictions. This increased throughput enabling larger blood samples to be filtered. They used funnel pore sizes ranging from 15 μm to 1 μm . Aghaamoo

et al. [73] performed a computational study of conical filters where they studied the effect of filter pore half angles in the range of 2° to 20° . They only considered a filter pore radius of $3 \mu\text{m}$ with the filter length set at $25 \mu\text{m}$. They also studied cell motion in a conical filter array under a flow having a square wave profile.

For this study, conical filters are considered similar to Aghaamoo et al. [73] Filter geometric properties are selected based on the previous works discussed above.

2.1.4 Filter geometry

The physical model of a single conical filter is shown in Figure 2.1 with a sketch detailing the geometric parameters of the filter funnel. Taking advantage of the rotational symmetry about the axis, only a 2D section was considered as the computational domain. The total length of a single filter is $85 \mu\text{m}$.

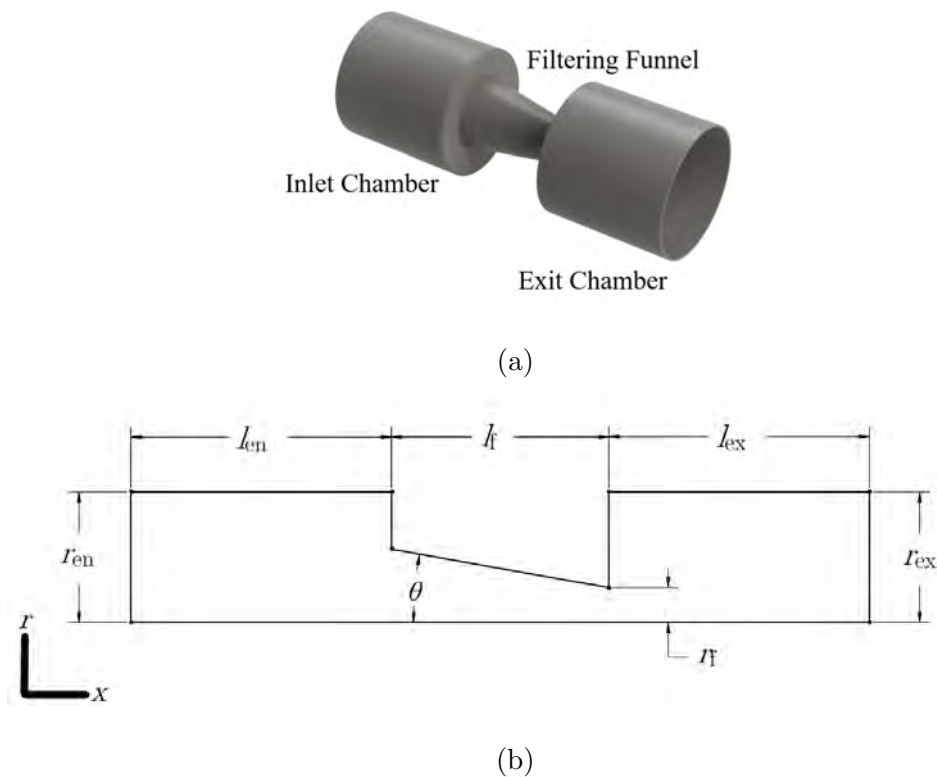


Figure 2.1: (a) 3D physical model of single filter, (b) 2D sketch showing geometric parameters.

The dimension of the geometric parameters are listed in Table 2.3. All the geometric parameters except filter pore radius, r_f were kept constant. Three different values

Table 2.3: Geometric parameters of single filter.

Geometric parameter	Dimension
Entrance chamber length, l_{en}	30 μm
Filter length, l_f	25 μm
Exit chamber length, l_{ex}	30 μm
Entrance chamber radius, r_{en}	15 μm
Exit chamber radius, r_{ex}	15 μm
Filter pore half angle, θ	10°
Filter pore radius, r_f	2, 4 and 6 μm

of r_f were taken: 2, 4 and 6 μm . The values were selected based on previous experimental [58, 61] and computational [73] studies.

The filter array was constructed by connecting three different filter funnels in series. The geometric parameters were kept the same, but the pore radius was varied from 6 μm for funnel 1, 4 μm for funnel 2 to 2 μm for funnel 3. The total length of the funnel array was 195 μm . Figure 2.2 shows the 3D model and 2D sketch of the filter array detailing the dimensions.

2.1.5 Computational parameters

Cell physical properties for the computation were selected based on the discussion in Section 2.1.1. Four different cell cortical stiffness values were selected mirroring the cell cortical tension of RT4 bladder cancer cell, MCF-10A, MDA-MB-231, and MDA-MB-468 breast cancer cells (Table 2.1). Cancer cell diameter was found to vary over a range of 10- 24 μm (Table 2.2). Three different values of cell diameter were selected, representing the range of 12- 20 μm . The densities of plasma and the CTC were set at 1.02 and 1.06 g/mL, respectively, based on values reported by experimental studies (Section 2.1.1).

The effect of cancer cell viscosity on cancer cell passing phenomena through a microchannel and passing pressure has been computationally studied by Zhang et al. [72] They observed the formation of thin plasma films between the cell and the channel wall during the cell occupation phase within the channel. The film thickness was found to increase with cell viscosity. On the other hand, the maximum pressure drop was found to initially decrease and then increase again with an increase

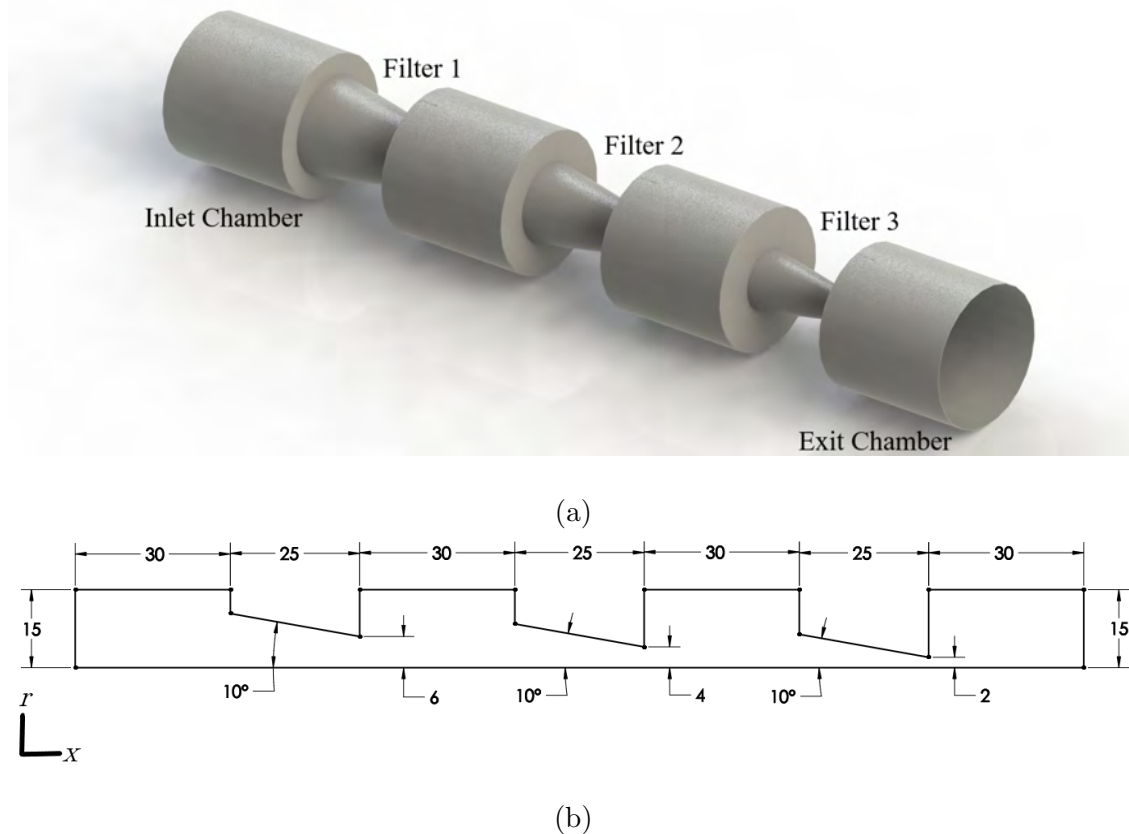


Figure 2.2: (a) 3D physical model of filter array, (b) 2D sketch showing dimensions in μm .

in cell viscosity. Cell passage through a channel was divided into five phases: entry, squeezing in, cell occupation, squeezing out, and exit. Only the occupation phase was identified to behave differently under a high viscosity ratio. The cell to plasma viscosity ratio was reported only up to the value of 64. Hence, it is unknown how maximum pressure might behave at higher viscosity ratios. In a separate study, Zhang et al. [103] studied the effect of Non-Newtonian behavior of cancer cells. They modeled CTCs as shear-thinning liquid. They obtained threshold pressure at high flow rates and found that the highest pressure occurs at different states of cell occupation in a microfluidic channel for Newtonian and non-Newtonian cell models. At low flow rates, the results from the two models are similar. Cell viscosity affects inlet pressure when there is a cell passing incident through a funnel. The trapped state is a static condition with the cell position getting fixed and the flow rate dropping to zero. In this case, only pressure difference due to cortical tension effects

Table 2.4: Computational parameters.

Parameter	Value
Cell cortical Tension, σ	0.2, 0.4, 1.1 and 2 mN/m
Cell diameter, D	12, 16 and 20 μm
Cell density, ρ_c	1.06 g/mL
Plasma density, ρ_p	1.02 g/mL
Cell viscosity, μ_c	0.0012 Pas
Plasma viscosity, μ_p	0.0012 Pas

is present. In this study, the cancer cell viscosity effect was not considered. Cell viscosity was set to be the same as blood plasma, 0.0012 Pas. All the computational parameters are listed in Table 2.4.

2.2 Governing equations

The Cell passage through the conical filter is modeled by a two-phase flow where the phases CTC and plasma are immiscible. Cell cortical tension is modeled by surface tension between the phases. Any heat transfer effect is neglected. Because of the very small Reynolds number associated ($Re = 0.025 - 0.075$), the flow is considered to be laminar. Due to symmetry, the physical domain is considered to be axisymmetric. A single set of mass and momentum equation describes the flow, with a separate transport equation for capturing cell phase volume fraction within the continuous plasma media. The conservation of mass or the continuity equation can be generally written as:

$$\frac{\partial \rho}{\partial t} + \nabla \cdot (\rho \mathbf{v}) = S_m, \quad (2.1)$$

where ρ is the density, \mathbf{v} is the velocity vector, and S_m is the source term which can represent mass added to the continuous phase from the second phase as found in problems involving vaporization of droplets. For 2D axisymmetric geometries, the continuity equation takes the following form:

$$\frac{\partial \rho}{\partial t} + \frac{\partial}{\partial x} (\rho v_x) + \frac{\partial}{\partial r} (\rho v_r) + \frac{\rho v_r}{r} = S_m, \quad (2.2)$$

where v_x and v_r are the axial and radial components of velocity. The source term S_m is taken to be zero in this study as no mass transfer is considered between the cell and the plasma phase. The general form of the conservation of momentum is written as:

$$\frac{\partial}{\partial t}(\rho \mathbf{v}) + \nabla \cdot (\rho \mathbf{v} \mathbf{v} + p \mathbf{I} - \mathbf{T}) = \rho \mathbf{g} + \mathbf{F}, \quad (2.3)$$

where p is the pressure, \mathbf{I} is the unit tensor, \mathbf{g} is the gravitational acceleration vector, \mathbf{F} is the source term and \mathbf{T} is the viscous stress tensor. The viscous stress tensor is given by

$$\mathbf{T} = 2\mu \left(\mathbf{D} - \frac{1}{3} (\nabla \cdot \mathbf{v}) \mathbf{I} \right), \quad (2.4)$$

where μ is shear viscosity and

$$\mathbf{D} = \frac{1}{2} \left(\nabla \mathbf{v} + (\nabla \mathbf{v})^T \right) \quad (2.5)$$

is the deformation rate tensor. Non-Newtonian effects for the cell can be added to the model by expressing cell viscosity, μ_c as a function of \mathbf{D} ,

$$\mu_c = \mu_c(\mathbf{D}). \quad (2.6)$$

μ_c can be determined by relating it to the second invariant of \mathbf{D} by defining,

$$\dot{\gamma} = \sqrt{2\mathbf{D} : \mathbf{D}} \quad (2.7)$$

and expressing μ_c as,

$$\mu_c = \mu_c(\dot{\gamma}). \quad (2.8)$$

One such model is the power law expression which can be written as,

$$\mu_c = k \dot{\gamma}^{n-1} \quad (2.9)$$

where k is the consistency index and n is the power law index expressing deviations from Newtonian behavior. $n = 1$ indicates Newtonian fluid, $n > 1$ indicates shear thickening fluid, and $n < 1$ gives shear thinning properties to the fluid. No gravity

effect was considered in this study. The source term \mathbf{F} is used to include surface tension effects. For 2D axisymmetric geometries, the axial and radial components of the momentum conservation equation can be written as,

$$\begin{aligned} \frac{\partial}{\partial t} (\rho v_x) + \frac{1}{r} \frac{\partial}{\partial x} (r \rho v_x v_x) + \frac{1}{r} \frac{\partial}{\partial r} (r \rho v_r v_x) = & - \frac{\partial p}{\partial x} + \frac{1}{r} \frac{\partial}{\partial x} \left[r \mu \left(2 \frac{\partial v_x}{\partial x} - \frac{2}{3} (\nabla \cdot \mathbf{v}) \right) \right] \\ & + \frac{1}{r} \frac{\partial}{\partial r} \left[r \mu \left(\frac{\partial v_x}{\partial r} + \frac{\partial v_r}{\partial x} \right) \right] + F_x \end{aligned} \quad (2.10)$$

and

$$\begin{aligned} \frac{\partial}{\partial t} (\rho v_r) + \frac{1}{r} \frac{\partial}{\partial x} (r \rho v_x v_r) + \frac{1}{r} \frac{\partial}{\partial r} (r \rho v_r v_r) = & - \frac{\partial p}{\partial r} + \frac{1}{r} \frac{\partial}{\partial x} \left[r \mu \left(\frac{\partial v_r}{\partial x} + \frac{\partial v_x}{\partial r} \right) \right] \\ & + \frac{1}{r} \frac{\partial}{\partial r} \left[r \mu \left(2 \frac{\partial v_r}{\partial r} - \frac{2}{3} (\nabla \cdot \mathbf{v}) \right) \right] \\ & - 2 \mu \frac{v_r}{r^2} + \frac{2}{3} \frac{\mu}{r} (\nabla \cdot \mathbf{v}) + F_r, \end{aligned} \quad (2.11)$$

where

$$\nabla \cdot \mathbf{v} = \frac{\partial v_x}{\partial x} + \frac{\partial v_r}{\partial r} + \frac{v_r}{r}. \quad (2.12)$$

2.3 Boundary conditions

The unique solution of the governing partial differential equations requires the application of boundary conditions. Figure 2.3 shows the physical domain and its boundaries. The boundary conditions used in this study are described below.

2.3.1 Inlet boundary conditions

There are two steps in this study: CTC trapping in the filter funnel array and threshold pressure determination for CTCs of different cortical tension and size. For filter array simulations, the flow is pressure-driven. So, *pressure inlet* boundary

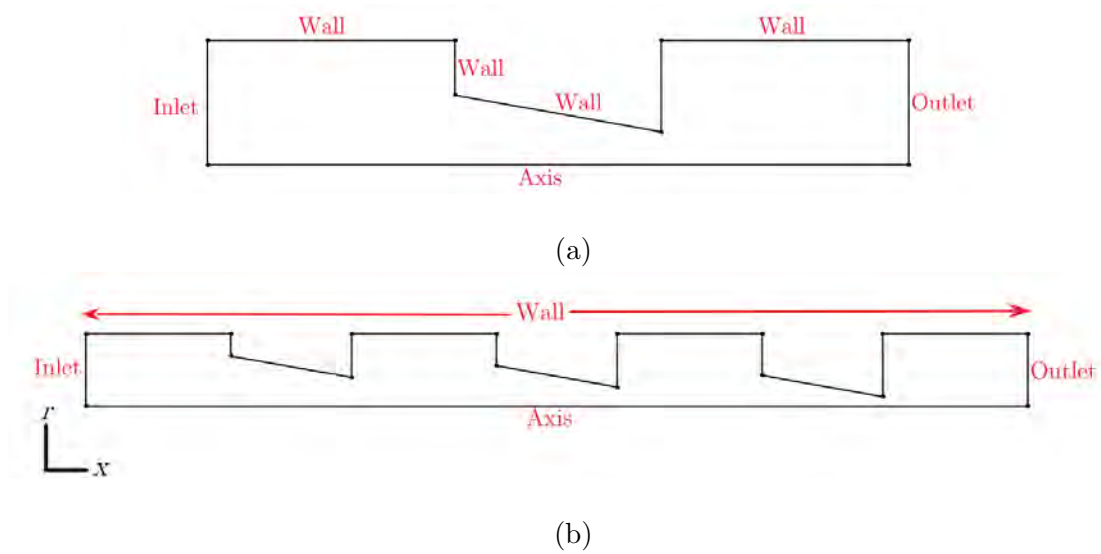


Figure 2.3: Boundary conditions.

condition was used where the total pressure is applied at the inlet. Mathematically,

$$P_0(t, r, 0) = P_1 \quad (2.13)$$

where P_0 is the total pressure and P_1 is the value of total pressure at the inlet. Two different values of P_1 were used: 100 Pa and 300 Pa. This leads to an adjustment of the flow rate when the CTC is deformed within a filter funnel. The values of P_1 were selected based on the experimental threshold values obtained by Guo et al. [58]. They reported threshold pressure values in the range of 40- 250 Pa for Mouse Lymphoma Cells (MLC). The reported cell diameter was 15.6 μm , and cell cortical tension was 0.75 mN/m, which is in the range of the values used in the present study.

For the second case, plasma is driven at a fixed flow rate, and the pressure required for a CTC to pass a filter funnel is recorded to determine the threshold pressure. For this case, the *velocity inlet* boundary condition was used where uniform plasma velocity was applied at the inlet. The flow direction was set to be normal to the inlet boundary. Mathematically,

$$v_n(t, r, 0) = v_1 \quad (2.14)$$

where v_n is the normal velocity and v_1 is the value of boundary normal velocity at inlet. The flow rate was fixed at 0.27 nL/s, which gives a uniform plasma velocity of $v_1 = 0.38$ mm/s at the inlet. For this boundary condition, the total pressure at the inlet is not fixed and will adjust to any value necessary to provide the required flow. For CTC passing, this leads to an adjustment of the pressure when the CTC is deformed within a filter funnel. For both velocity and pressure inlet boundary conditions, the volume fraction of the cell at the inlet was set to zero. This leads to only the flow of plasma through the inlet.

2.3.2 Wall boundary condition

The filter walls were modeled as stationary with no slip shear condition. No slip shear condition sets all the velocity components to be zero at the wall boundary,

$$\mathbf{v}_{\text{wall}} = 0. \quad (2.15)$$

In addition, a non-wetting wall contact angle, $\theta_w = 180^\circ$ was set between the CTC and the filter wall.

2.3.3 Outlet boundary condition

The outlets were modeled with pressure outlet boundary condition where a static gauge pressure of 0 Pa is set at the outlet. Mathematically,

$$P(t, r, x_{\text{exit}}) = 0 \quad (2.16)$$

where P is the static pressure and x_{exit} is the value of axial coordinate x at the exit. $x_{\text{exit}} = 85 \mu\text{m}$ for single filters $x_{\text{exit}} = 195 \mu\text{m}$ for the filter array. With the static pressure at the outlet set to zero, pressure or velocity at the inlet is calculated according to the applied inlet boundary condition. Flow reversals can occur at the pressure outlet, and the backflow CTC volume fraction was set to zero at the outlet.

Table 2.5: Summary of boundary conditions.

Boundary name	Boundary condition	\mathbf{v} (mm/s)	P (Pa)	P_0 (Pa)
Inlet	Pressure inlet	-	-	100, 300
	Velocity inlet	(0,0.38)	-	-
Outlet	Pressure Outlet	-	0	-
Wall	No slip condition with $\theta_w = 180^\circ$	(0,0)	-	-
Axis	Zero normal gradient of flow variables	(0, v_x)	-	-

2.3.4 Axis boundary condition

Axis boundary condition was set at the center line of the two-dimensional axisymmetric domain. Symmetry is enforced by setting the radial gradient of flow variables to zero on the axis,

$$\frac{\partial v_x}{\partial r}(t, 0, x) = 0, \quad (2.17)$$

$$\frac{\partial v_r}{\partial r}(t, 0, x) = 0, \quad (2.18)$$

$$\frac{\partial P}{\partial r}(t, 0, x) = 0. \quad (2.19)$$

In addition, the radial velocity is also taken to be zero on the axis,

$$v_r(t, 0, x) = 0. \quad (2.20)$$

Any value for a particular variable on the axis is taken from the nearest computational cell.

The boundary conditions used in this study are summarized in Table 2.5.

2.4 Cortical tension modeling

CTC cortical tension is modeled by the surface tension effect. For a tumor cell of given deformability, the cell cortical tension, σ is considered to be constant. The surface tension effects are modeled by the *Continuum Surface Stress (CSS)*

model. The CSS model treats the surface tension effects in a conservative manner. The force due to cell cortical tension depends on the curvature of the CTC phase boundary. In computing threshold pressure for CTC passing through a filter, the pressure signature depends on the accurate prediction of CTC deformation. CSS avoids the explicit calculation of curvature. In this method, the surface stress tensor due to cell cortical tension effects is written as:

$$\mathbf{T} = \sigma \left(\mathbf{I} - \hat{n} \otimes \hat{n} \right) |\vec{n}| \quad (2.21)$$

$$\vec{n} = \nabla \alpha \quad (2.22)$$

$$\hat{n} = \frac{\vec{n}}{|\vec{n}|} \quad (2.23)$$

where \mathbf{I} is the unit tensor, σ is the cell cortical tension, \otimes is the tensor product of the two vectors, α is the CTC volume fraction, and \vec{n} is the volume fraction gradient. Plugging in the expression of \vec{n} , Equation (2.21) can be written as

$$\mathbf{T} = \sigma \left(|\nabla \alpha| \mathbf{I} - \frac{\nabla \alpha \otimes \nabla \alpha}{|\nabla \alpha|} \right) \quad (2.24)$$

The force due to cell cortical tension, F_{CSS} is written as

$$F_{CSS} = \nabla \cdot \mathbf{T} \quad (2.25)$$

which gives

$$F_{CSS} = \nabla \cdot \left[\sigma \left(|\nabla \alpha| \mathbf{I} - \frac{\nabla \alpha \otimes \nabla \alpha}{|\nabla \alpha|} \right) \right] \quad (2.26)$$

The CSS method, thus, does not require any explicit computation of curvature and behaves physically around sharp corners in the flow domain.

2.4.1 Wall adhesion

During the passage through the filters, the CTC comes in contact with the filter walls. Due to this, the adjustment of CTC curvature near the wall is necessary. The cell is considered to be non-wetting with the filter wall. Thus the contact angle, θ_w between the filter wall and a CTC is taken to be 180° . Using work done by Brackbill et al. [104], this contact angle is used to adjust the surface normal in cells near the wall. This leads to the adjustment of the phase boundary surface curvature near the filter wall. The surface normal at the computational cell next to the wall can be written as:

$$\hat{n} = \hat{n}_w \cos \theta_w + \hat{t}_w \sin \theta_w \quad (2.27)$$

where \hat{n}_w and \hat{t}_w are the unit vectors normal and tangential to the wall, respectively. This surface normal determines the local curvature of the surface near a wall. The curvature then is used to calculate the source term that arises due to cortical tension effects.

2.5 Numerical simulation

The Numerical simulations were carried out using the commercial software ANSYS Fluent [105]. The numerical solution of the governing equations requires discretization of the governing equations. The discretization was done through the *Finite Volume Method (FVM)* where the integral form of the governing partial differential equations is cast into divisions of the computational domain, called control volumes. The divergence terms are converted into surface integrals using the divergence theorem. These surface integrals are then evaluated as fluxes through the surfaces of the control volumes. The steps followed are enlisted below:

- Division of the computational domain into discrete control volumes using a computational grid.

- Integration of the governing equations on the individual control volumes, which results in algebraic equations for the discrete dependent variables like velocity, pressure, etc.
- Linearization of the discretized equations solution of the linear system of equations to find values of the dependent variables.

2.5.1 Pressure-based segregated algorithm

The governing equations were solved using the pressure-based segregated algorithm. The momentum conservation does not provide an equation for pressure evolution. Rather the constraint of mass conservation (the continuity equation) of the velocity field is satisfied by solving a pressure correction equation. This equation is derived from the continuity and the momentum equation in such a way that the velocity field corrected by pressure satisfies the continuity equation. In the segregated algorithm, the governing equations are solved sequentially for the solution variables v_r, v_x , etc. Since the equations are nonlinear and coupled, an iterative solution loop is carried out to obtain a converged solution. The iteration steps are illustrated in Figure 2.4.

The steps can be enlisted as:

1. Update fluid properties (e.g., density, viscosity, etc.) based on the current solution.
2. Solve the momentum equations sequentially with recently updated pressure and face mass flux values.
3. Solve the pressure correction equation using the recently obtained velocity field and mass flux.
4. Correct face mass flux, pressure, and the velocity field using the corrected pressure obtained in step 3.
5. Solve for additional scalars, if any.

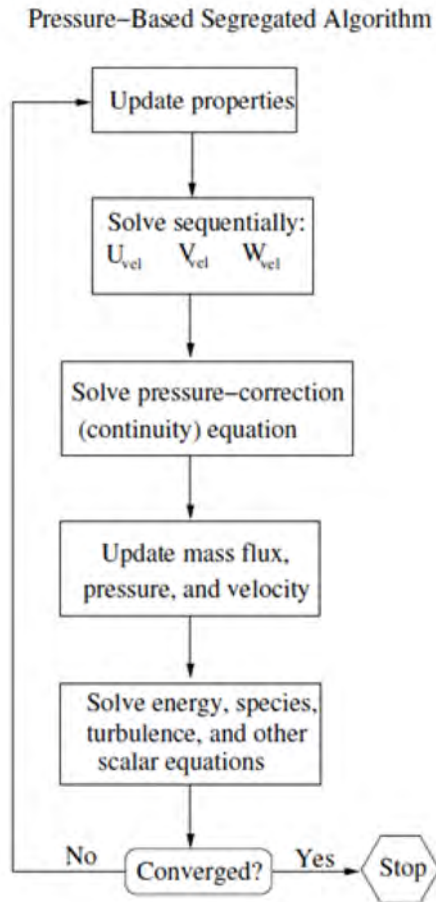


Figure 2.4: Overview of the pressure based segregated algorithm.

6. Update the source terms arising from the interactions among different phases.
7. Check for the convergence of the equations.

The iterative loop is continued until the convergence criteria are satisfied.

2.5.2 Spatial discretization

The momentum conservation equation (2.3) can be written in the integral form as:

$$\int_V \frac{\partial \rho \mathbf{v}}{\partial t} dV + \oint \rho \mathbf{v} \mathbf{v} \cdot d\mathbf{A} = - \oint p \mathbf{I} \cdot d\mathbf{A} + \oint \mathbf{T} \cdot d\mathbf{A} + \int_V \mathbf{F} dV, \quad (2.28)$$

where the gravity term is neglected. This equation is applied to each control volume in the computational domain. The semi discretized form is expressed as:

$$\frac{\partial \rho \mathbf{v}}{\partial t} V + \sum_f^{N_{faces}} \rho_f \mathbf{v}_f \mathbf{v}_f \cdot \mathbf{A}_f = - \sum_f^{N_{faces}} p_f \mathbf{A}_f + \sum_f^{N_{faces}} \mathbf{T}_f \cdot \mathbf{A}_f + \mathbf{F}V, \quad (2.29)$$

where, N_{faces} is the number of faces enclosing a cell, subscript f denotes values of the variables on the faces, \mathbf{A}_f is the area of a face and V is the cell volume. A representative 2D triangular control volume is shown in Figure 2.5 as example.

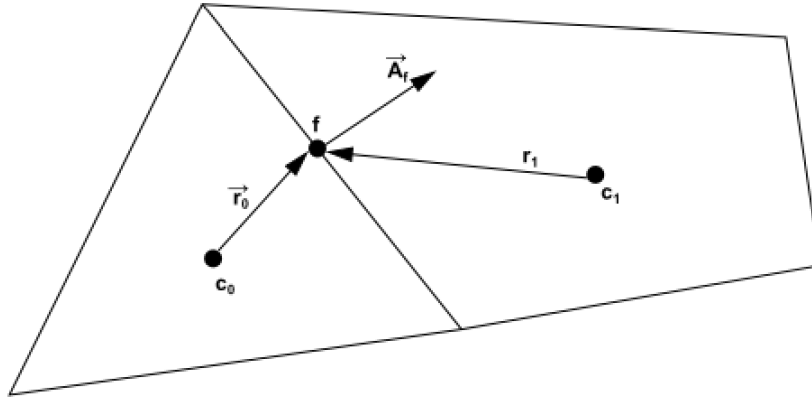


Figure 2.5: Control volume for illustrating spatial discretization of the momentum equation.

$\frac{\partial \rho \mathbf{v}}{\partial t} V$ is defined in Section 2.5.4. The discretized equation contains unknown variables at the cell center along with values at the cell faces which can be calculated from the surrounding cells. A linearized form of the equation can be written as:

$$a_P \phi = \sum_{nb} a_{nb} \phi_{nb} + b \quad (2.30)$$

where ϕ can take the value of any of the velocity components, the subscript nb refers to neighboring cells, and a_P and a_{nb} are linearized coefficients of ϕ_{nb} . Similar equations can be written for each cell in the computational domain. This results in a set of algebraic equations, which is solved by point implicit Gauss-Seidel linear equation solver in conjunction with the Algebraic Multigrid method.

The Equation (2.29) requires face values of flow variables for the convective terms. These values are interpolated from the cell center values using an upwinding scheme.

In this scheme, the face value ϕ_f is obtained from the cell upstream relative to the normal velocity, v_n . The second order upwind scheme is used for the momentum equation, where quantities at the cell face are calculated through a Taylor series expansion of the cell-centered solution about the cell centroid. The face value is computed using the following expression:

$$\phi_{f,SOU} = \phi + \nabla\phi \cdot \vec{r} \quad (2.31)$$

where, ϕ and $\nabla\phi$ are the cell centered value and its gradient in the upstream cell respectively and \vec{r} is the displacement vector from the upstream cell centroid to the face centroid. This requires the determination of gradients, which is calculated by the least squares cell based method.

The Equation (2.30) can be solved to obtain the velocity field if the pressure field and the mass fluxes are known. However, pressure and mass fluxes are not known prior to the solution. To obtain the pressure at the face PRESTO! (PREssure STaggering Option) an interpolation scheme is used, which uses the discrete continuity balance for a control volume about the face to compute pressure.

The continuity equation (2.2) can be written in the conservative form as:

$$\int_V \frac{\partial \rho}{\partial t} dV + \oint \rho \mathbf{v} \cdot d\mathbf{A} = 0 \quad (2.32)$$

Integrating over a control volume, the semi discretized form can be written as:

$$\int_V \frac{\partial \rho}{\partial t} dV + \sum_f^{N_{faces}} J_f A_f = 0 \quad (2.33)$$

where J_f is the mass flux through face f , ρv_n . To find the face values of velocities v_n from the velocity at the cell centers, a momentum weighted averaging using weighted factors is performed. The factors can be taken by writing equations for the velocity components similar to the Equation (2.30).

2.5.3 Pressure velocity coupling

As discussed in Section 2.5.1, the conservation equations 2.2 and 2.3 does not contain an equation for pressure evolution. The *Semi-Implicit Method for Pressure Linked Equations (SIMPLE)* algorithm obtains pressure field through a pressure correction scheme by enforcing mass conservation. In this process, both the cell pressure and face flux are corrected. The corrected flux satisfies the discretized conservation equation during each iteration. For the current study, however, the Pressure-Implicit with Splitting of Operators (PISO) algorithm was used for pressure velocity coupling. PISO is a part of the SIMPLE family of algorithms. One of the limitations of the SIMPLE algorithm is that the new velocities and fluxes do not satisfy the momentum equation after solving the pressure correction equation. As a result, calculations are repeated until a balance is obtained. PISO algorithm improves the efficiency of this calculation by performing additional momentum and skewness corrections.

2.5.4 Temporal Discretization

Temporal discretization involves the time integration of the terms of a differential equation to obtain the solution at different time steps. First order accurate implicit method was used for temporal discretization. The generic form of an equation for the time evolution of a variable ϕ can be written as:

$$\frac{\partial \phi}{\partial t} = F(\phi) \quad (2.34)$$

The first order accurate implicit temporal discretization is then given by:

$$\frac{\phi^{p+1} - \phi^p}{\Delta t} = F(\phi^{p+1}), \quad (2.35)$$

where the superscript p indicates value at the current time level and the superscript $p + 1$ indicates value at the next time level. The value of ϕ^{p+1} in a given computational cell is related to ϕ^{p+1} in the neighboring cells through $F(\phi^{p+1})$. Equation

(2.35) can be rearranged as:

$$\phi^{p+1} = \phi^p + \Delta t F(\phi^{p+1}) \quad (2.36)$$

This is an implicit equation and can be solved iteratively at each time step before moving to the next step. The fully implicit scheme is unconditionally stable. Cancer cell passing events through the microfilters required variable time stepping. The time step size was in the range of 10 μ s- 0.1 μ s.

2.6 Interface capturing

The current study considers a two-phase flow between a tumor cell and blood plasma. The cell membrane is represented by the interface of the two phases. Numerical schemes to resolve material interfaces can be classified into two categories: interface tracking and interface capturing methods. Interface tracking methods [106, 107] track the evolution of the interface as a sharp discontinuity. Any interfacial physics like surface tension effects can be very easily incorporated. But these methods are not discretely conservative at the interface. On the other hand, interface capturing methods [108, 109] can achieve discrete conservation by solving the governing equations in the conservative form. But these methods smear the material interface over a small region. In this study, the *Volume of Fluid (VOF)* method [110] is employed for interface capturing. The sharp interface is ensured by using the *Geometric reconstruction* scheme.

2.6.1 The VOF model

The VOF model solves a single set of momentum equations for two or more immiscible phases. The volume fraction of each of the phase is tracked throughout the computational domain. The sum of the volume fraction of all the phases is unity.

$$\sum_{i=1}^n \alpha_i = 1, \quad (2.37)$$

where α_i is the volume fraction. Thus, three different scenarios are possible for a cell:

1. $\alpha_i = 0$: the cell is empty of the i^{th} phase.
2. $0 < \alpha_i < 1$: the cell has an interface between the i^{th} and one or more other phases.
3. $\alpha_i = 1$: the cell is full of the i^{th} phase.

All the fluid properties in a cell are averaged by volume fraction values. The following rules are applied respectively for density and viscosity:

$$\rho = \sum_{i=1}^n \alpha_i \rho_i, \quad (2.38)$$

$$\mu = \sum_{i=1}^n \alpha_i \mu_i. \quad (2.39)$$

The interface is confined to thin regions in space. In these regions, fluid properties are thus representative of a mixture of the phases. A volume fraction cutoff of 10^{-6} is used. For two phases, this represents that a cell is purely comprised of one of the phases if the other phase volume fraction is below the cutoff.

2.6.1.1 The volume fraction equation

To capture and evolve the interface between the phases, a transport equation is solved for the volume fraction of one or more of the phases. The equation takes the following form:

$$\frac{1}{\rho_i} \left[\frac{\partial}{\partial t} (\alpha_i \rho_i) + \nabla \cdot (\alpha_i \rho_i \mathbf{v}_i) = S_{\alpha_i} + \sum_{j=1}^n (\dot{m}_{ji} - \dot{m}_{ij}) \right], \quad (2.40)$$

where S_{α_i} is the source term, \dot{m}_{ij} is the mass transfer from phase i to phase j and \dot{m}_{ji} is the mass transfer from phase j to phase i . For this study, there is no production or transfer of mass between the phases. Hence, all these terms are set

to zero. Since volume fractions sum to unity, one of the methods is to solve $n - 1$ equations for $n - 1$ phases. The primary phase volume fraction can be computed from the constraint.

The transport equation for volume fraction is solved with the explicit scheme. The conservative form of Equation (2.40) can be written as:

$$\int_V \frac{\partial \alpha_i \rho_i}{\partial t} dV + \oint \alpha_i \rho_i \mathbf{v}_i \cdot d\mathbf{A} = \int_V \left[S_{\alpha_i} + \sum_{j=1}^n (\dot{m}_{ji} - \dot{m}_{ij}) \right] dV, \quad (2.41)$$

which can then be written in the discretized form as:

$$\frac{\alpha_i^{p+1} \rho_i^{p+1} - \alpha_i^p \rho_i^p}{\Delta t} V + \sum_f (\rho_i U_f^p \alpha_{i,f}^p) = \left[S_{\alpha_i} + \sum_{j=1}^n (\dot{m}_{ji} - \dot{m}_{ij}) \right] V, \quad (2.42)$$

where $p + 1$ is the index for the new time step, p is the index for the previous time step, $\alpha_{i,f}$ is the value of the i^{th} volume fraction on the faces of the cell, $V =$ is the volume of the cell and $U_f =$ is the volume flux through the face, based on normal velocity.

2.6.2 The geometric reconstruction scheme

Standard interpolation schemes outlined in Section 2.5.2 are used to obtain face fluxes whenever a cell is fully occupied by one phase. But when a cell is near the interface between two phases, the geometric reconstruction scheme is used. This scheme represents the interface between two phases assuming that the interface has a linear slope (Figure 2.6) within each cell and uses this linear slope for the computation of fluid advection through the faces.

The steps followed in this scheme are:

- Calculating the position of the linear interface relative to the centroid of each partially filled cell based on the information about the volume fraction and its derivatives.

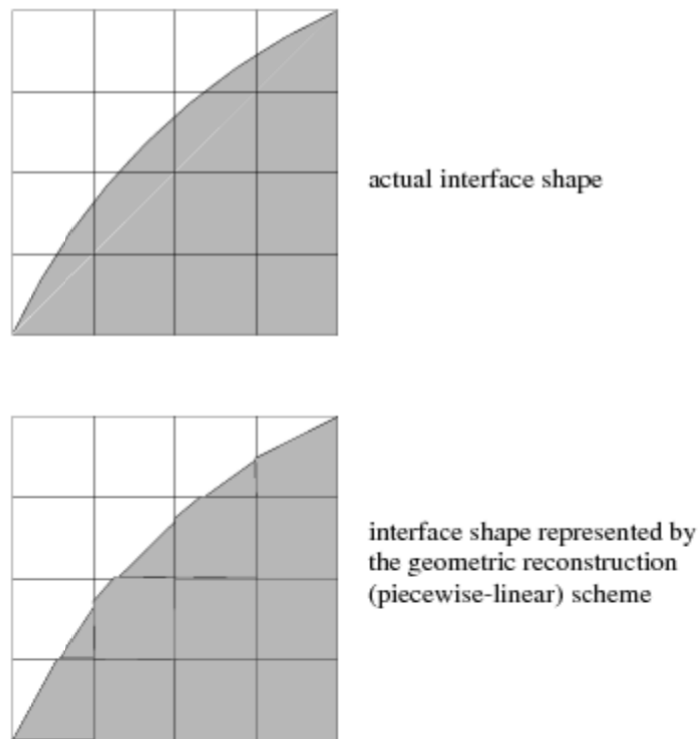


Figure 2.6: Interface calculation by the geometric reconstruction scheme.

- Calculating the advecting amount of fluid through each face using the computed linear interface representation and velocity distribution on the face.
- Calculating the volume fraction in each cell by using the balance of mass fluxes.

2.7 Discretization of the computational domain

The computational domain has to be discretized to form control volumes to which the discretized form of the governing equations are applied. Discretization is performed by using structured multi-block mesh. Mesh for filter array simulation is shown in Figure 2.7, with the enlarged view showing computational cells at the funnel constriction. The total number of cells for the single filter mesh is about 40000. While in the filter array mesh, the number of cells is about 2.5 times that of a single filter.

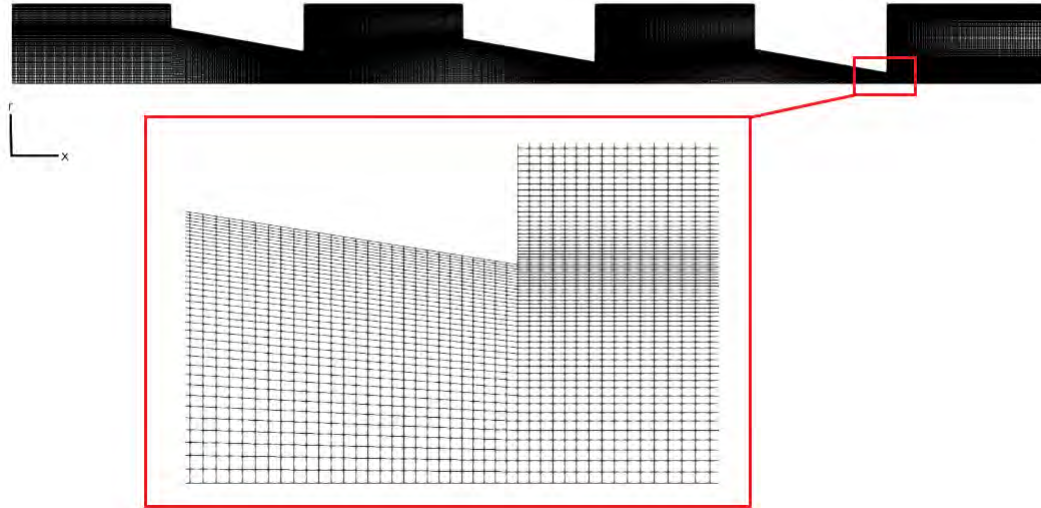


Figure 2.7: Mesh of the filter array computational domain.

2.8 Validation and verification

Results from numerical simulation need to be validated against experimental data. The physical model and its solution procedure adopted in this study have been validated against micropipette aspiration experimental data from Evans et al. [76]. They obtained the threshold pressure required to form initial hemispherical projections of blood granulocytes inside pipets. Based on a theoretical correlation, they measured a cortical tension, $\sigma = 0.035$ mN/m in the cell cortex. The average cell diameter was measured as $8.5 \mu\text{m}$. They used pipettes with a diameter ranging from 2- $8 \mu\text{m}$. 2D axisymmetric geometry was chosen to replicate the experimental conditions. The cell was driven to the micropipette by setting a fixed flow rate at the inlet. Threshold pressure was calculated by the procedure outlined in Section 4.2. Threshold pressure, $P_{\text{threshold}}$ values for different pipet diameter is presented in Figure 2.8. The simulation results are found to be in agreement with the experimental data. A slight discrepancy is found for the pipet with the smallest diameter.

To quantify the independence of the solution upon grid resolution, systematic testing has been performed according to the method presented by Roach et al. [111, 112]. The procedure is also described by Khan et al. [113]. Three different grids were

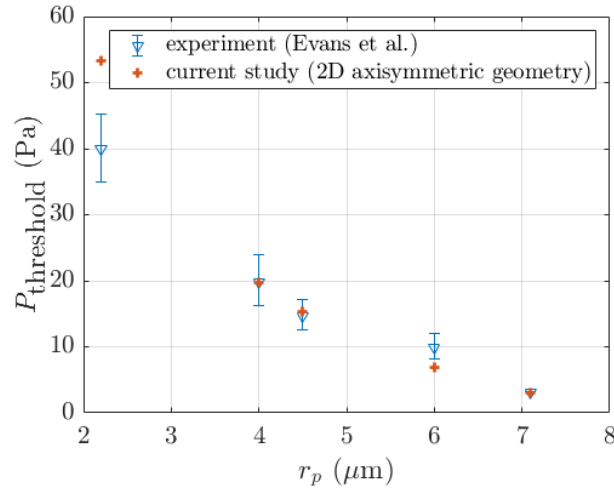


Figure 2.8: Comparison of threshold pressure required to deform a blood granulocyte.

Table 2.6: Number of cells for the grids used for grid convergence test.

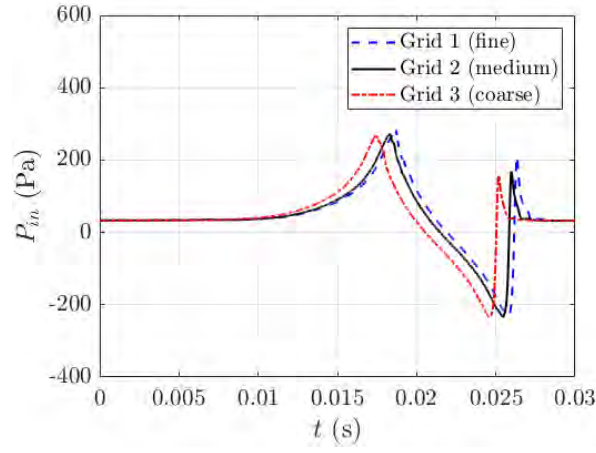
Grid	Number of cells
Grid 1 (fine)	73,396
Grid 2 (medium)	37,125
Grid 3 (coarse)	18,752

selected, having three different resolutions with a non-integer grid refinement ratio, r_g of 1.41. Table 2.6 gives the number of cells in each grid. The value of r_g was kept the same in both the r and x directions. The single filter case selected for the test has $r_f = 4 \mu\text{m}$, $\sigma = 1.1 \text{ mN/m}$ and $D = 16 \mu\text{m}$. The boundary conditions were kept the same as described in Section 2.3. Inlet pressure history shown in Figure 2.9 (a) was compared between the three grids.

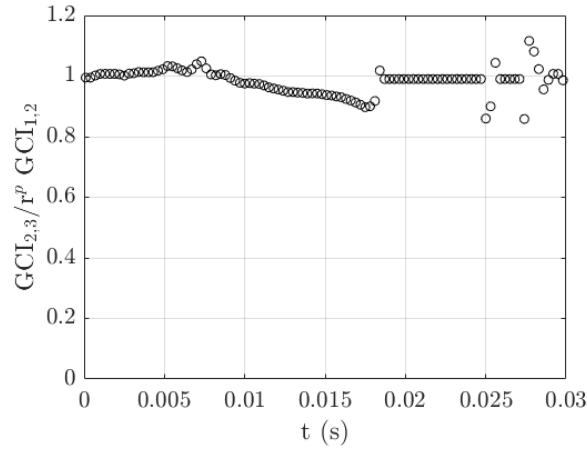
The solution order of accuracy is calculated from the pressure history using the following equation:

$$p = \frac{\ln\left(\frac{f_3 - f_2}{f_2 - f_1}\right)}{\ln(r_g)}, \quad (2.43)$$

where f_3 , f_2 and f_1 are inlet total pressure magnitude for grid 1, grid 2 and grid 3 at different times, t . A grid convergence index, GCI is calculated based on generalized Richardson extrapolation index for comparing discrete solution from two different



(a)



(b)

Figure 2.9: (a) Inlet pressure history for grids of three different resolution, (b) Calculated range of convergence.

grids. GCI is defined as,

$$\text{GCI}_{i,i+1} = \frac{F_s |\varepsilon|}{r_g^p - 1} \quad (2.44)$$

where ε indicates the change in solution between two grids. ε is given by,

$$\varepsilon = \frac{f_{i+1} - f_i}{f_i}. \quad (2.45)$$

Index i takes the values 1 or 2 for the three grids. F_s is a safety factor recommended by Roach et al. [111, 112] F_s is set to be 1.25. $\text{GCI}_{2,3}$ is calculated from the pressure histories of grid 2 and grid 3. Similarly, $\text{GCI}_{1,2}$ is calculated from grid 1 and grid 2. The values are used to calculate range of convergence (RC) which is defined by

$\frac{GCI_{2,3}}{r_g^p GCI_{1,2}}$. The range of convergence values at different times, t are shown in the Figure 2.9 (b). Despite having some noises, the values are mostly close to the value of the asymptotic range of convergence, unity. It is concluded that the solution is independent of grid resolution, and grid 2 is used for all single filter calculations. Grids for array simulations are also generated based on this single filter grid.

Chapter 3

CTC Isolation and Sorting by Pressure Driven Flow

3.1 CTC passing phenomena in a filter funnel: deformability analysis

To design a microfilter device for trapping circulating tumor cells (CTCs), it is important to understand the fundamentals of cell deformation in a single filter. As a cancer cell deforms during its passage through the filter, fluid dynamic variables like pressure or flow rate change according to the deformed state of the cell. In this section, CTC passing through a single conical filter under constant flow rate and constant total pressure are described in detail. Similar descriptions are provided in previous works [71, 73].

3.1.1 CTC deformation under constant flow rate

The pressure-deformability behavior for a CTC under constant flow rate is shown in Figure 3.1. Before approaching the filter funnel the total inlet pressure, P_{in} is constant. But as the cell approaches the filter funnel, it gets deformed, and P_{in} starts to increase. This is because, before the cell gets deformed in the funnel,

P_{in} is equal to the viscous pressure drop required to drive the flow through the funnel. But as the cell starts to deform, more pressure is required in addition to the viscous pressure drop. For constant inlet flow rate, P_{in} can be decomposed into two components:

$$P_{\text{in}} = P_{\text{viscous}} + P_{\text{cortical-tension}} \quad (3.1)$$

Initially, P_{in} is equal to P_{viscous} , which remains constant. But as the cell starts deforming in the funnel from an undeformed state, $P_{\text{cortical-tension}}$ changes from its zero initial value. At the instant when P_{in} is maximum, cell frontal curvature is at the minimum (inset (b) in Figure 3.1) and $P_{\text{cortical-tension}}$ is also at the maximum. As the cell continues to move through the funnel, P_{in} starts decreasing and drops to a value below the initial value of P_{in} . This is because as the cell comes out of the funnel, curvature at the back of the cell decreases to a minimum and $P_{\text{cortical-tension}}$ becomes negative (inset (c) in Figure 3.1). The cell rapidly draws its tail from the funnel and after coming out of the filter funnel, it starts recovering to its undeformed state. At this instant $P_{\text{cortical-tension}}$ increases again towards zero. But a second pressure peak can be seen just after the cell comes out of the funnel (inset (d) in Figure 3.1). This happens because after rapidly drawing its tail out of the funnel there is a recoil of the cell and the back portion of the cell flattens out. After this, the cell recovers its undeformed state and $P_{\text{cortical-tension}}$ becomes zero again. This means P_{in} becomes equal to P_{viscous} (inset (e) in Figure 3.1).

3.1.2 CTC deformation in pressure driven flow

In contrast to Section 3.1.1, CTC passing under constant pressure is discussed here. The ideas presented in the previous section are equally applicable here. In response to a constant inlet total pressure P_{in} , the flow rate, Q varies as the cell deforms through a funnel. The pressure deformability behavior is shown in Figure 3.2. In the undeformed state, the flow rate is constant (inset (a) in Figure 3.2). We can use Equation 3.1 here. But in this case P_{in} is constant. When $P_{\text{cortical-tension}}$ changes

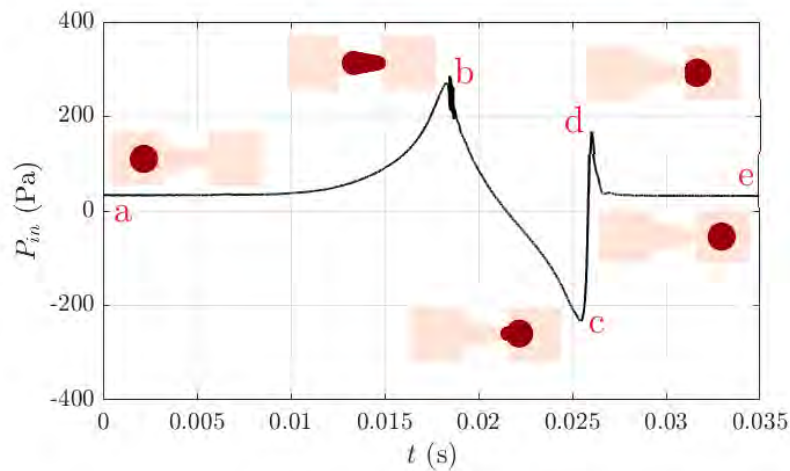


Figure 3.1: Pressure-deformability behavior of a CTC passing through a single conical microfilter. Insets a- e shows cell deformation states at various instants.

at different deformed state, P_{viscous} also has to change. This leads to a change in flow rate. When $P_{\text{cortical-tension}}$ increases, P_{viscous} decreases along with flow rate and vice-versa. As the cell starts deforming in the filter funnel, $P_{\text{cortical-tension}}$ increases, and the flow rate, Q starts to decrease. Insets (b-d) in Figure 3.2 can be directly contrasted with insets (b-d) in Figure 3.1. Here flow rate increases again to a peak when the cell draws its tail from the filter funnel (inset (c)). The same recoiling phenomenon can be seen here, which leads to a depression in flow rate (inset (d)). For the constant flow rate case, the cell must pass through the funnel, and P_{in} adjusts accordingly. But for pressure-driven flow, the applied inlet pressure may be insufficient to deform the cell enough that it can pass through the funnel (insets (e) and (f) in Figure 3.2). In such scenario, the cell reaches a maximum deformed state under the given inlet pressure and P_{in} equals $P_{\text{cortical-tension}}$. This means P_{viscous} becomes zero along with flow rate, Q . Without an increase in inlet pressure, the cell is trapped in the funnel. This leads to the cell trapping phenomena in filter funnels under pressure-driven flow.

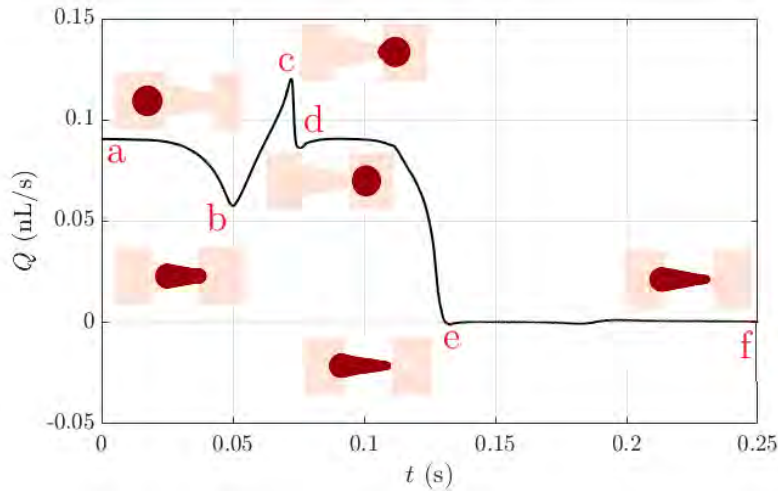


Figure 3.2: Flow rate-deformability behavior of a CTC passing through a single conical microfilter. Insets a- f shows cell deformation states at various instants.

3.2 CTC trapping in a microfluidic filter array

A filter array is formed by connecting single filters in series with decreasing filter pore radius, r_f . Similar filter arrays were used by Aghaamoo et al. [73], but all the filter funnels in their design had the same filter pore radius, r_f . Pressure driven flow is considered for two different values of inlet driving pressure, P_{in} , 100 Pa and 300 Pa. The computational parameters are given in Section 2.1.5. For four different combinations of cortical tension, σ and three different combinations of cell diameter, D , 24 different cases were simulated. The 100 Pa cases were all simulated for a physical time of 0.4 s, whereas the 300 Pa cases for 0.15 s. The flow rate and cell position history for the case $P_{in} = 100$ Pa, $\sigma = 0.2$ mN/m and $D = 16$ μm is shown in Figure 3.3(a). In contrast to [73], only forward driving pressure was considered. Cell position is calculated by the axial position of the center of mass of the cell. Due to symmetry, the radial position of the center of mass is zero. Cell volume fractions at different instants are also presented to show cell physical position and deformation. For the case shown in Figure 3.3, the cell passes through filters 1 and 2. The flow rate history and cell volume fraction show the typical characteristics discussed in Section 3.1.2. But the 100 Pa inlet pressure is insufficient for the cell to pass through filter 3. As a result, the cell gets trapped in the funnel as indicated

by its constant position from just before $t= 0.3$ s. The flow rate, Q , also drops to zero. The cell in its trapped position can be viewed in Figure 3.3(h).

In contrast to the previous case, the cell passes through all the filters for the case shown in Figure 3.4. For this case, the inlet driving pressure is 300 Pa while the other parameters are kept the same. This pressure is sufficient to deform the cell enough so that it can pass through filter 3. Cell position keeps increasing as the cell traverses the funnels. The same cell thus can be either trapped in a funnel or can pass through the filter device depending upon the inlet pressure. Under 300 Pa cell deformation, cell recoil is quite significant (Figure 3.4(h)). The cell has a higher velocity through the filter funnels under 300 Pa pressure and draws its tail out of the funnel much more rapidly. This leads to significant deformation under recoil. Filter 3 has much less volume within the funnel in comparison to filter 1 and 2. As a result, when passing through filter 3, the cell is highly deformed (Figure 3.4(h)). Also, comparing the similar states between 3.3 and 3.4, by the time there is a trough in flow rate, Q , the cell has advanced further forward in the 300 Pa case.

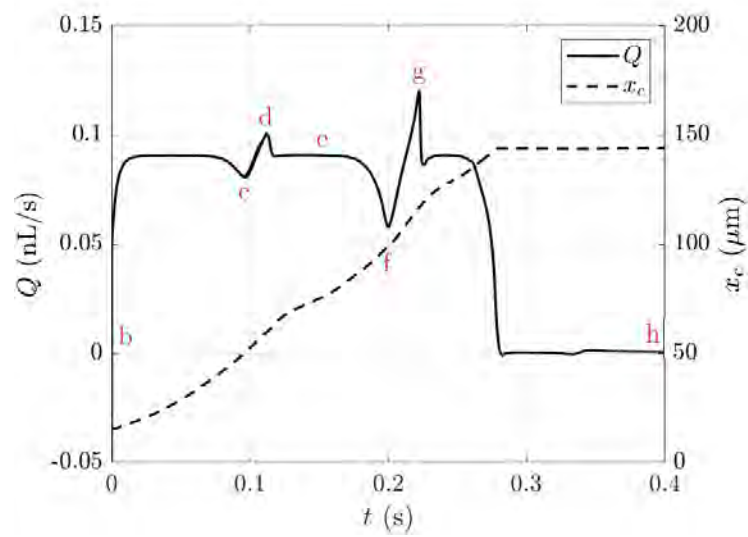
Figures 3.5 and 3.6 show the cases for $\sigma= 0.4$ mN/m and $D = 20$ μm . This cell is stiffer and larger than the previous two cases. Under 100 Pa inlet pressure, the cell gets trapped in filter 2. But under 300 Pa pressure, it passes through all the filter funnels. The difference with the previous case is that under 100 Pa pressure, the cell gets trapped in filter 2. Whereas the previous cell being softer and smaller, got trapped in filter 3. Again, the cell is highly deformed in filter 3.

Figures 3.7 and 3.8 show the cases for $\sigma= 1.1$ mN/m and $D = 16$ μm . Thus the cell is stiffer than the previous two cells. Under 100 Pa inlet pressure, the cell gets trapped in filter 2 while under 300 Pa pressure, it gets trapped in filter 3. In comparison to the previous cases, a higher value of cortical tension has resulted in the cell being trapped earlier in funnels with larger values of r_f . In the previous cases, the cell did not get trapped under 300 Pa pressure. But in this case, the cell gets trapped even at the higher of the two driving pressures. The stiffest cell so far ($\sigma= 2$ mN/m) is showcased in Figures 3.9 and 3.10. But the cell is the smallest one with $D= 12$ μm . Despite being the stiffest, the cell is trapped in filter 2 for

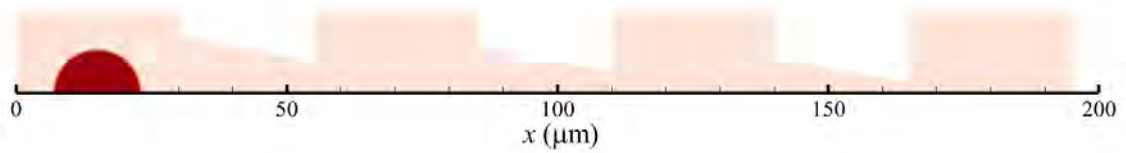
100 Pa inlet pressure. As the filter pore radius, r_f is $6 \mu\text{m}$, the $12 \mu\text{m}$ diameter cell can easily pass through filter 1 with very small changes in flow rate. For 300 Pa pressure, the cell gets trapped in filter 3. Despite being stiffer than the previous two cases, this cell is also much smaller. Thus cell trapping pattern in funnels is the same. This indicates cell size-dependent trapping along with cell cortical tension.

The rest of the Figures from 3.11 to 3.2 show cell position and flow rate history for the remaining cases. For a few of the cases, the cell gets through all the funnels. This occurs for softer cells. In other cases, cell trapping is achieved in different funnels depending upon P_{in} , σ and D . A few of the largest or stiffest cells even get trapped in filter 1.

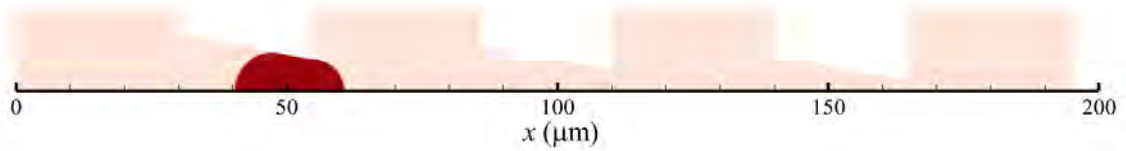
Guo et al. [58] did an experimental study of Mouse Lymphoma Cell (MLC) motion under oscillatory pressure in a funnel chain. The funnels had the same geometric parameters with the pore size set at $6 \mu\text{m}$. They observed cell displacement with different pressure amplitude at a fixed frequency and different frequencies at a fixed amplitude. Ratcheting motion was observed when the applied pressure surpassed threshold pressure. When the applied pressure was not sufficient, cells were found to be oscillating in the same confinement. On the other hand, in frequency studies, the cells were confined when the frequency was too high. Higher frequencies did not provide sufficient time to traverse a funnel. But higher frequencies enabled cell movement through funnel constrictions. Aghaamoo et al. [73] computationally studied cell motion and deformation through filter funnel array with same filter pore size. Their study was similar to [58]. They reported rectified ratcheting in the funnel array. But no cell trapping phenomena was reported. Confinement for cells of different physical properties was also not reported.



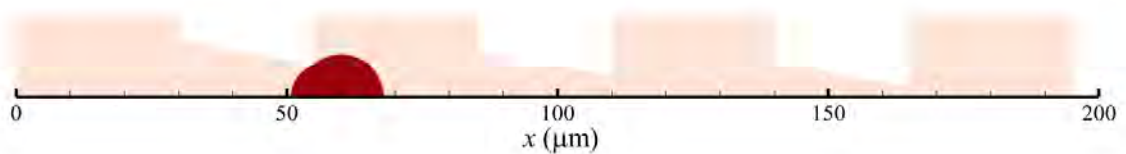
(a)



(b)



(c)



(d)

Figure 3.3: (a) flow rate and cell position history for the case: $P_{in} = 100$ Pa, $\sigma = 0.2$ mN/m and $D = 16$ μm , (b)-(h) cell volume fraction showing cell position and deformation at different times during passage through the filter. (cont.)

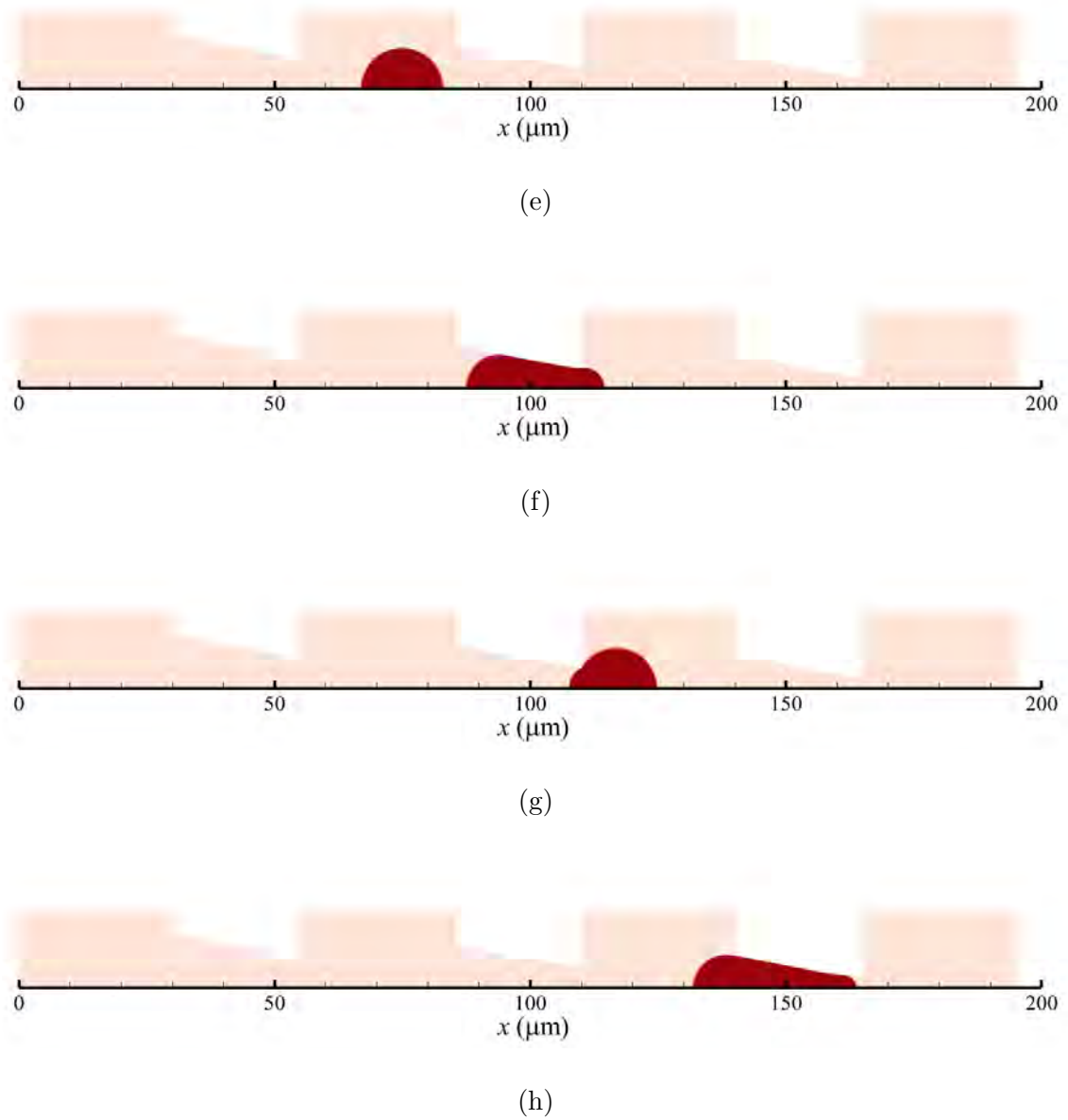
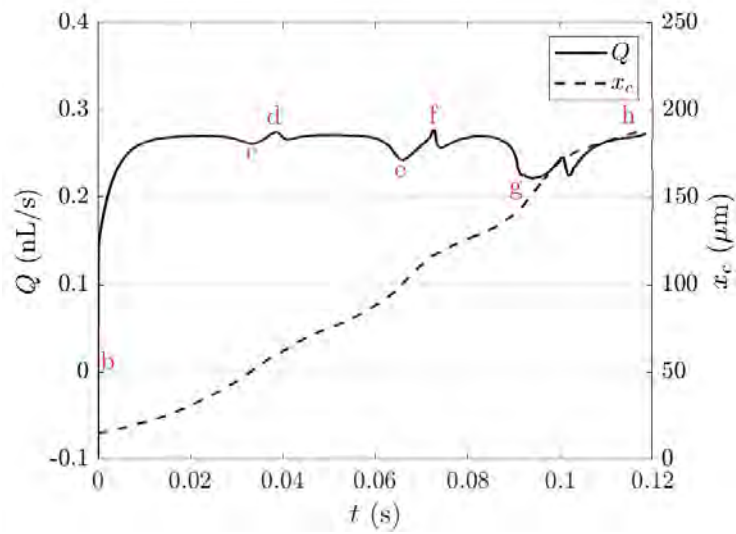
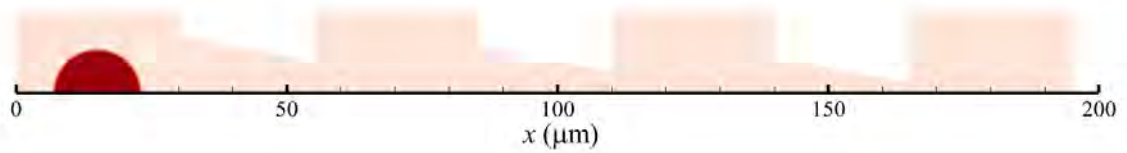


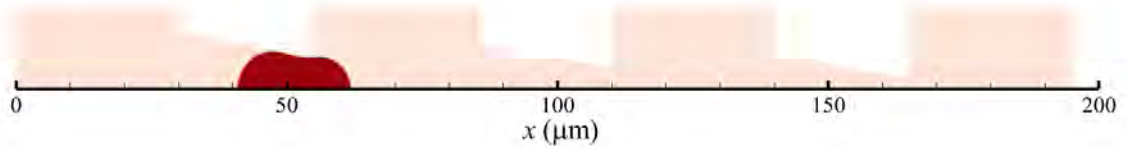
Figure 3.3: (a) flow rate and cell position history for the case: $P_{in} = 100$ Pa, $\sigma = 0.2$ mN/m and $D = 16$ μm , (b)-(h) cell volume fraction showing cell position and deformation at different times during passage through the filter.



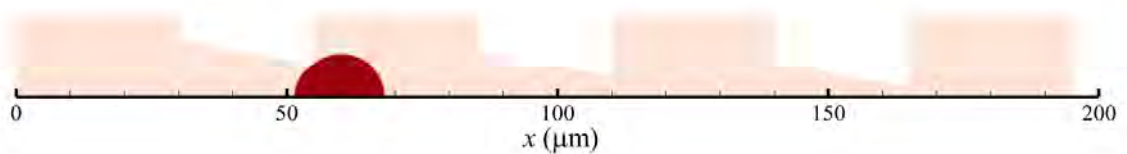
(a)



(b)



(c)



(d)

Figure 3.4: (a) flow rate and cell position history for the case: $P_{in} = 300$ Pa, $\sigma = 0.2$ mN/m and $D = 16$ μm , (b)-(h) cell volume fraction showing cell position and deformation at different times during passage through the filter. (cont.)

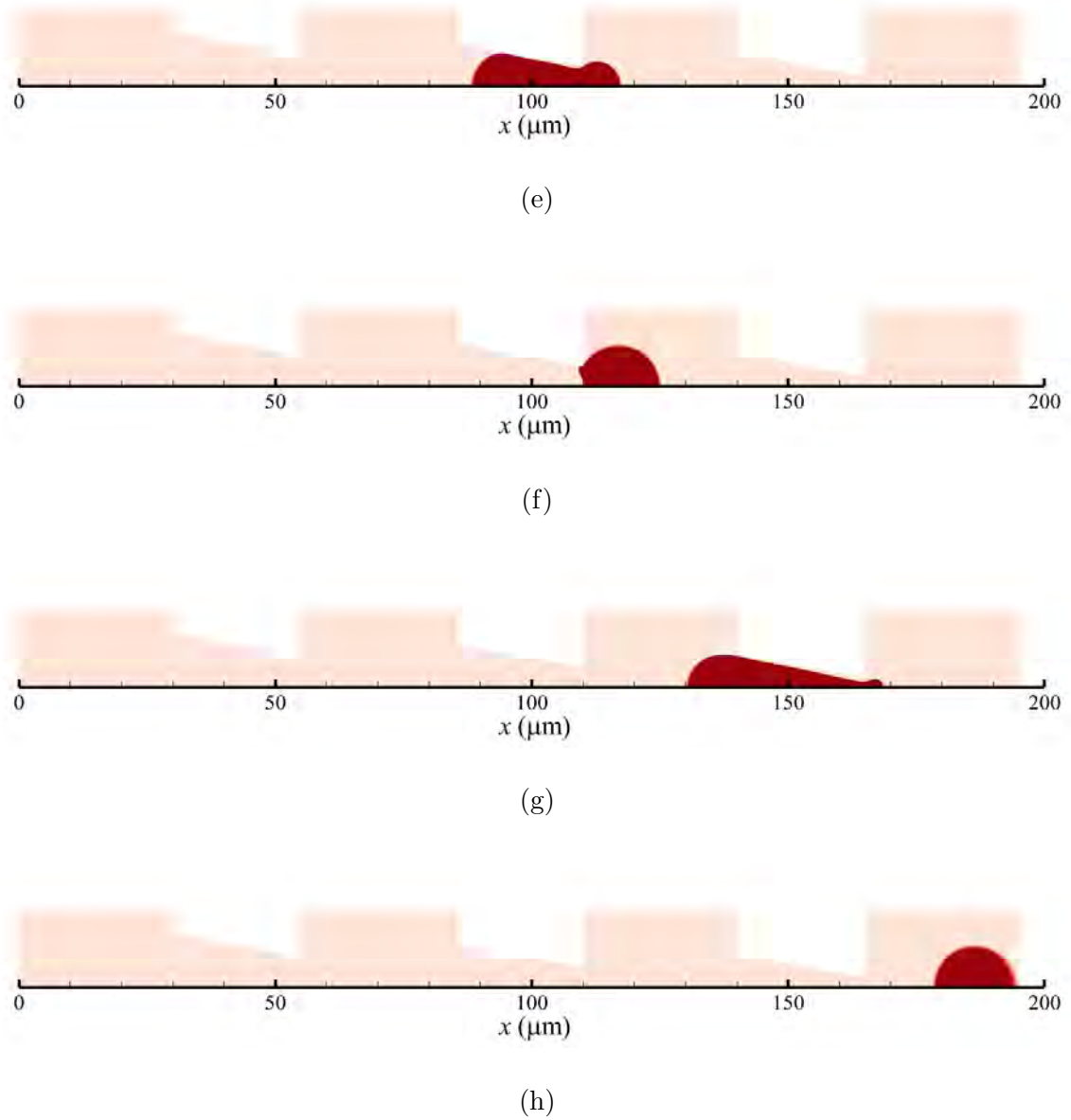
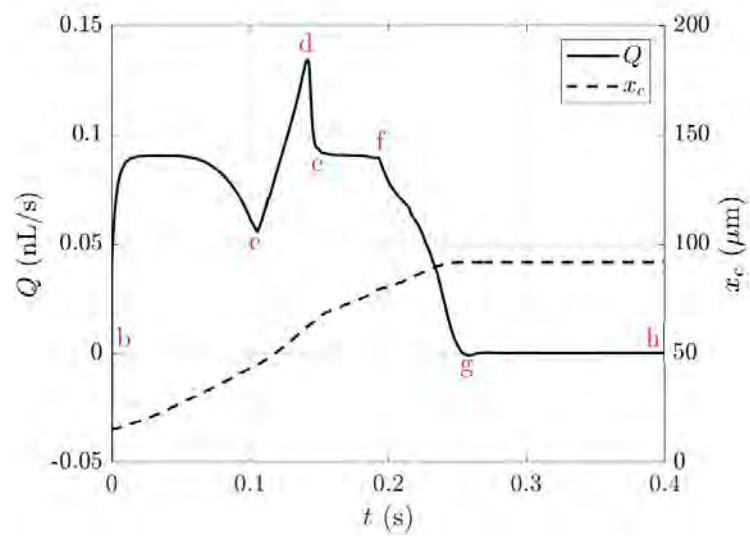
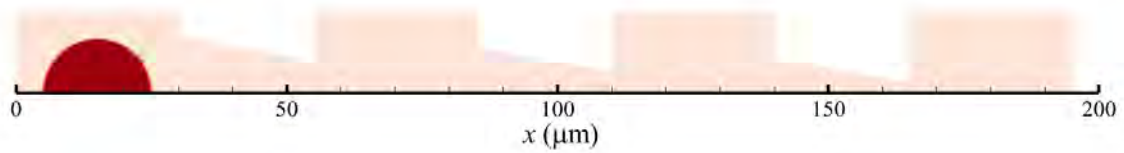


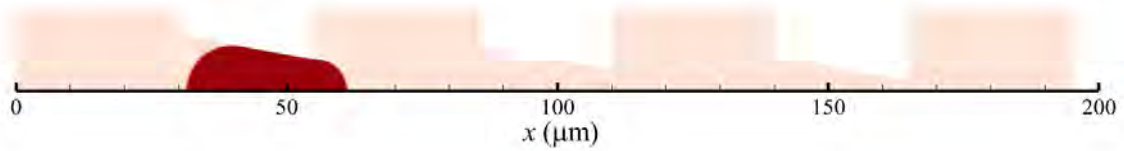
Figure 3.4: (a) flow rate and cell position history for the case: $P_{in} = 300$ Pa, $\sigma = 0.2$ mN/m and $D = 16$ μm , (b)-(h) cell volume fraction showing cell position and deformation at different times during passage through the filter.



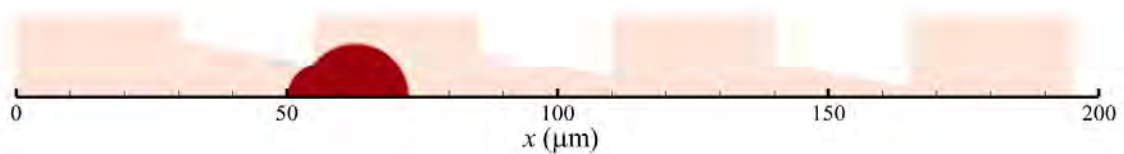
(a)



(b)

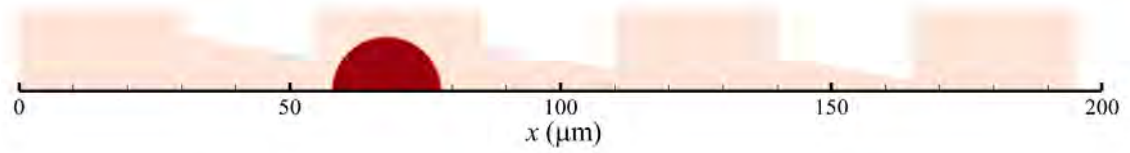


(c)

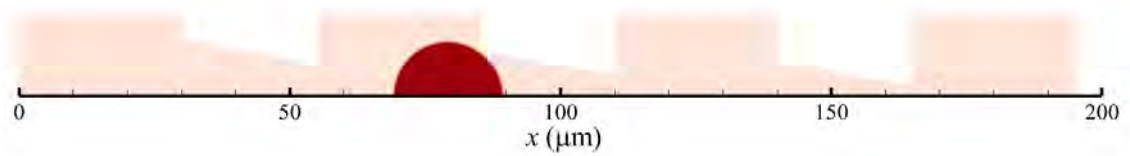


(d)

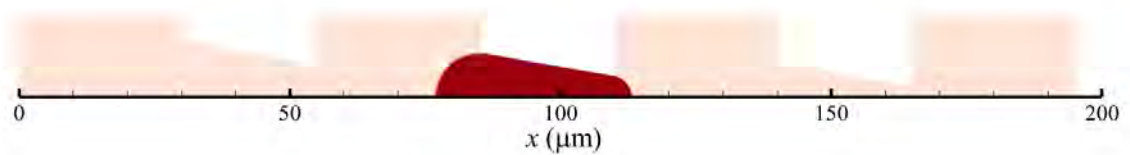
Figure 3.5: (a) flow rate and cell position history for the case: $P_{in} = 100$ Pa, $\sigma = 0.4$ mN/m and $D = 20$ μm , (b)-(h) cell volume fraction showing cell position and deformation at different times during passage through the filter. (cont.)



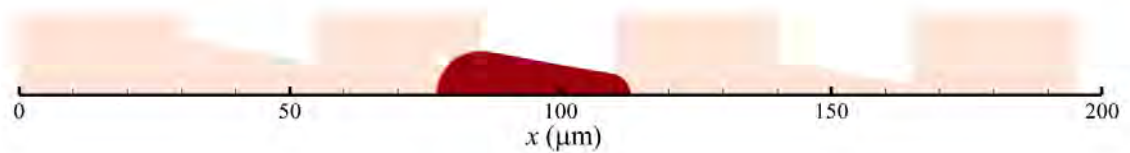
(e)



(f)

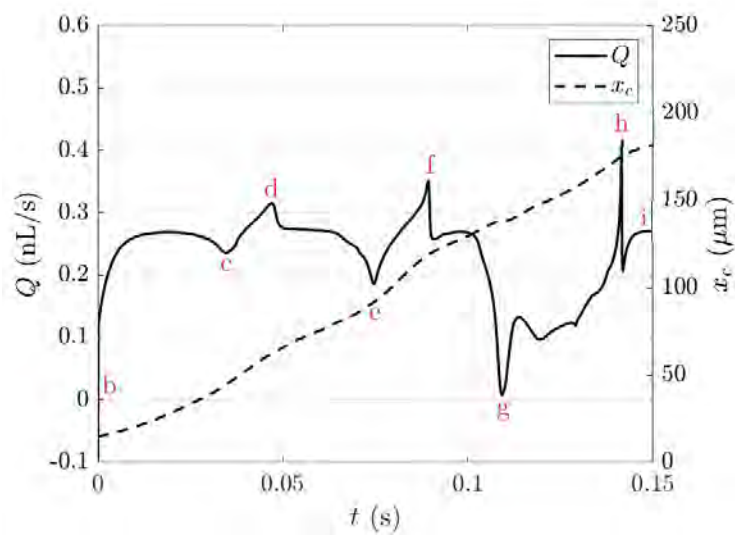


(g)

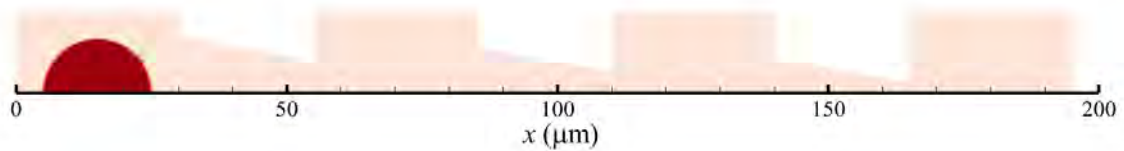


(h)

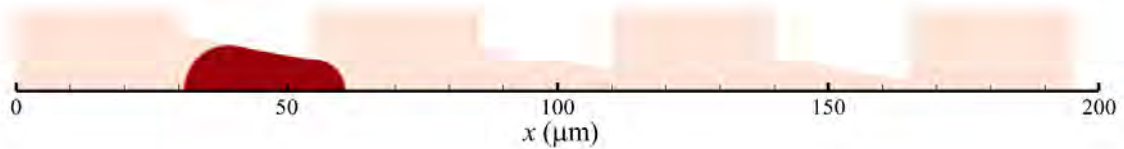
Figure 3.5: (a) flow rate and cell position history for the case: $P_{in} = 100$ Pa, $\sigma = 0.4$ mN/m and $D = 20$ μm , (b)-(h) cell volume fraction showing cell position and deformation at different times during passage through the filter.



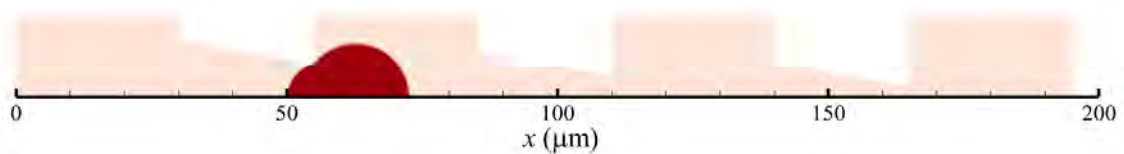
(a)



(b)

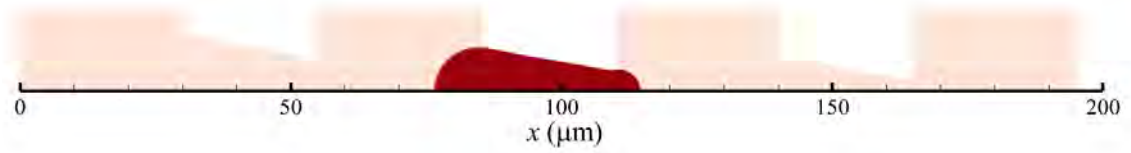


(c)

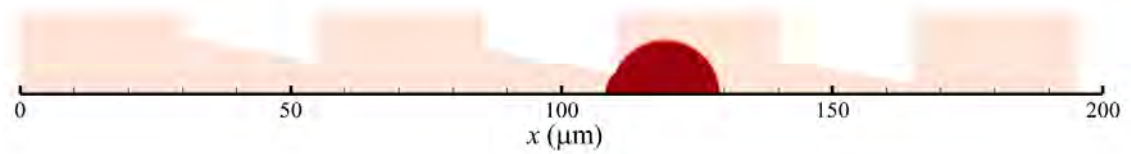


(d)

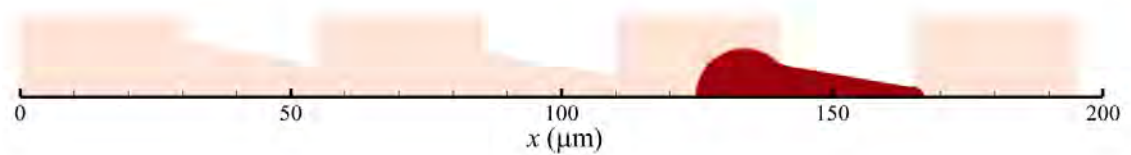
Figure 3.6: (a) flow rate and cell position history for the case: $P_{in} = 300$ Pa, $\sigma = 0.4$ mN/m and $D = 20$ μm , (b)-(h) cell volume fraction showing cell position and deformation at different times during passage through the filter. (cont.)



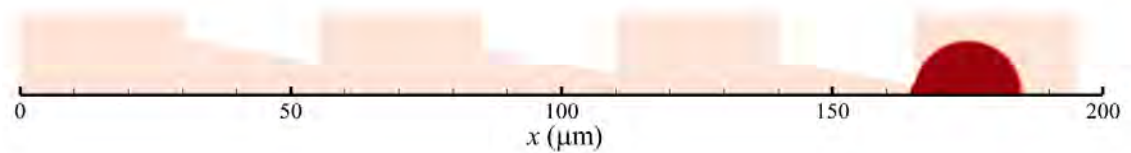
(e)



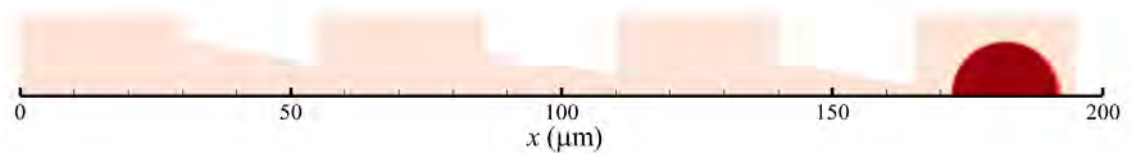
(f)



(g)

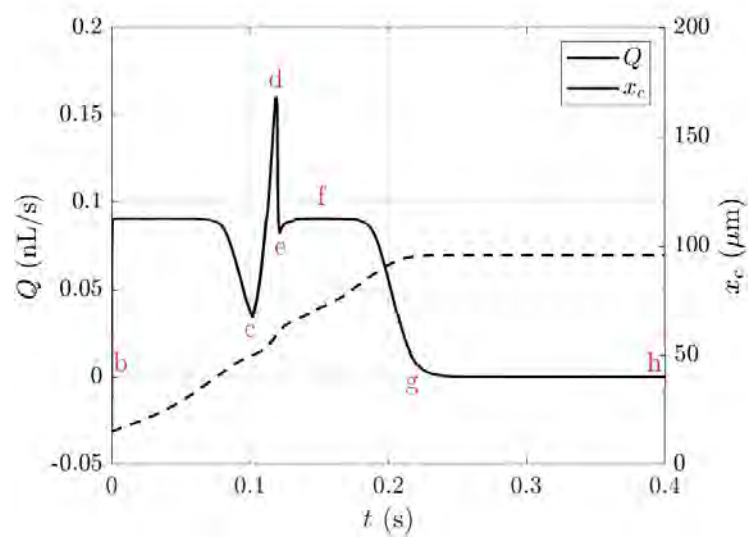


(h)

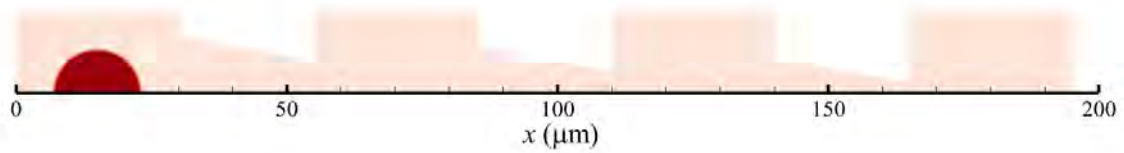


(i)

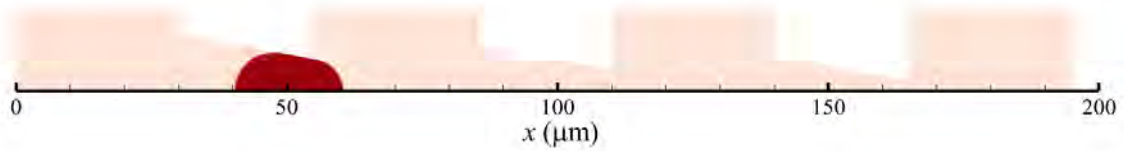
Figure 3.6: (a) flow rate and cell position history for the case: $P_{in} = 300$ Pa, $\sigma = 0.4$ mN/m and $D = 20$ μm , (b)-(h) cell volume fraction showing cell position and deformation at different times during passage through the filter.



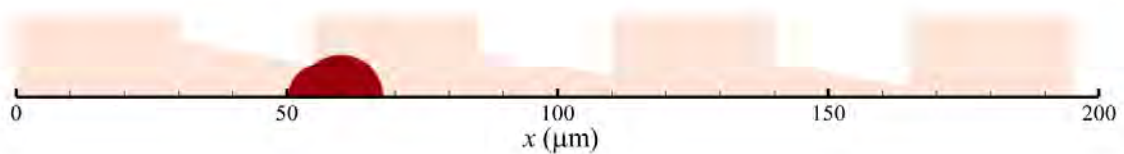
(a)



(b)



(c)



(d)

Figure 3.7: (a) flow rate and cell position history for the case: $P_{in} = 100$ Pa, $\sigma = 1.1$ mN/m and $D = 16$ μm , (b)-(h) cell volume fraction showing cell position and deformation at different times during passage through the filter. (cont.)

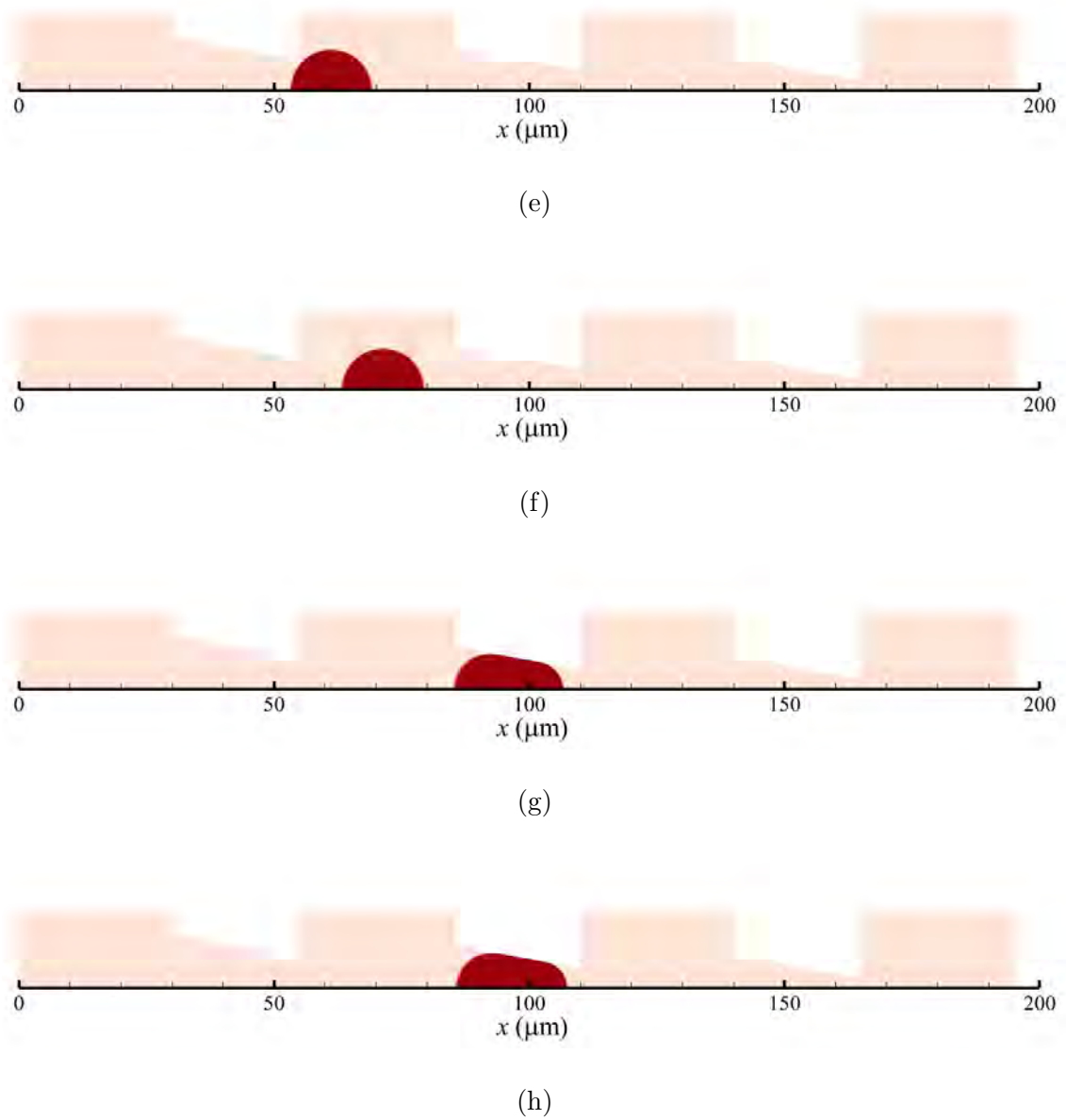
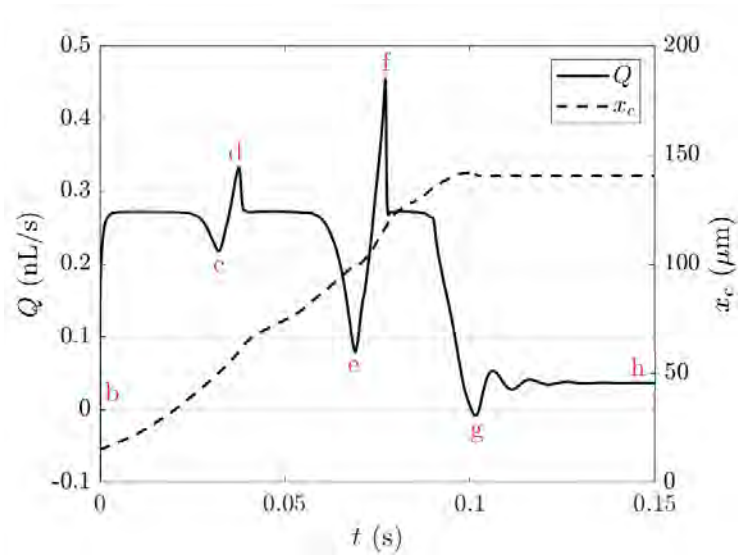
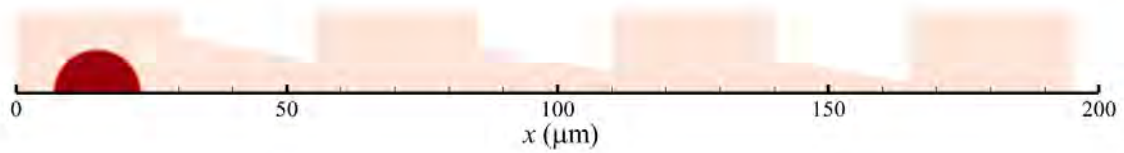


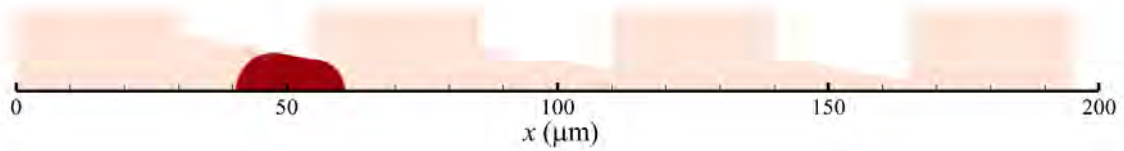
Figure 3.7: (a) flow rate and cell position history for the case: $P_{in} = 100$ Pa, $\sigma = 1.1$ mN/m and $D = 16$ μm , (b)-(h) cell volume fraction showing cell position and deformation at different times during passage through the filter.



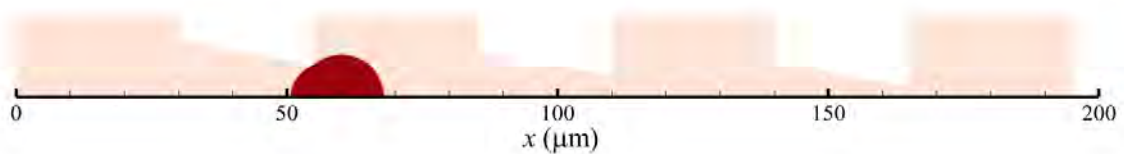
(a)



(b)



(c)



(d)

Figure 3.8: (a) flow rate and cell position history for the case: $P_{in} = 300$ Pa, $\sigma = 1.1$ mN/m and $D = 16$ μm , (b)-(h) cell volume fraction showing cell position and deformation at different times during passage through the filter. (cont.)

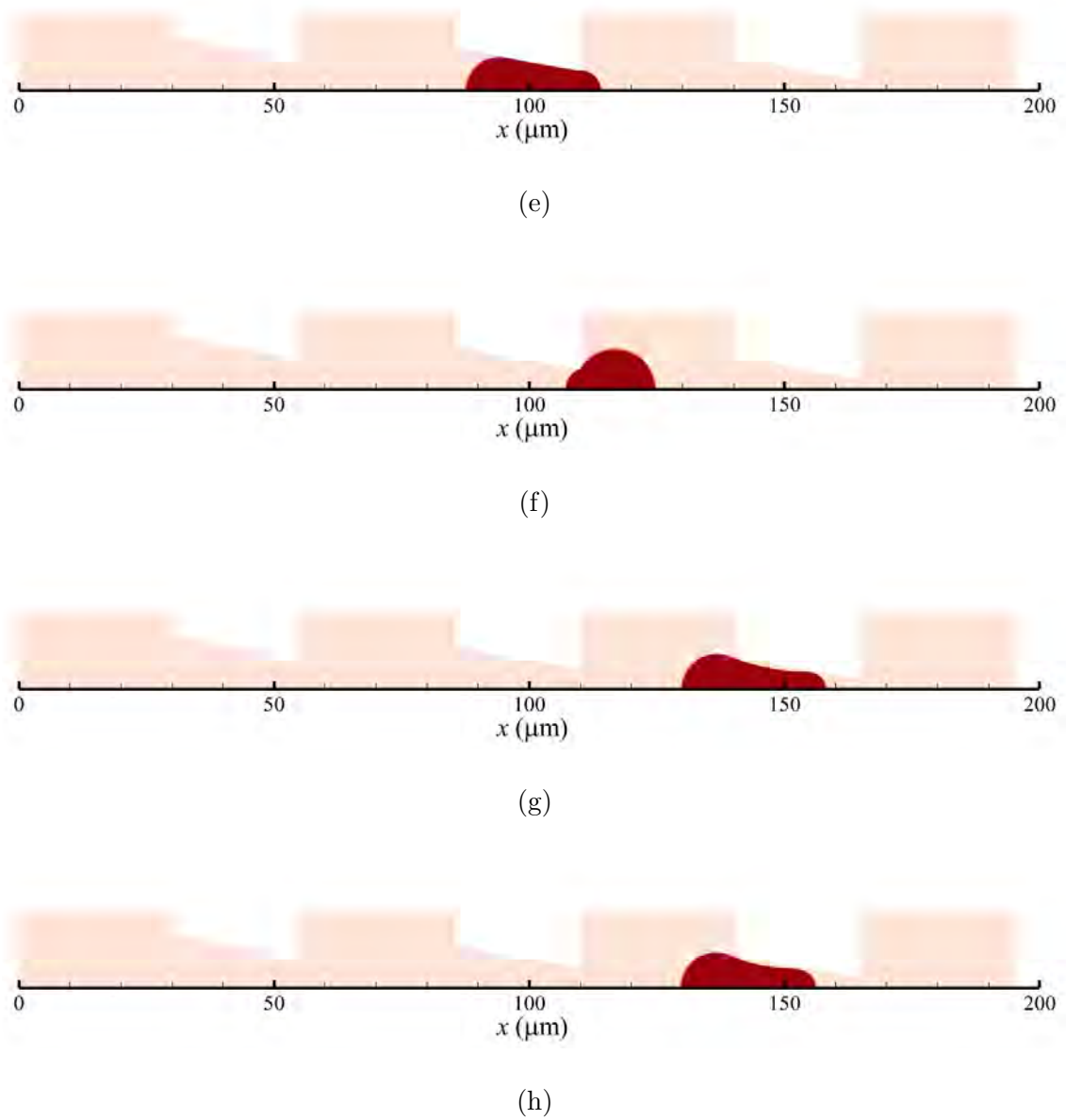
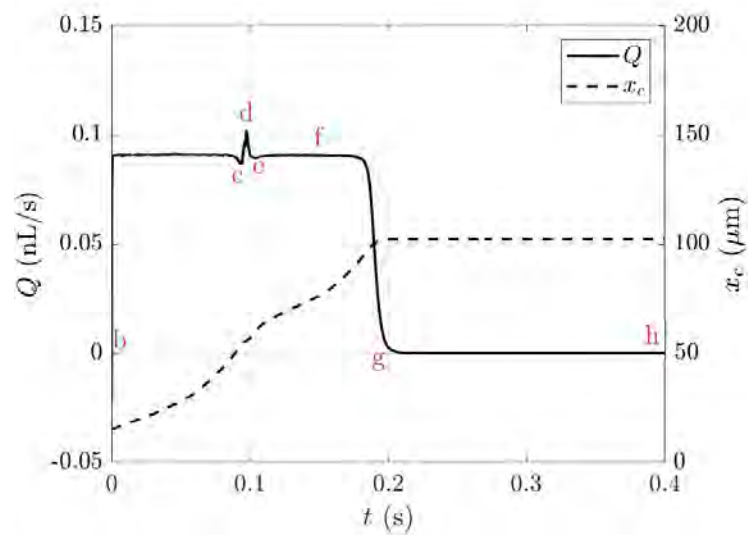
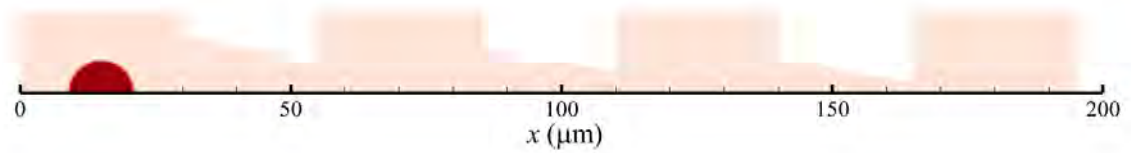


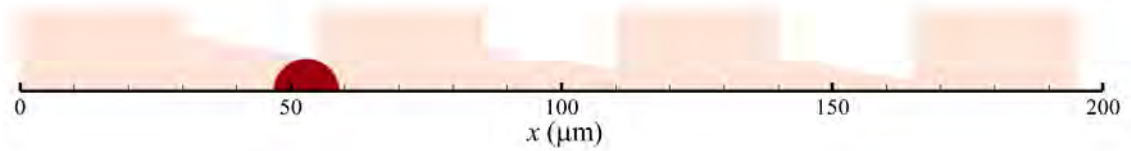
Figure 3.8: (a) flow rate and cell position history for the case: $P_{in} = 300$ Pa, $\sigma = 1.1$ mN/m and $D = 16$ μm , (b)-(h) cell volume fraction showing cell position and deformation at different times during passage through the filter.



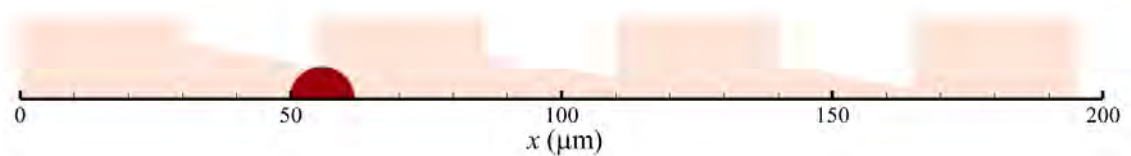
(a)



(b)



(c)



(d)

Figure 3.9: (a) flow rate and cell position history for the case: $P_{in} = 100$ Pa, $\sigma = 2$ mN/m and $D = 12$ μm , (b)-(h) cell volume fraction showing cell position and deformation at different times during passage through the filter. (cont.)

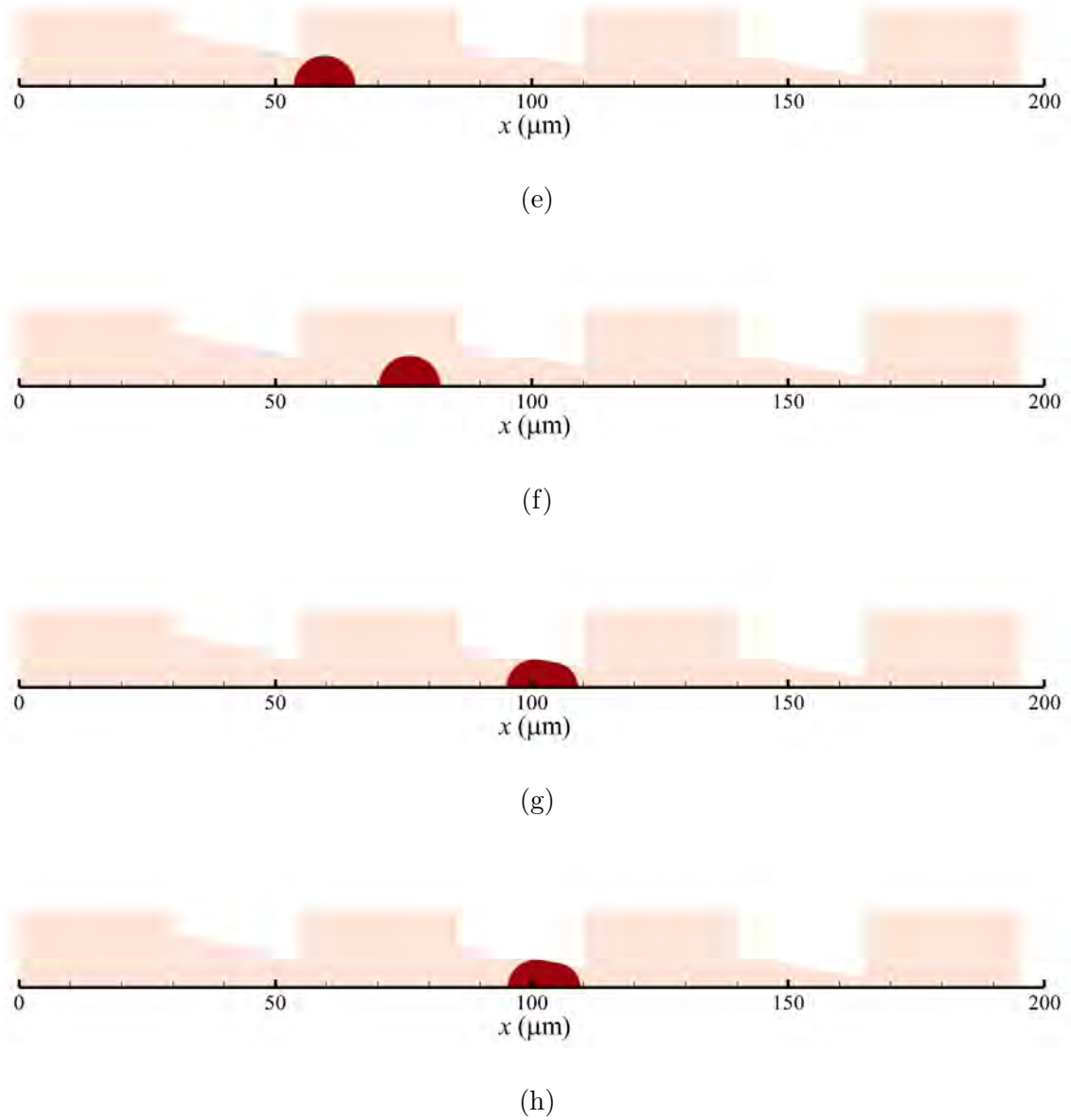
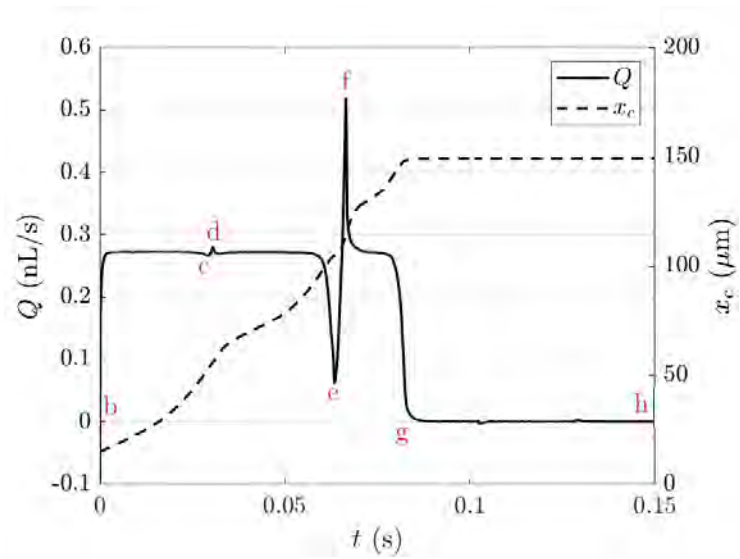
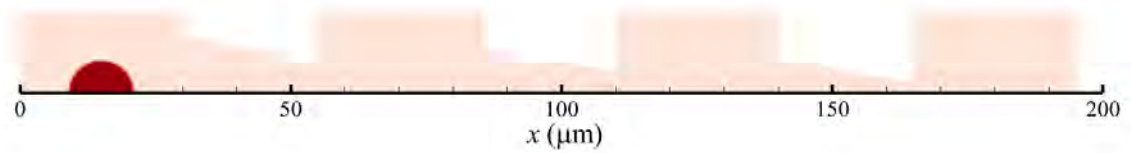


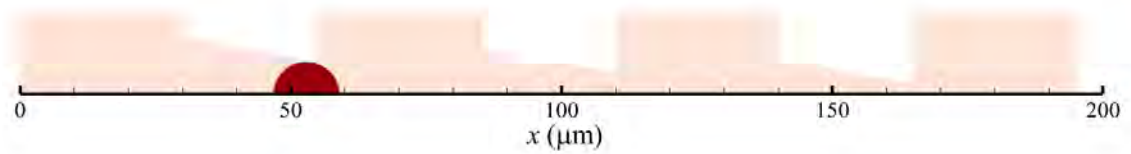
Figure 3.9: (a) flow rate and cell position history for the case: $P_{in} = 100$ Pa, $\sigma = 2$ mN/m and $D = 12$ μm , (b)-(h) cell volume fraction showing cell position and deformation at different times during passage through the filter.



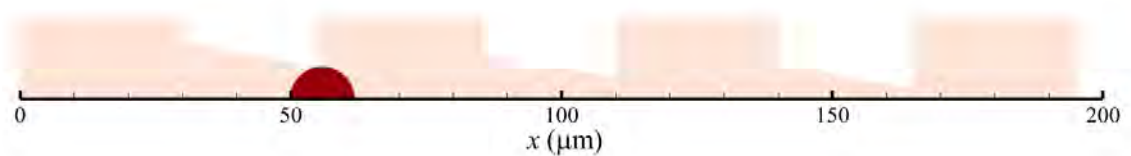
(a)



(b)



(c)



(d)

Figure 3.10: (a) flow rate and cell position history for the case: $P_{in} = 300$ Pa, $\sigma = 2$ mN/m and $D = 12$ μm , (b)-(h) cell volume fraction showing cell position and deformation at different times during passage through the filter. (cont.)

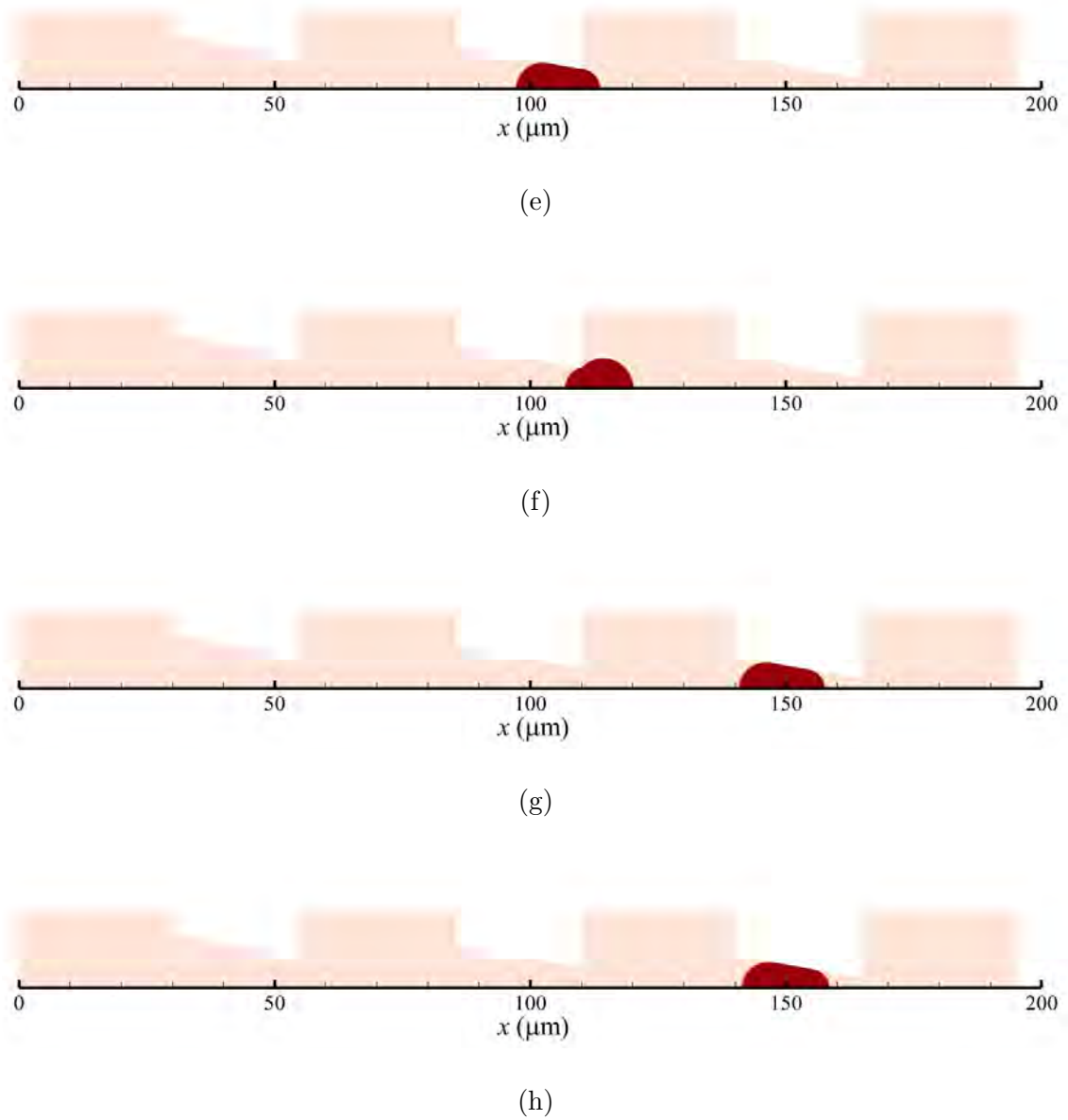
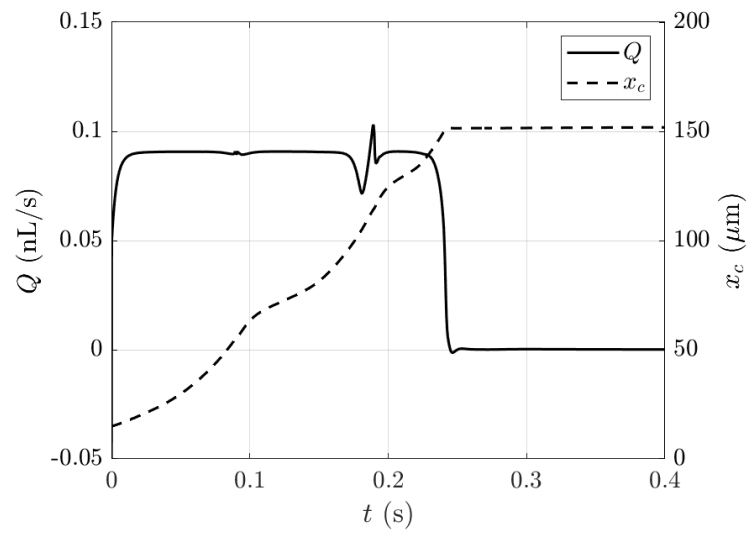
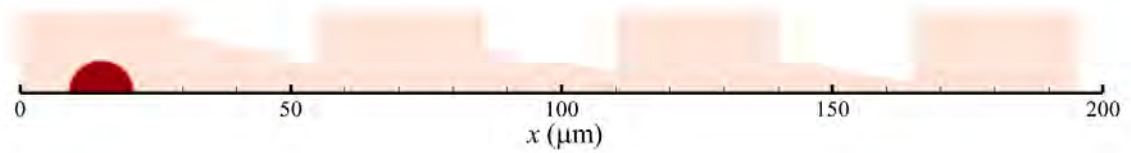


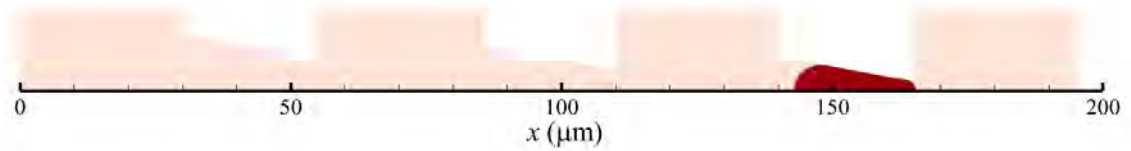
Figure 3.10: (a) flow rate and cell position history for the case: $P_{in} = 300$ Pa, $\sigma = 2$ mN/m and $D = 12$ μm , (b)-(h) cell volume fraction showing cell position and deformation at different times during passage through the filter.



(a)

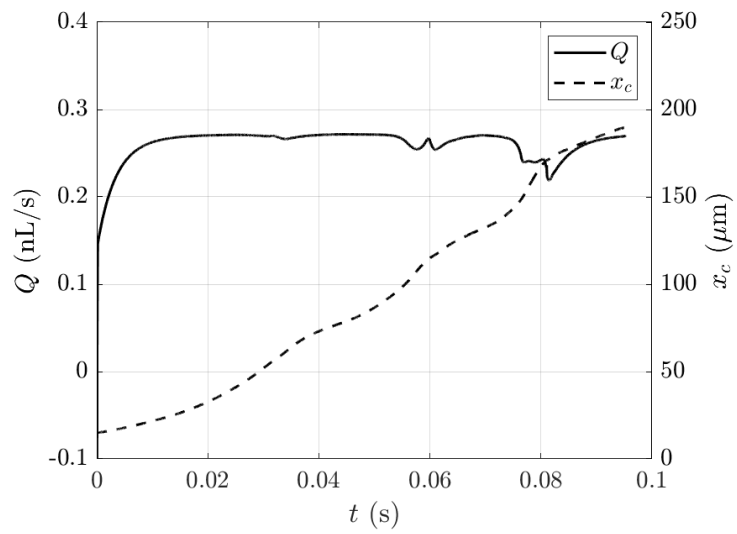


(b)

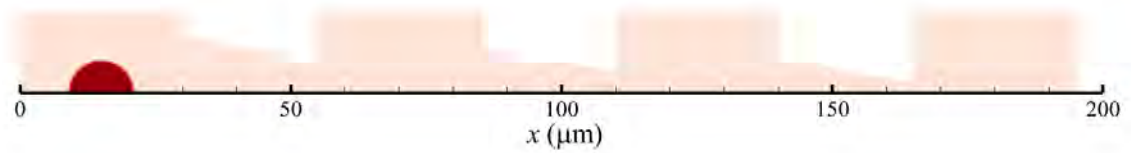


(c)

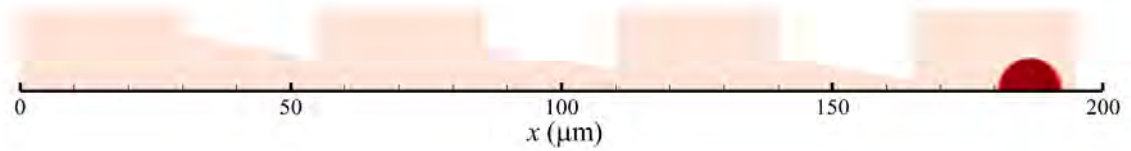
Figure 3.11: (a) flow rate and cell position history for the case: $P_{in} = 100$ Pa, $\sigma = 0.2$ mN/m and $D = 12$ μm , (b)-(c) cell volume fraction showing cell position and deformation at the initial and final time.



(a)

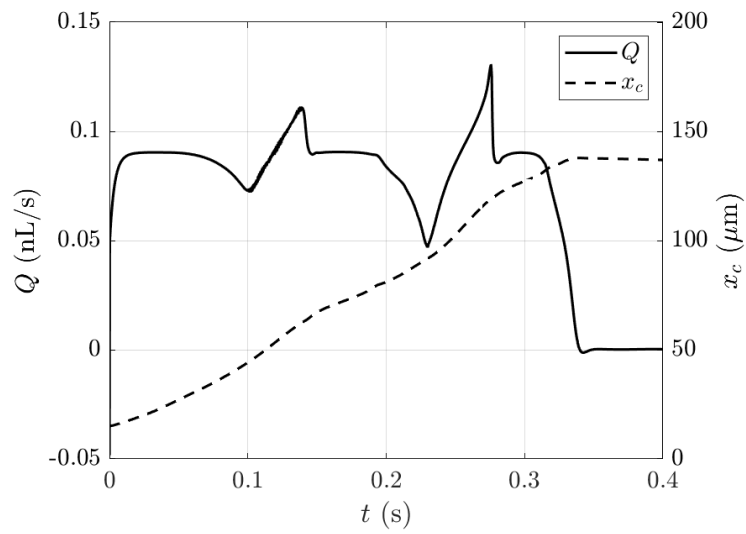


(b)

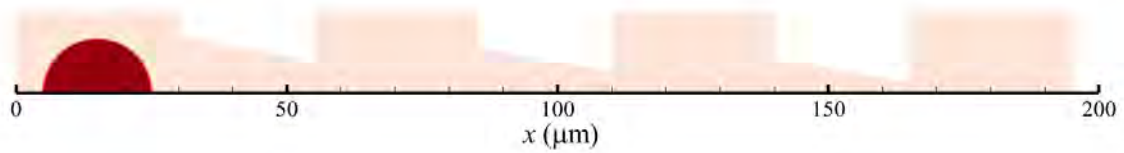


(c)

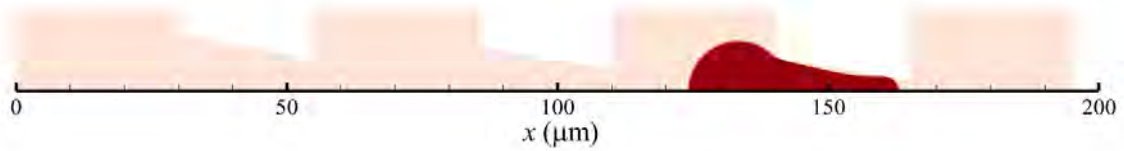
Figure 3.12: (a) flow rate and cell position history for the case: $P_{in} = 300$ Pa, $\sigma = 0.2$ mN/m and $D = 12$ μm , (b)-(c) cell volume fraction showing cell position and deformation at the initial and final time.



(a)

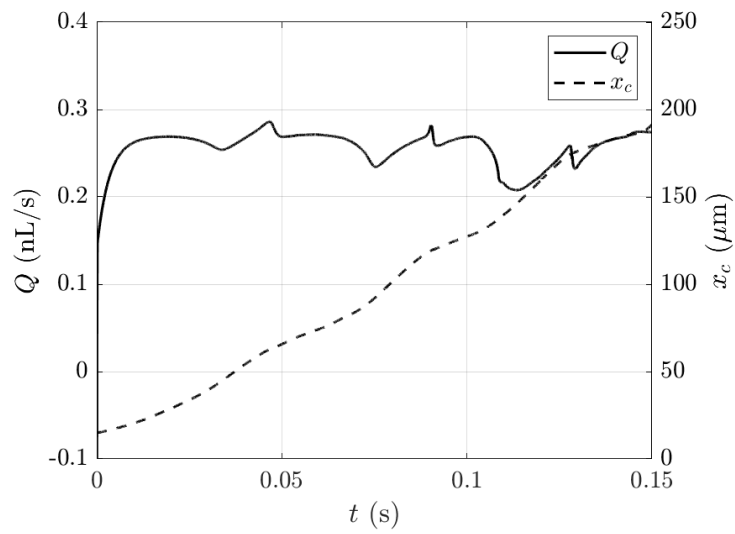


(b)

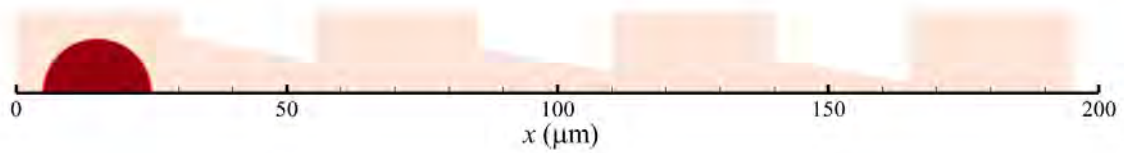


(c)

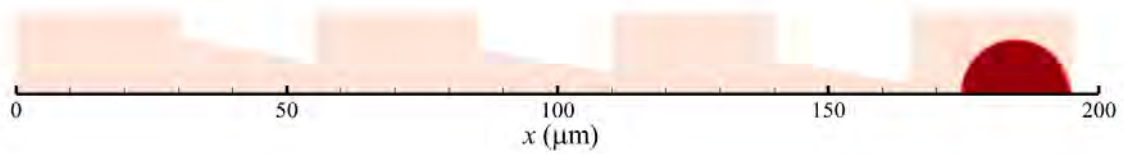
Figure 3.13: (a) flow rate and cell position history for the case: $P_{in} = 100$ Pa, $\sigma = 0.2$ mN/m and $D = 20$ μm , (b)-(c) cell volume fraction showing cell position and deformation at the initial and final time.



(a)

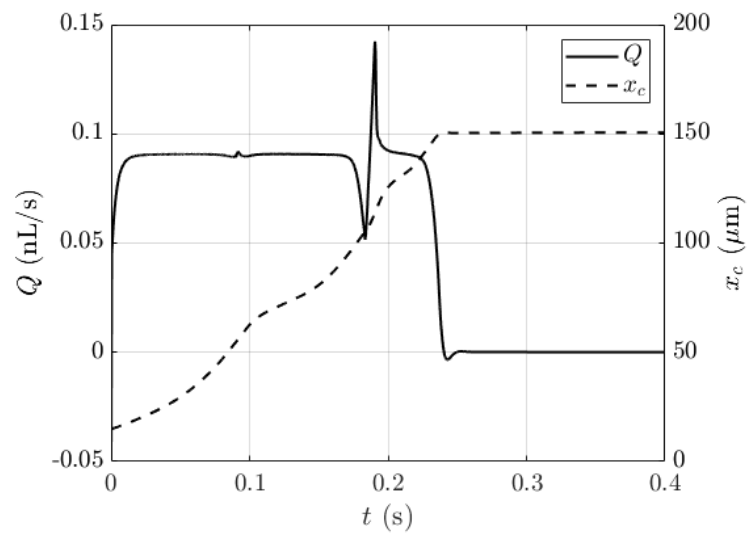


(b)

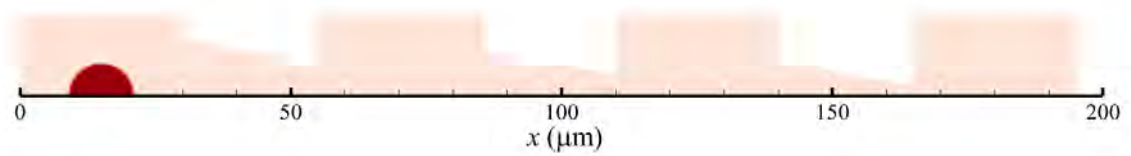


(c)

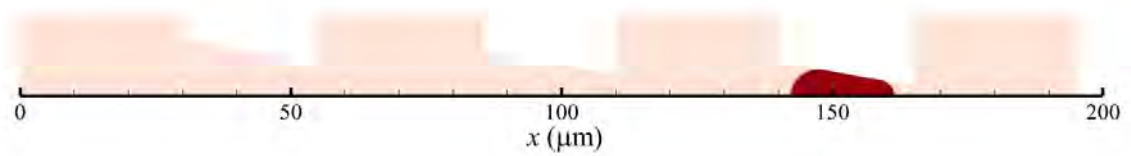
Figure 3.14: (a) flow rate and cell position history for the case: $P_{in} = 300$ Pa, $\sigma = 0.2$ mN/m and $D = 20$ μm , (b)-(c) cell volume fraction showing cell position and deformation at the initial and final time.



(a)

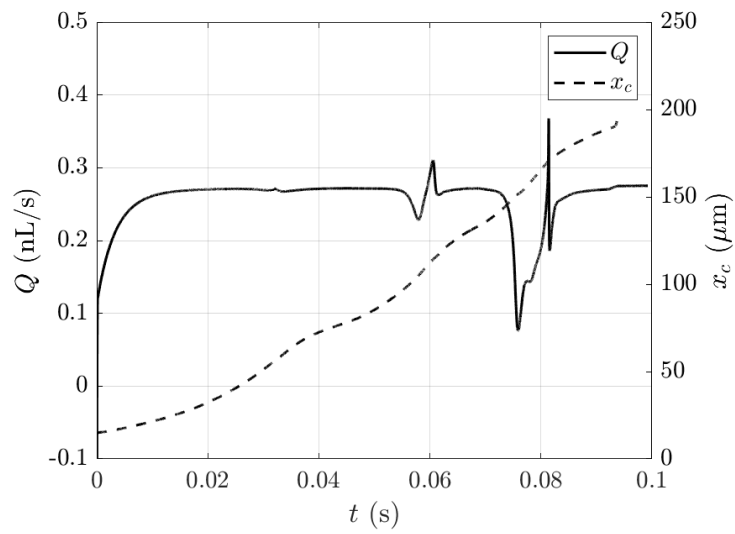


(b)

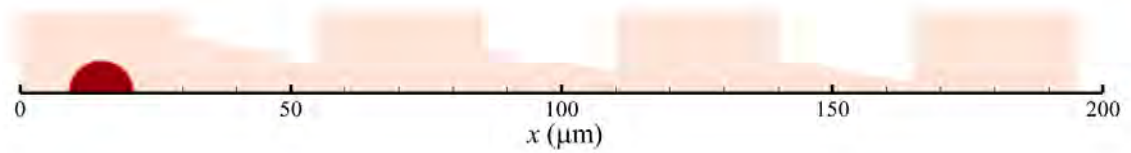


(c)

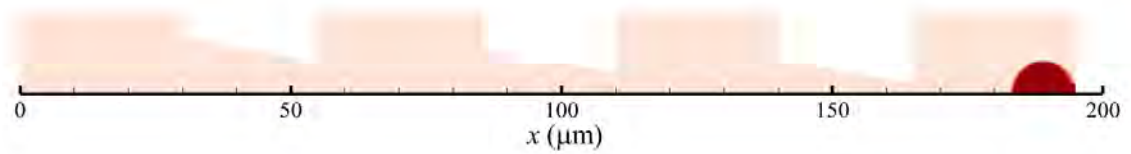
Figure 3.15: (a) flow rate and cell position history for the case: $P_{in} = 100$ Pa, $\sigma = 0.4$ mN/m and $D = 12$ μm , (b)-(c) cell volume fraction showing cell position and deformation at the initial and final time.



(a)

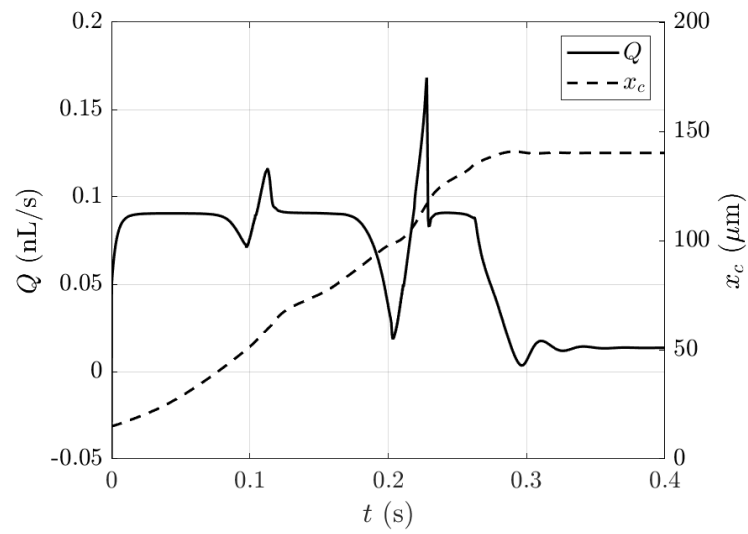


(b)

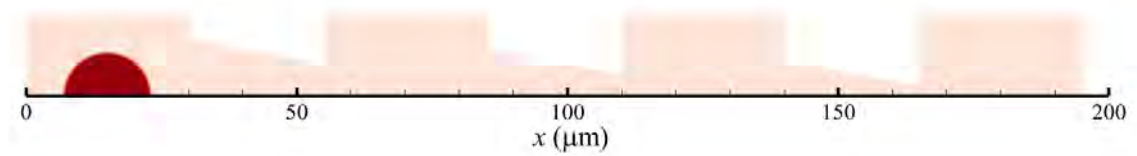


(c)

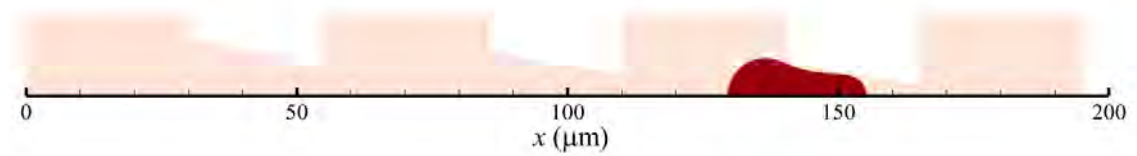
Figure 3.16: (a) flow rate and cell position history for the case: $P_{in} = 300$ Pa, $\sigma = 0.4$ mN/m and $D = 12$ μm , (b)-(c) cell volume fraction showing cell position and deformation at the initial and final time.



(a)

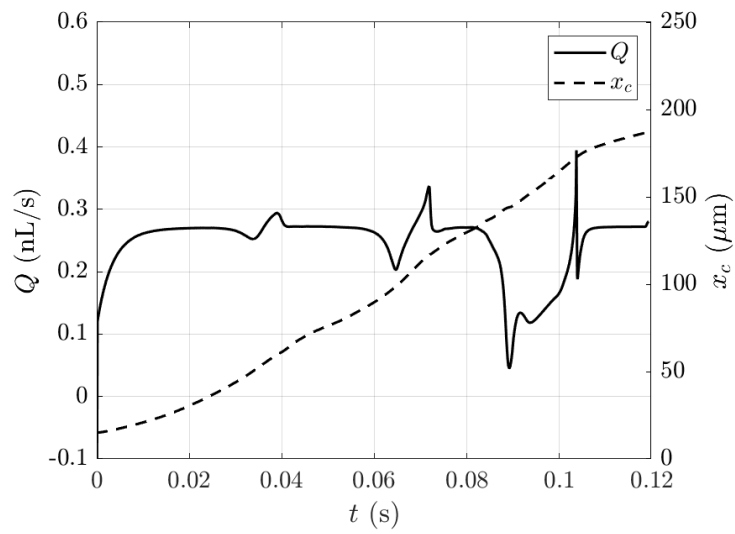


(b)

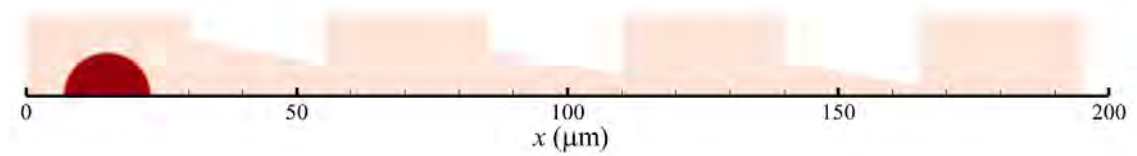


(c)

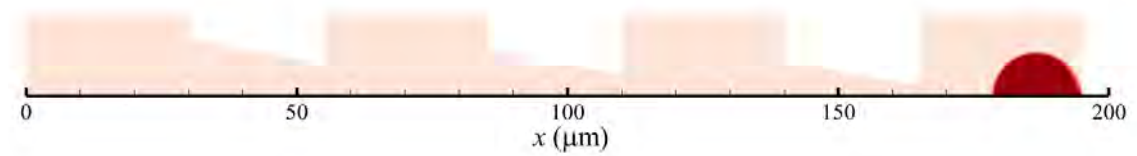
Figure 3.17: (a) flow rate and cell position history for the case: $P_{in} = 100$ Pa, $\sigma = 0.4$ mN/m and $D = 16$ μm , (b)-(c) cell volume fraction showing cell position and deformation at the initial and final time.



(a)

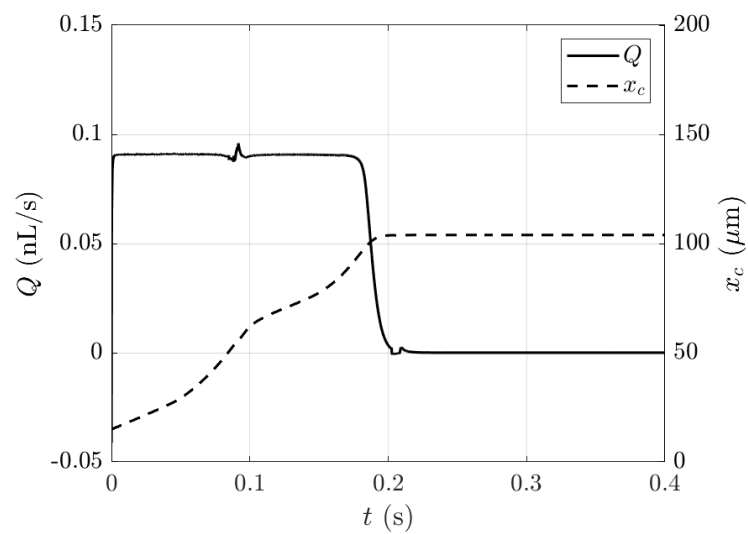


(b)

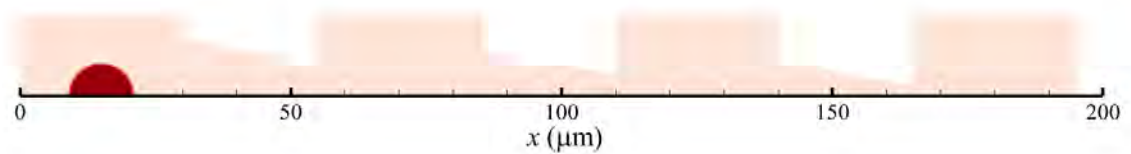


(c)

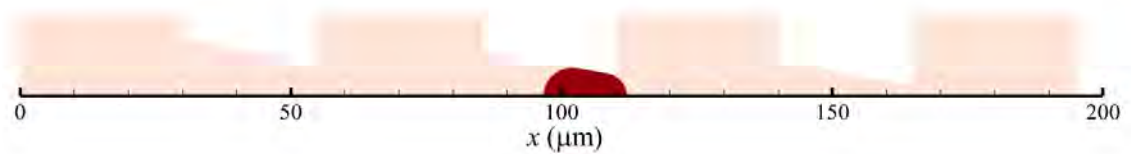
Figure 3.18: (a) flow rate and cell position history for the case: $P_{in} = 300$ Pa, $\sigma = 0.4$ mN/m and $D = 16$ μm , (b)-(c) cell volume fraction showing cell position and deformation at the initial and final time.



(a)

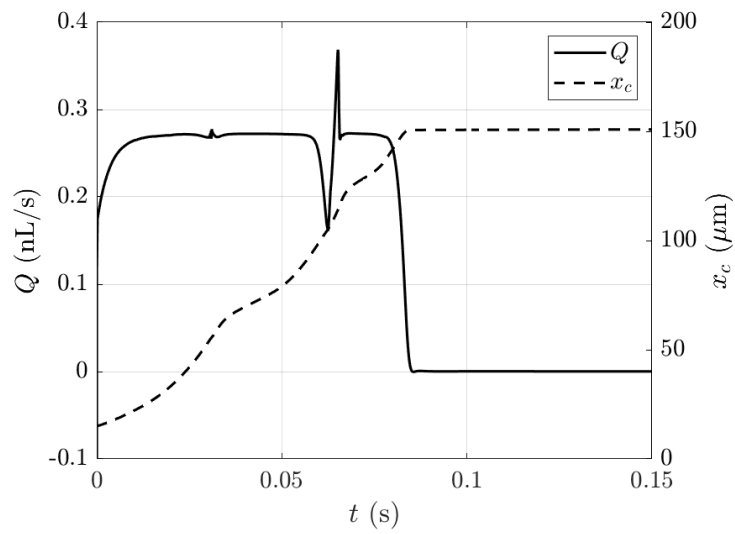


(b)

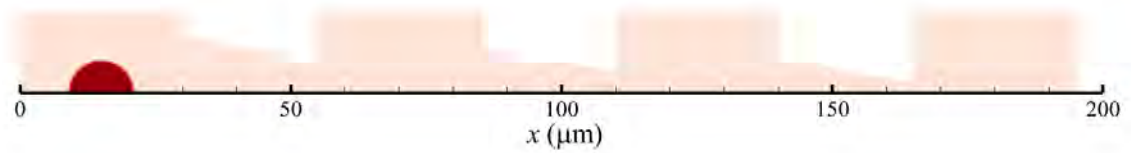


(c)

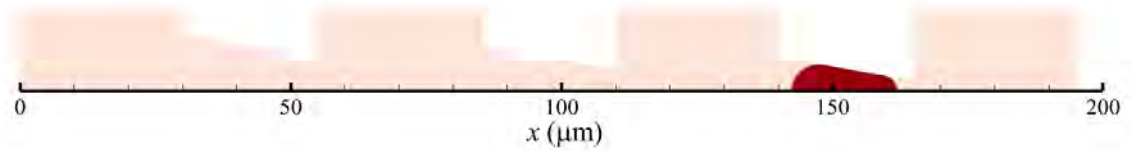
Figure 3.19: (a) flow rate and cell position history for the case: $P_{in} = 100$ Pa, $\sigma = 1.1$ mN/m and $D = 12$ μm , (b)-(c) cell volume fraction showing cell position and deformation at the initial and final time.



(a)

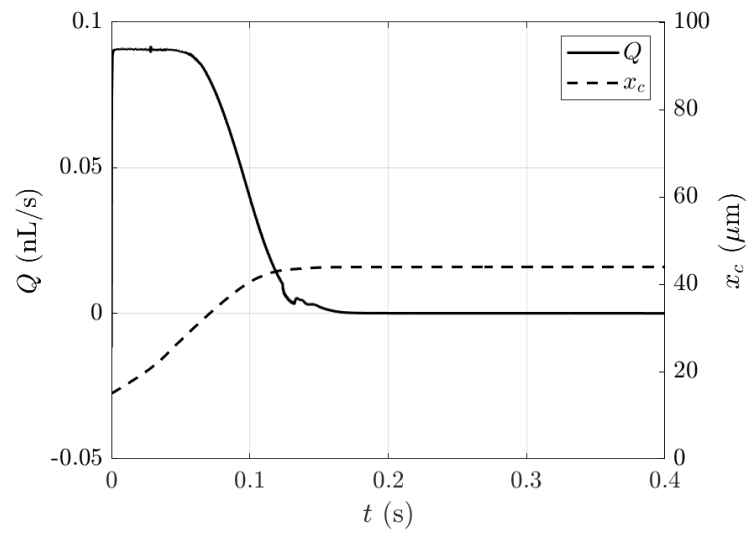


(b)

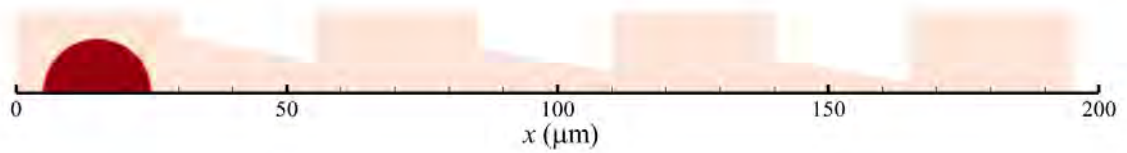


(c)

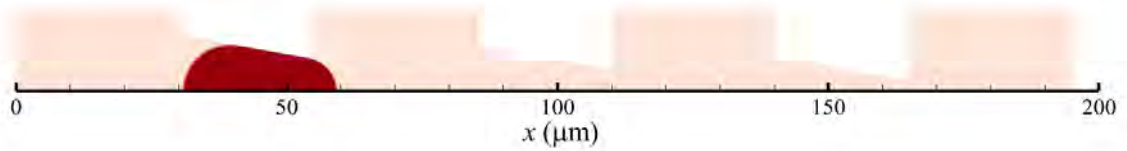
Figure 3.20: (a) flow rate and cell position history for the case: $P_{in} = 300$ Pa, $\sigma = 1.1$ mN/m and $D = 12$ μm , (b)-(c) cell volume fraction showing cell position and deformation at the initial and final time.



(a)

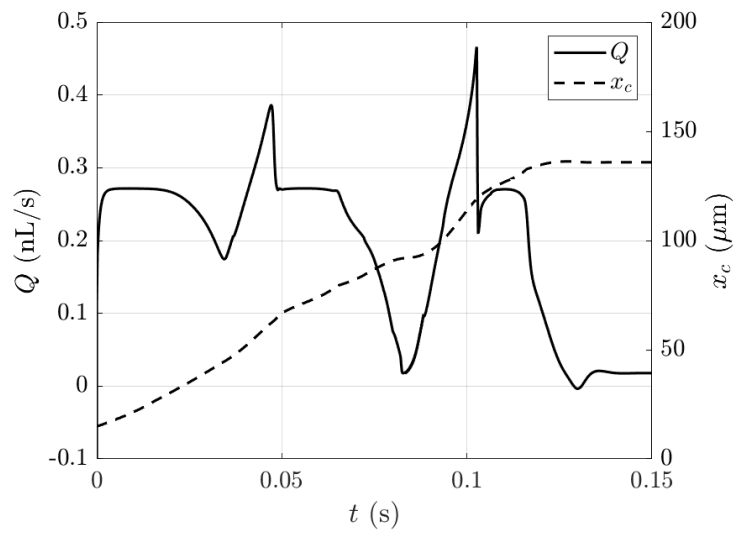


(b)

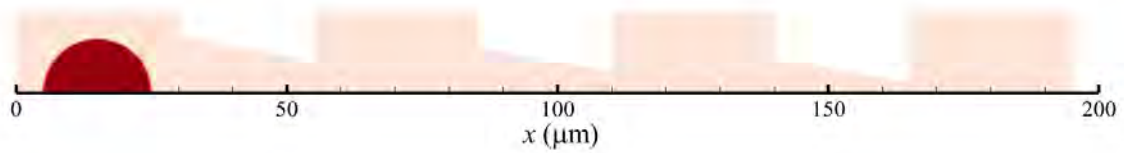


(c)

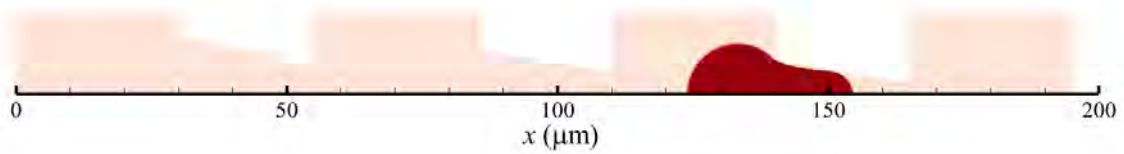
Figure 3.21: (a) flow rate and cell position history for the case: $P_{in} = 100$ Pa, $\sigma = 1.1$ mN/m and $D = 20$ μm , (b)-(c) cell volume fraction showing cell position and deformation at the initial and final time.



(a)

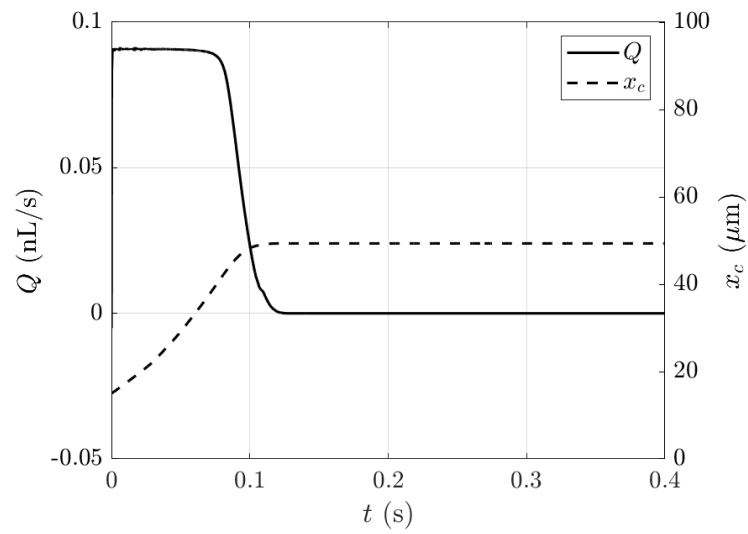


(b)

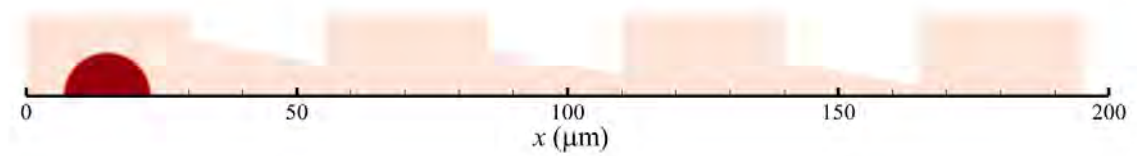


(c)

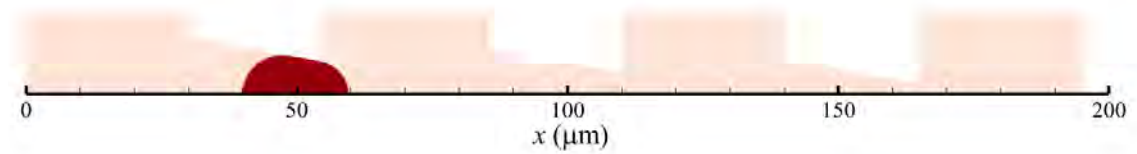
Figure 3.22: (a) flow rate and cell position history for the case: $P_{in} = 300$ Pa, $\sigma = 1.1$ mN/m and $D = 20$ μm , (b)-(c) cell volume fraction showing cell position and deformation at the initial and final time.



(a)

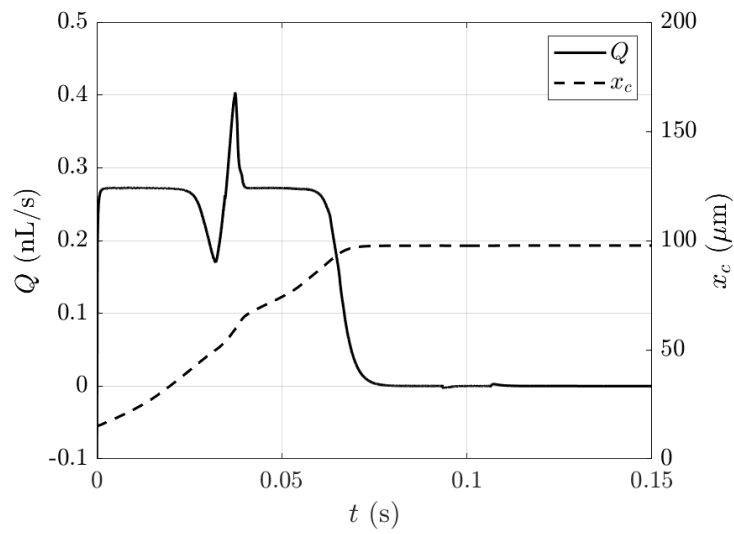


(b)

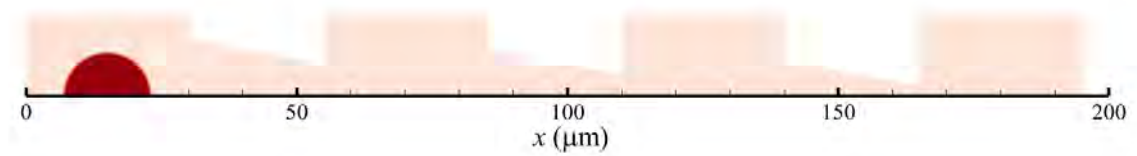


(c)

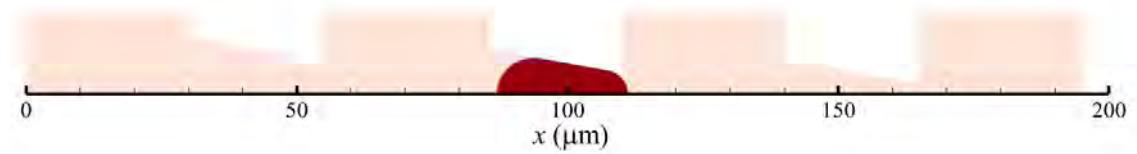
Figure 3.23: (a) flow rate and cell position history for the case: $P_{in} = 100$ Pa, $\sigma = 2$ mN/m and $D = 16$ μm , (b)-(c) cell volume fraction showing cell position and deformation at the initial and final time.



(a)

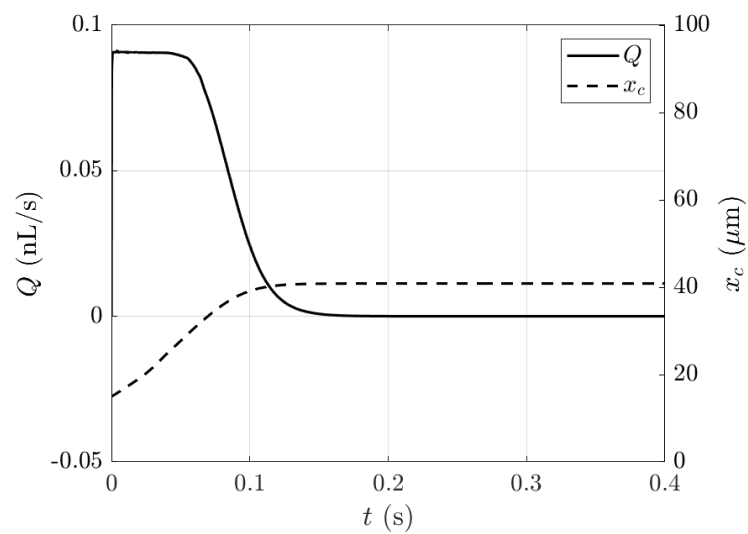


(b)

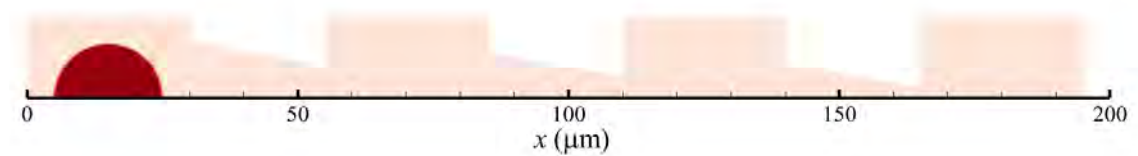


(c)

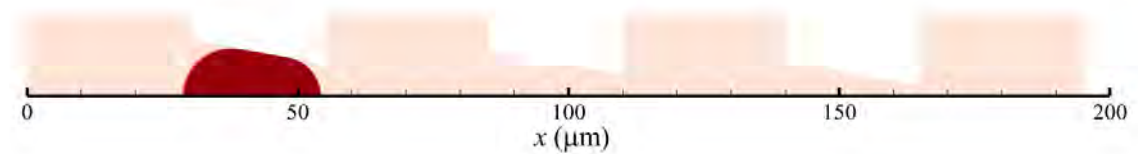
Figure 3.24: (a) flow rate and cell position history for the case: $P_{in} = 300$ Pa, $\sigma = 2$ mN/m and $D = 16$ μm , (b)-(c) cell volume fraction showing cell position and deformation at the initial and final time.



(a)

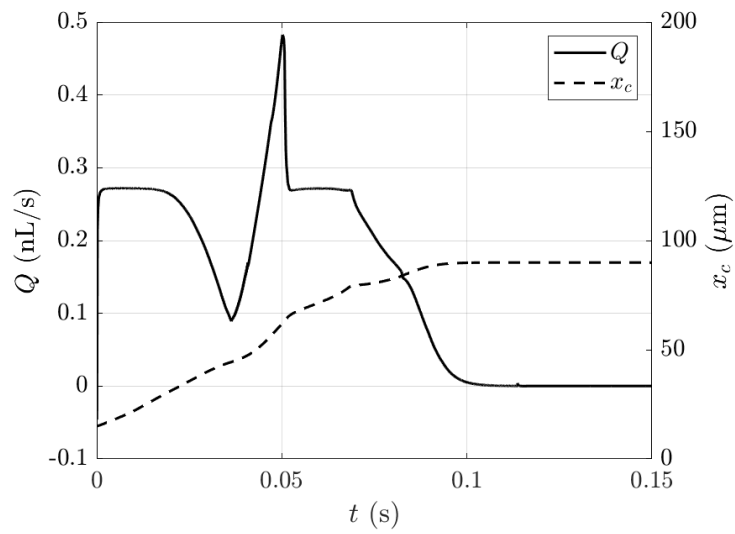


(b)

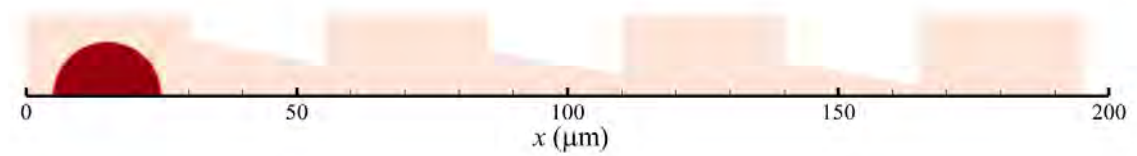


(c)

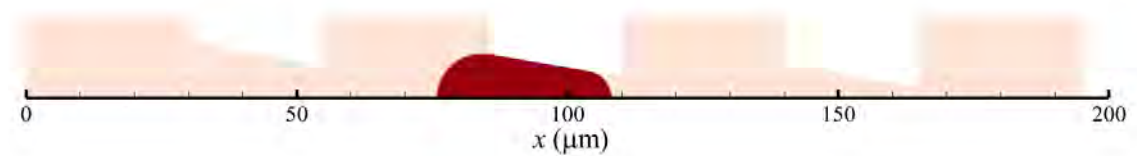
Figure 3.25: (a) flow rate and cell position history for the case: $P_{in} = 100$ Pa, $\sigma = 2$ mN/m and $D = 20$ μm , (b)-(c) cell volume fraction showing cell position and deformation at the initial and final time.



(a)



(b)



(c)

Figure 3.26: (a) flow rate and cell position history for the case: $P_{in} = 300$ Pa, $\sigma = 2$ mN/m and $D = 20$ μm , (b)-(c) cell volume fraction showing cell position and deformation at the initial and final time.

3.3 Quantification of cell deformation

To quantify cell deformation through the filters, the axial deformability index, ϵ is defined as

$$\epsilon = \frac{l_d}{D}, \quad (3.2)$$

where l_d is the axial length of the cell under deformation and D is the cell diameter (Figure 3.27). ϵ was calculated for the cases shown in Figures 3.3 to 3.10. Cell entry and exit from the filter funnels and the intermediate points were considered for calculating ϵ .

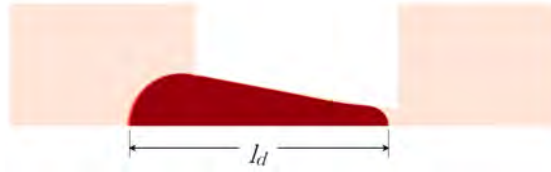


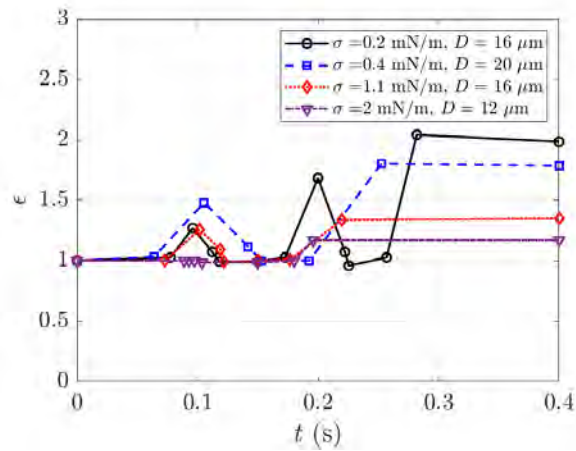
Figure 3.27: Deformed length, l_d for quantifying cell deformation.

The results are summarized in Figure 3.28 which shows ϵ separately for the 100 Pa and the 300 Pa cases. ϵ is 1 in the undeformed state. Cell deformation primarily depends on the pore radius, r_f of the filter funnel that a cell is passing through. The filter with the lowest r_f will produce the largest deformation. As a result, ϵ increases as a cell passes through a funnel. After that, the cell recovers its shape, and ϵ falls back to 1. Any residual value of ϵ greater than 1 at the end of the simulation indicates cell trapping. And the higher values of ϵ indicate the cell being trapped in a filter with a smaller r_f . Trapped cells are not always in the maximum deformed state. This is because, depending upon the cell property and the applied pressure, the front of the trapped cell can be at the entrance of the filter funnel to the exit. The more a cell enters into a funnel up to the exit, the more deformed it gets. The final deformation and ϵ will, thus, depend on the final position within a funnel. If a cell passes through all the funnels without getting trapped, it recovers its shape, and ϵ goes back to 1.

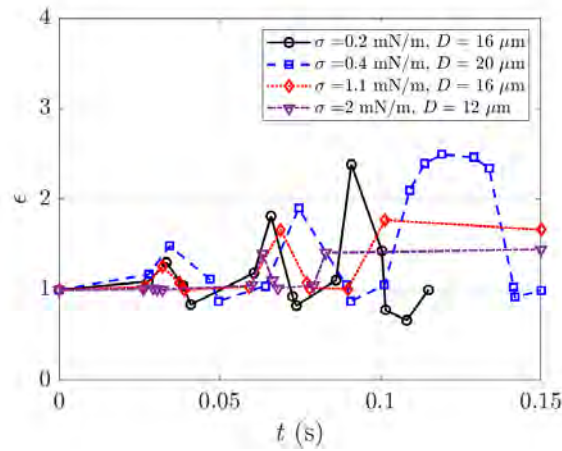
From Figure 3.28 (a), the $\sigma = 0.2$ case shows the most amount of deformation ($\epsilon \approx 2$). This is because this cell gets trapped in filter 3, while the other cells

get trapped in filter 2. Even amongst these two cases, a different amount of final deformation is seen according to their final trapped position. The stiffer the cell, the lower the final value of ϵ , indicating that stiffer cells get trapped early in a particular funnel. For the 100 Pa case, cells with the same diameter, $D = 16\mu\text{m}$, show similar amount of deformation in filter 1 ($\epsilon \approx 1.25$). But the largest cell, $D = 20\mu\text{m}$, shows more deformation in the same filter ($\epsilon \approx 1.5$), indicating the larger cells have to go through more deformation as they pass a filter funnel.

Under 300 Pa pressure, as shown in Figure 3.28 (b), filter 1 produces the same amount of deformation for the two cases having the same value of $D = 16\mu\text{m}$. But for filter 2, which both cells passed through, the softer cell $\sigma = 0.2\text{ mN/m}$ shows more deformation ($\epsilon \approx 1.8$). The largest cell, $D = 20\mu\text{m}$, shows more deformation in this case too. Interestingly, a few cases show ϵ falling below 1. These are the instants when there is cell recoil after passing through a funnel. The softest cell $\sigma = 0.2\text{ mN/m}$ has more deformation due to recoil than the other cases. The deformation is also more pronounced compared to the 100 Pa case. For the same cell physical properties, the maximum value of ϵ for the 300 Pa case is larger due to the cell passing event, which deforms a cell more than a case where it is simply trapped in a funnel. ϵ exceeds 2 for the cases where the cell traverses through filter 3, indicating the highly deformed nature of the cell during passage through the filter funnels. The softest cells ($\sigma = 0.2$ and 0.4 mN/m) both pass through filter 3 and ϵ reaches about 2.5. After full passage through the filter funnel, ϵ recovers to 1.



(a)



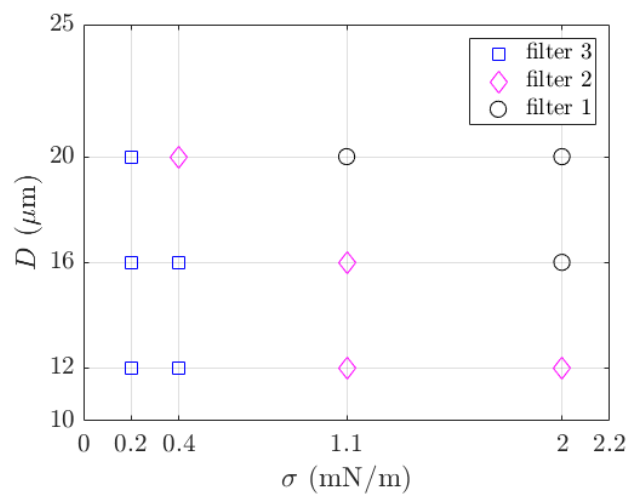
(b)

Figure 3.28: (a) Axial deformation, ϵ history for different cases: (a) $P_{in} = 100$ Pa and (b) $P_{in} = 300$ Pa.

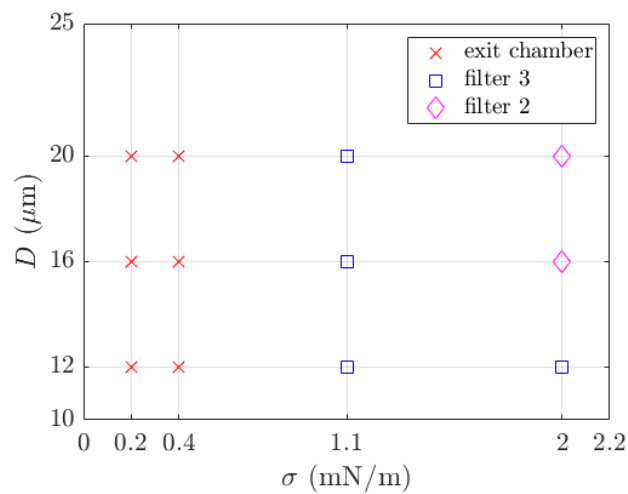
3.4 Cell sorting and trapping in filter array

The summary of the results of all the filter array simulation cases under pressure-driven flow is shown in Figure 3.29. The results are shown separately for 100 and 300 Pa inlet pressure. Every point in the graphs indicates a cell with distinct physical properties. A separate symbol is used to identify in which filter funnel the cell has been trapped into or whether the cell passes all the filter funnels into the exit chamber. For the 100 Pa case, none of the cells pass through to the exit chamber. This means under 100 Pa driving pressure, all the cells under consideration will be trapped. But how the cells are sorted in the filter funnels is strongly dependent

upon cell cortical tension, σ . Stiffer cells get trapped in funnels with a higher value of r_f . While the softer cells can make it further forward towards the funnels with smaller r_f . There is also variation due to cell diameter, D where a softer but larger cell ($\sigma = 0.4$ and 1.1 mN/m, $D = 20$ μm .) gets trapped. On the other hand, the 300 Pa cases also show sorting dependent on σ and D . But there is a clear distinction with the previous case. The difference of 200 Pa between the two groups of pressure is enough to make every cell jump to at least the next filter or the exit chamber. Some of the cells can even jump 2 filter funnels.



(a)



(b)

Figure 3.29: Trapping and sorting of CTCs under (a) 100 Pa and (b) 300 Pa driving pressure.

The summary indicates that the cells can pass through to the exit chamber if the applied pressure is sufficient. If not, then cells get trapped in a filter funnel. The cells are sorted in the funnels according to their physical properties under consideration, cortical tension, σ and cell size, D . The sorting pattern depends upon the applied pressure. Different applied pressure results in a different collection of cells in the filter funnels. This result provides proof that in addition to trapping, circulating tumor cells can also be sorted in microfluidic filter arrays. And for a given geometry of cells, the sorting range can be adjusted by changing the value of the applied pressure. It is to be noted that higher resolution in sorted cell property can be achieved in long filter arrays with gradual changes in the value of r_f .

In the experimental work by McFaul et al. [61], two different types of cells (mouse lymphoma cells (MLCs) and human peripheral blood mononuclear cells (PBMCs)) representing stiff and soft cells, were filtered through a microfluidic array device. The cells had some variation in their respective diameter and cortical tension values. The objective of the experiment was to separate the two populations of cells. This was achieved with a clear distinction between the average trapping funnel sizes of the cells. But there was spreading in the trapping funnel size due to variation in properties. This study considers variation in physical properties by a larger magnitude. Thus physical property-based trapping and sorting can easily be distinguished. They also studied the effect of driving pressure. Higher driving pressure resulted in the decrease of trapping funnel size, which is similar to the findings of this study that at higher driving pressure, cells move to smaller filter funnels.

Chapter 4

Establishment of Filter

Characteristics from Threshold

CTC Passing Pressure

4.1 Pressure signatures for CTC passing through a filter funnel

As discussed in Section 3.1.1, when a cancer cell passes through a filter funnel at a constant flow rate, the inlet total pressure first increases as the cell gets deformed in the filter. This increase in pressure is due to an increase in $P_{\text{cortical-tension}}$ described in equation 3.1. Thus, the threshold pressure required to ensure CTC passage through a filter funnel can be calculated from the equation 3.1 by subtracting P_{viscous} from the maximum value of total inlet pressure. As demonstrated in Section 3.2, if the applied inlet pressure is not sufficient, the cell comes to rest in the deformed state, unable to fully pass through the filter funnel. For this study, four different values of cell cortical tension, σ , three different values of cell diameter, D and filter funnels of three different pore radius, r_f are considered. This constitutes 36 cases. For all these cases, threshold passing pressure was determined through simulations at a constant inlet flow rate. The flow rate, Q was set to 0.27 nL/s.

Figure 4.1 shows the inlet total pressure signature for the case $r_f = 6 \mu\text{m}$, $\sigma = 0.2 \text{ mN/m}$ and $D = 16 \mu\text{m}$. Cell deformation is shown by cell volume fraction at different important instants. The pressure signature follows the trends shown in Figure 3.1, where two pressure peaks are observed. The first peak is generated when the cell front has passed the exit of the filter funnel with minimum curvature (Figure 4.1(d)). The second peak is generated when there is a recoil motion of the cell after coming out of the funnel. The second peak, however, is after the cell has already passed the filter funnel and thus has no significance in terms of the pressure required to pass the filter. The value of the second pressure peak can, however, be larger than the first, as shown in Figures 4.1(g). There is an oscillation in the pressure signature after the cell passes the filter funnel (Figures 4.1(h-i)). This happens because of the cell oscillation after the recoil motion. Three more cases have been shown in details, in Figures 4.2 to 4.4. These cases encompass all of the values of σ , D and r_f . Although the pressure signatures have the same general trend, the exact shape varies from case to case depending upon cell physical properties and filter pore radius r_f . The initial value of P_{viscous} is dependent upon filter pore radius, r_f . Filters with smaller openings create larger hydraulic resistances, which result in a larger pressure drop. The change in inlet total pressure, P_{in} due to cell deformation is dependent upon the parameters considered, namely σ , D and r_f .

Cell transit time through a funnel depends on r_f and D . Since the inlet flow rate was kept constant in all the cases, filter funnels with smaller r_f have smaller cross-sectional areas and thus produce higher velocities within the funnel. Higher velocity leads to a faster passing of the cell through the filter, as can be inferred from Figures 4.1 and 4.3. However, larger cells take longer to complete the passage as they have to traverse a longer distance from entry to complete exit from a filter funnel. This can be observed from Figures 4.2 and 4.4.

There is a formation of a thin lubrication layer when the cell passes through the filter funnel. Previous studies [72, 114] have shown that the film thickness is dependent upon the viscosity ratio of the two phases and the capillary number, Ca by the following relation:

$$\frac{e}{R} = F(\lambda, Ca) \cdot Ca^{2/3}, \quad (4.1)$$

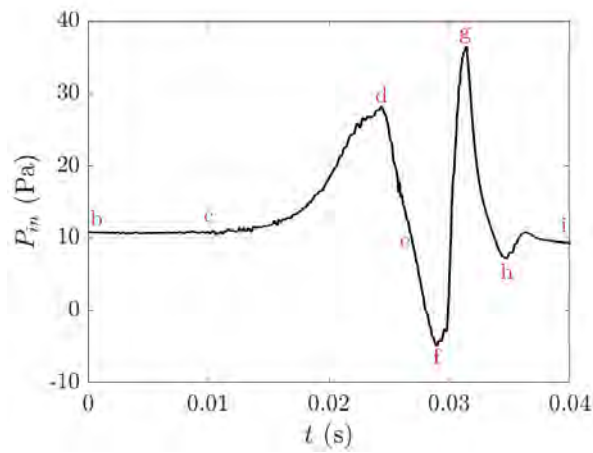
where e is the film thickness, R is the radius of the cylindrical channel considered in the studies, F is a coefficient determined by the viscosity ratio, λ . The viscosity ratio is one in all the cases considered in this study. The capillary number is defined by,

$$Ca = \frac{\mu U}{\sigma}, \quad (4.2)$$

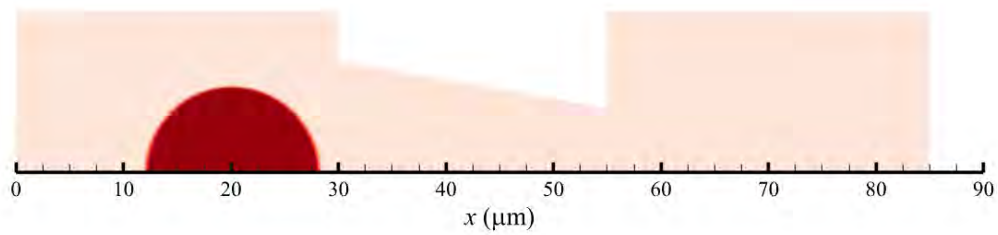
where μ is the cell viscosity and U is the local velocity of the cell in the filter funnel. μ was kept constant for all the cases. The inlet flow rate was also kept constant, which means funnels with smaller r_f have higher velocity U during cell passage. In addition, softer cells have a smaller value of σ . This means that cases, where σ and r_f are small are the cases where the film thickness is going to be higher. Figures 4.1(e) and 4.2(e) show formation of the lubrication film along the funnel wall at the exit. This two cases consider soft cells ($\sigma = 0.2$ and 0.4 mN/m) and for 4.2(a) smallest value of r_f . Figure 4.3 however, does not show any discernible formation of lubrication layer. This case has a higher value of σ and thus a small value of Ca . The next case is shown in Figure 4.4 however shows the formation of a thin lubrication layer. Although this case considers the cell with the highest stiffness ($\sigma = 2$ mN/m), pore radius r_f is the smallest ($r_f = 2$ μm). This results in higher velocity at the filter funnel exit leading to a high value of Ca , which leads to the formation of the thin layer.

The threshold pressure point in Figures 4.1- 4.4 (e) show variation in cell positions within the funnel. Similar results were found by Zhang et al. [72]. They found that a change in viscosity ratio, λ , not only brings a change in the thickness in the lubrication layer but also a change in the cell position at the maximum pressure.

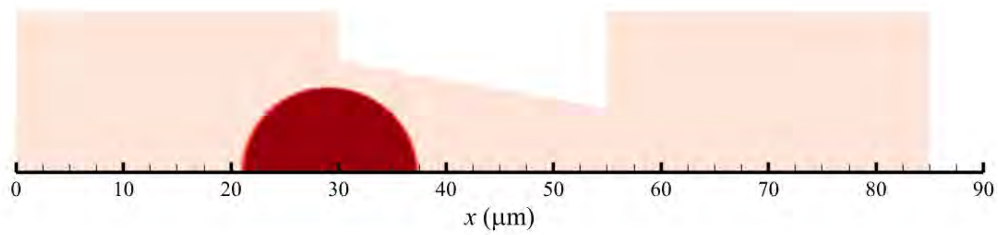
The pressure signatures for the rest of the cases considered are shown in Figures 4.5 to 4.12. Threshold pressure, $P_{\text{threshold}}$ have been calculated for all the cases, the results of which are presented in the next section.



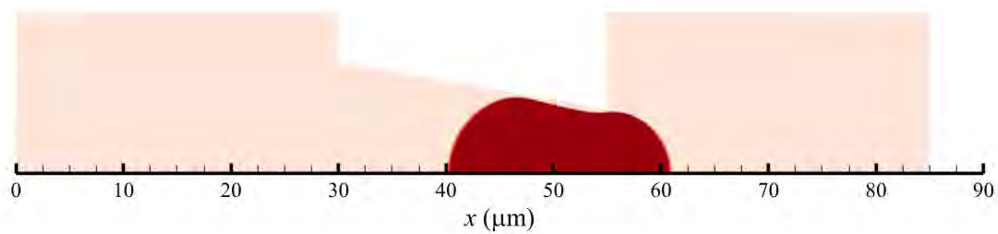
(a)



(b)

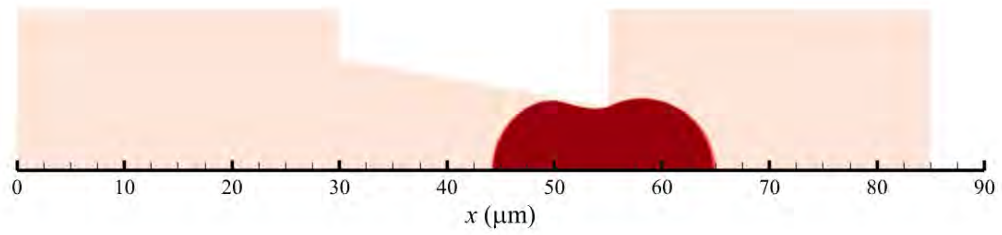


(c)

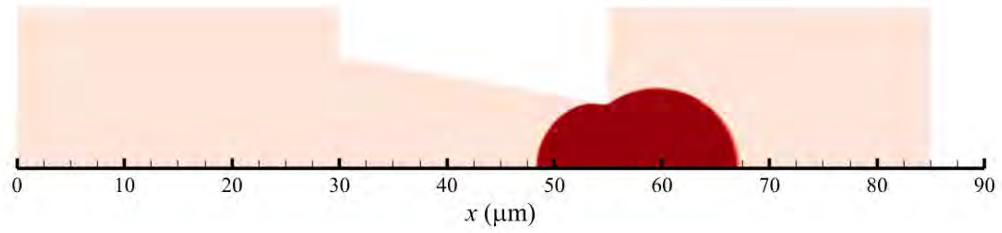


(d)

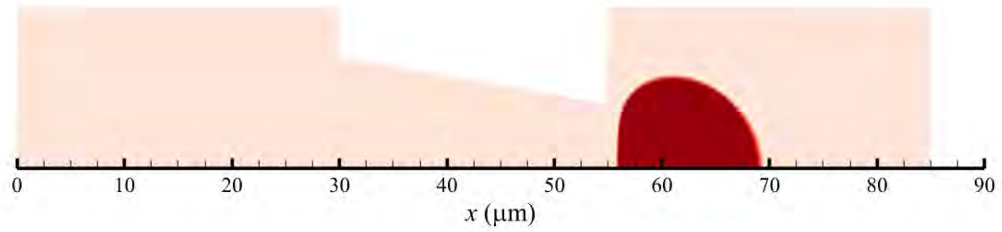
Figure 4.1: (a) Inlet pressure signature for the case: $r_f = 6 \mu\text{m}$, $\sigma = 0.2 \text{ mN/m}$ and $D = 16 \mu\text{m}$, (b)-(i) cell volume fraction showing cell position and deformation at different times during passage through the filter. (cont.)



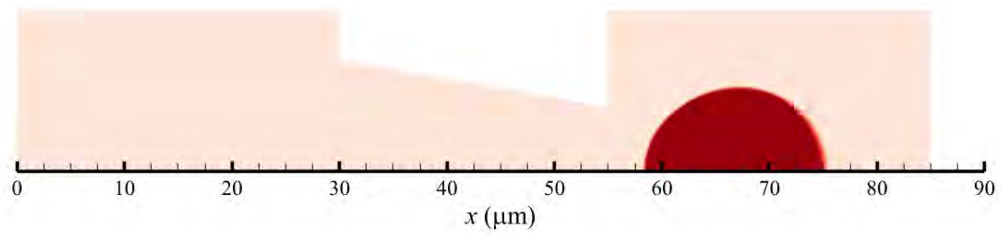
(e)



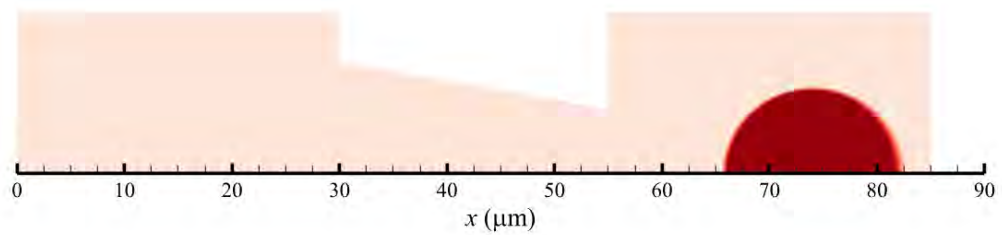
(f)



(g)

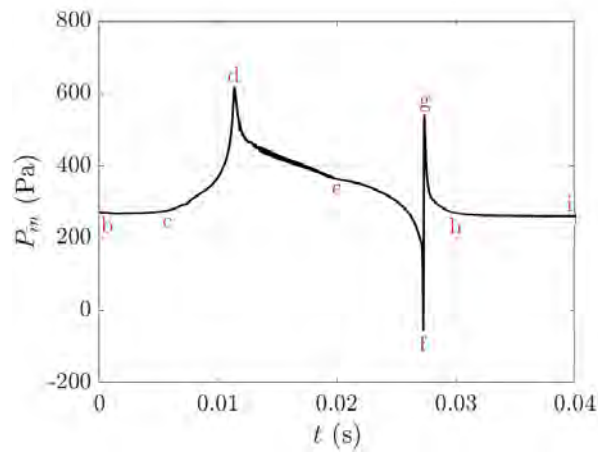


(h)

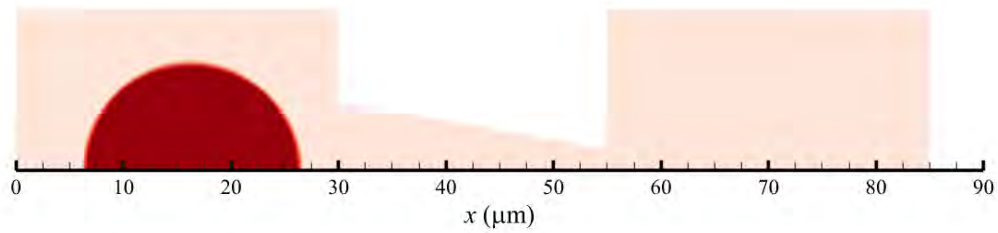


(i)

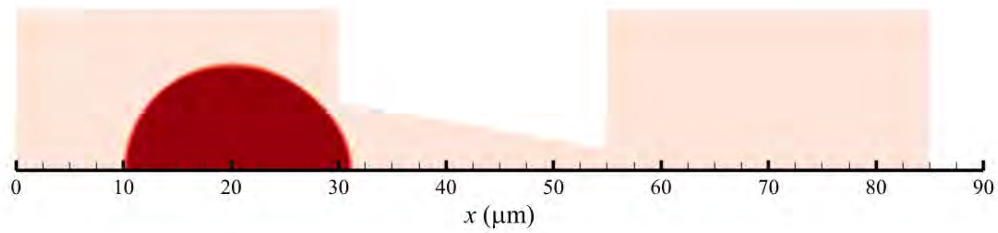
Figure 4.1: (a) Inlet pressure signature for the case: $r_f = 6 \mu\text{m}$, $\sigma = 0.2 \text{ mN/m}$ and $D = 16 \mu\text{m}$, (b)-(i) cell volume fraction showing cell position and deformation at different times during passage through the filter.



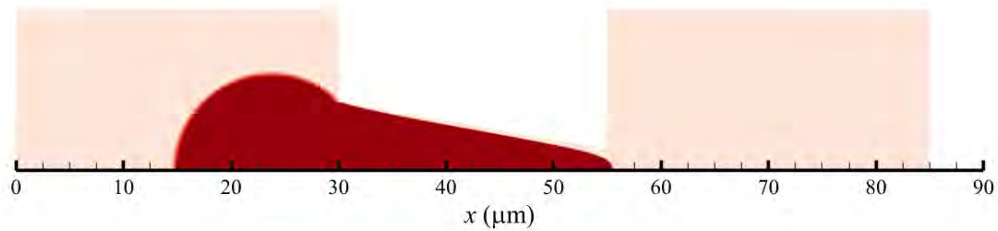
(a)



(b)

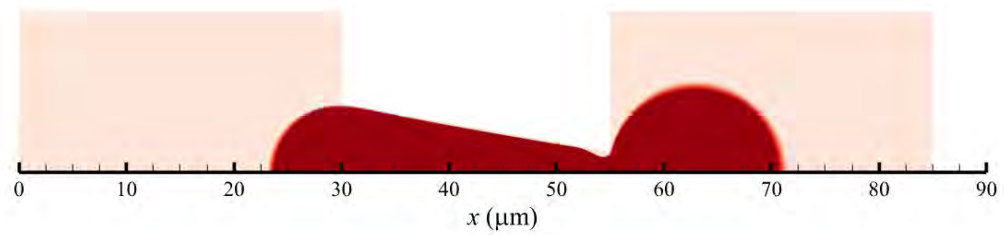


(c)

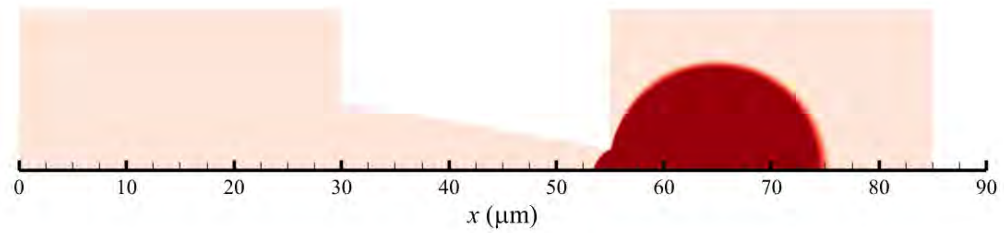


(d)

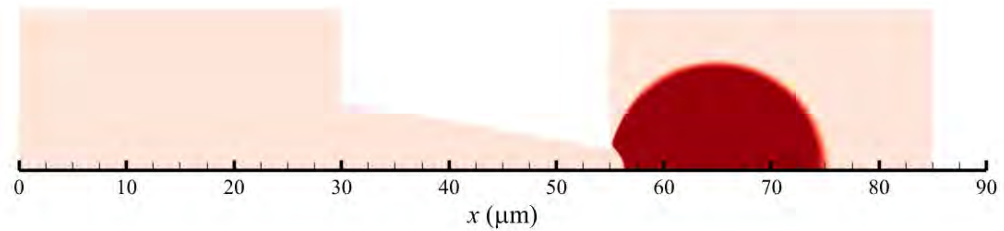
Figure 4.2: (a) Inlet pressure signature for the case: $r_f = 2 \mu\text{m}$, $\sigma = 0.4 \text{ mN/m}$ and $D = 20 \mu\text{m}$, (b)-(i) cell volume fraction showing cell position and deformation at different times during passage through the filter. (cont.)



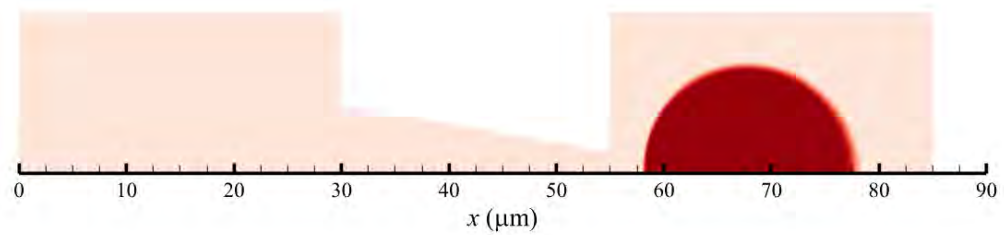
(e)



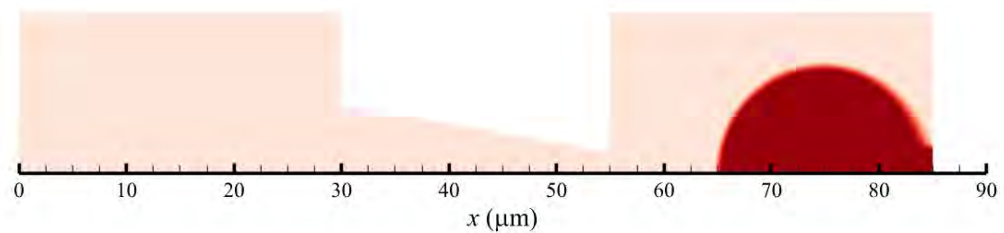
(f)



(g)

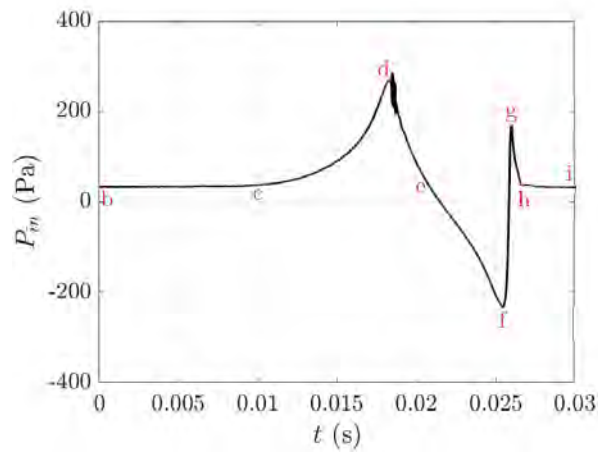


(h)

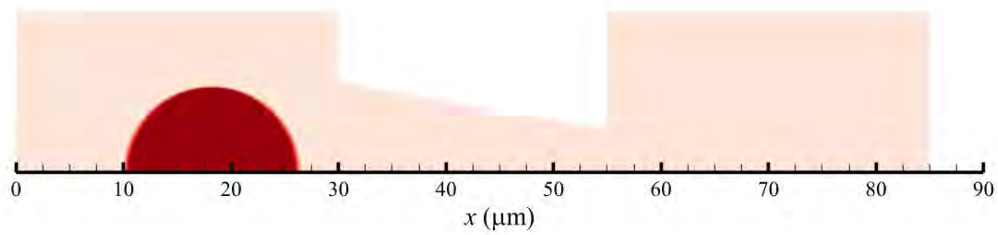


(i)

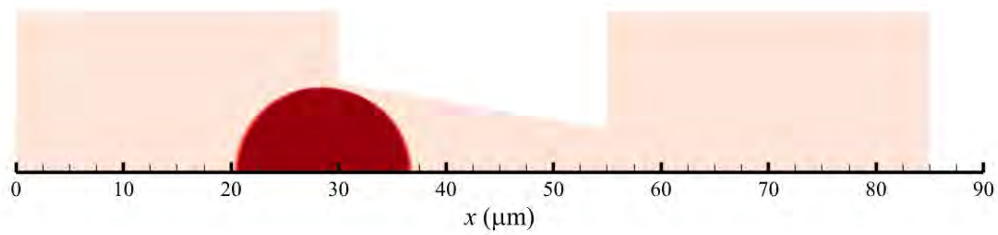
Figure 4.2: (a) Inlet pressure signature for the case: $r_f = 2 \mu\text{m}$, $\sigma = 0.4 \text{ mN/m}$ and $D = 20 \mu\text{m}$, (b)-(i) cell volume fraction showing cell position and deformation at different times during passage through the filter.



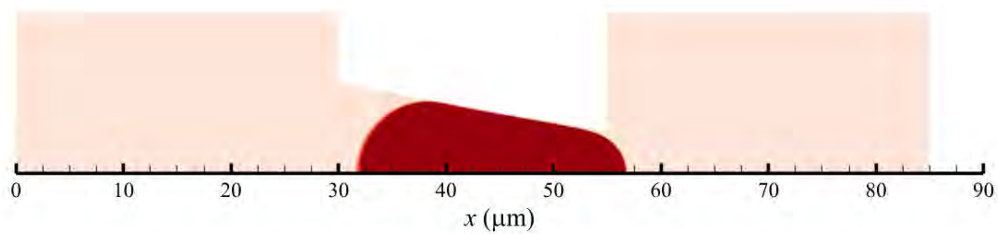
(a)



(b)

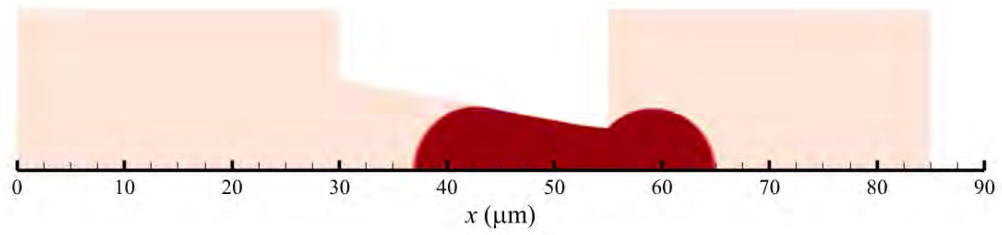


(c)

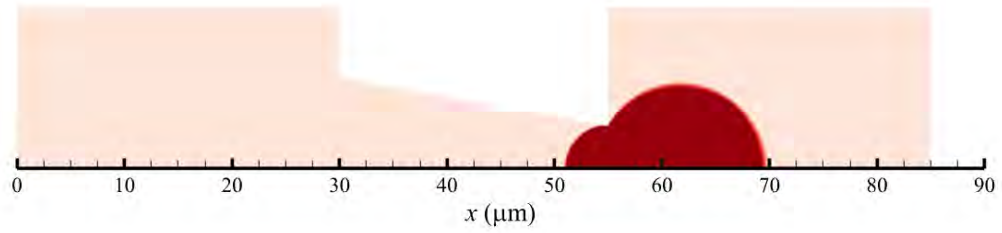


(d)

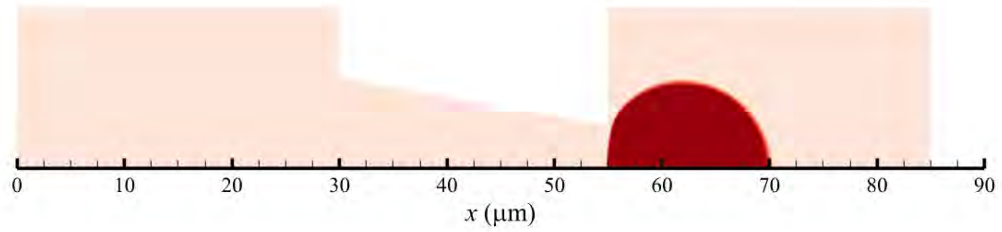
Figure 4.3: (a) Inlet pressure signature for the case: $r_f = 4 \mu\text{m}$, $\sigma = 1.1 \text{ mN/m}$ and $D = 16 \mu\text{m}$, (b)-(i) cell volume fraction showing cell position and deformation at different times during passage through the filter. (cont.)



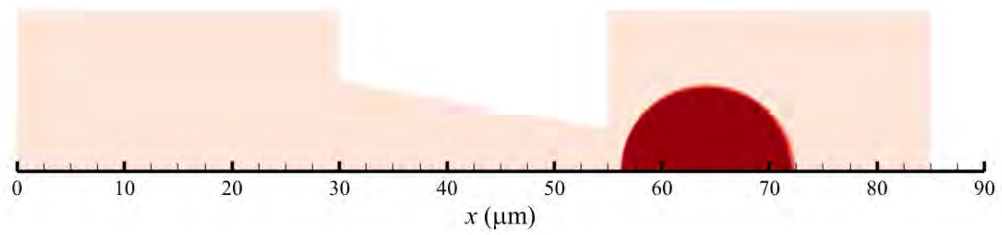
(e)



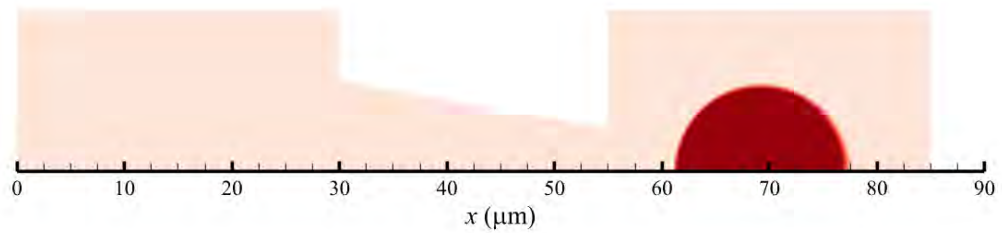
(f)



(g)

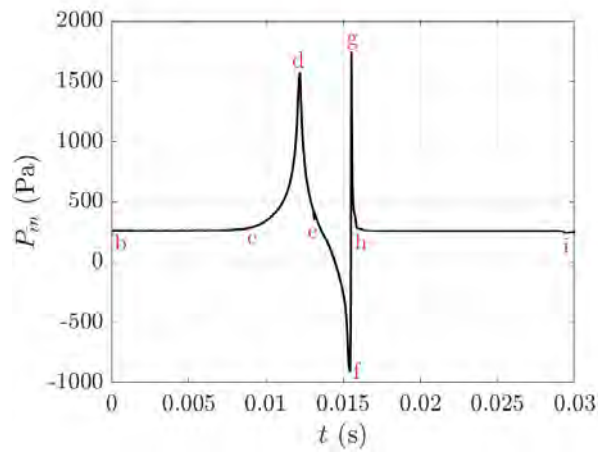


(h)

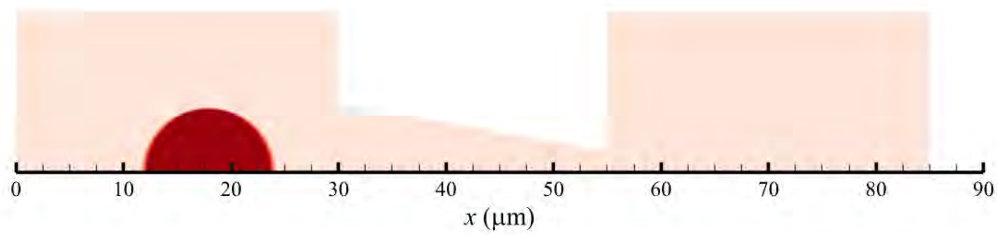


(i)

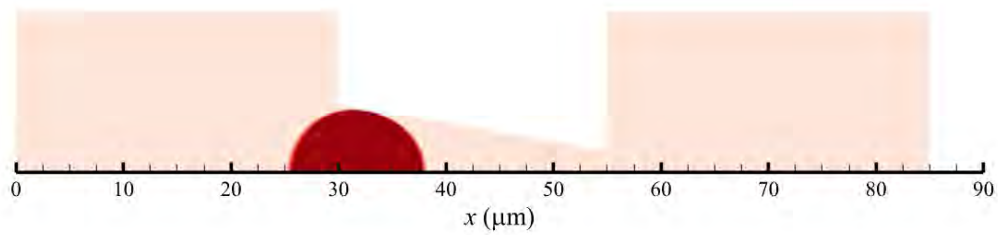
Figure 4.3: (a) Inlet pressure signature for the case: $r_f = 4 \mu\text{m}$, $\sigma = 1.1 \text{ mN/m}$ and $D = 16 \mu\text{m}$, (b)-(i) cell volume fraction showing cell position and deformation at different times during passage through the filter.



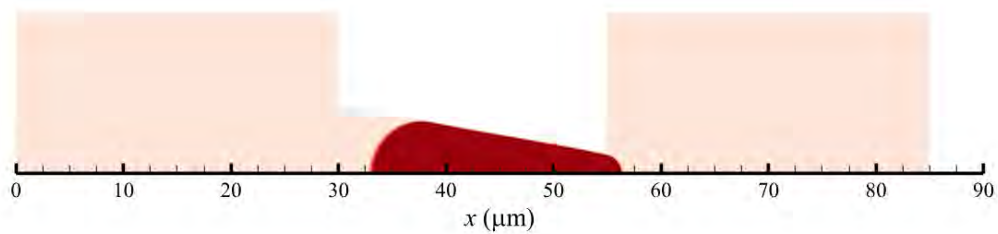
(a)



(b)

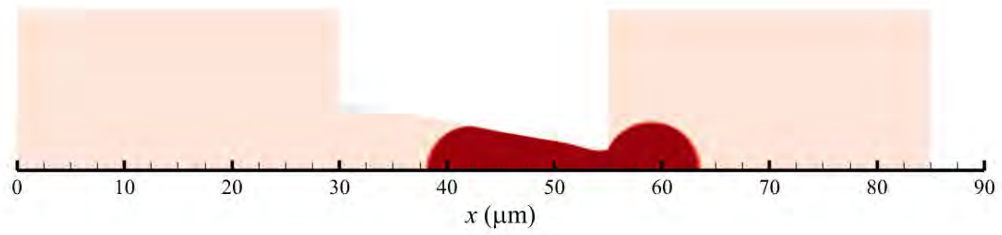


(c)

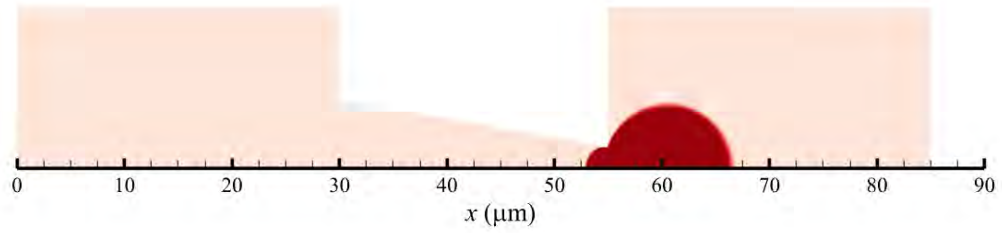


(d)

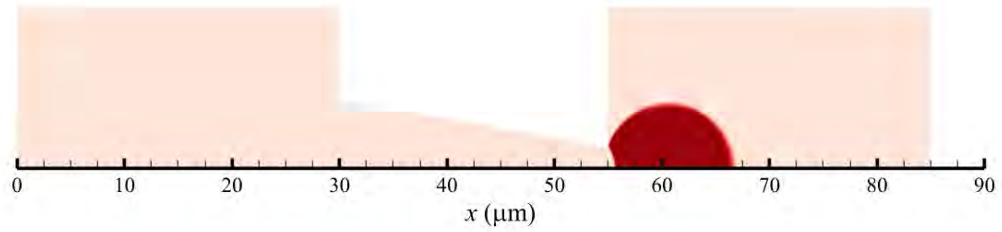
Figure 4.4: (a) Inlet pressure signature for the case: $r_f = 2 \mu\text{m}$, $\sigma = 2 \text{ mN/m}$ and $D = 12 \mu\text{m}$, (b)-(i) cell volume fraction showing cell position and deformation at different times during passage through the filter. (cont.)



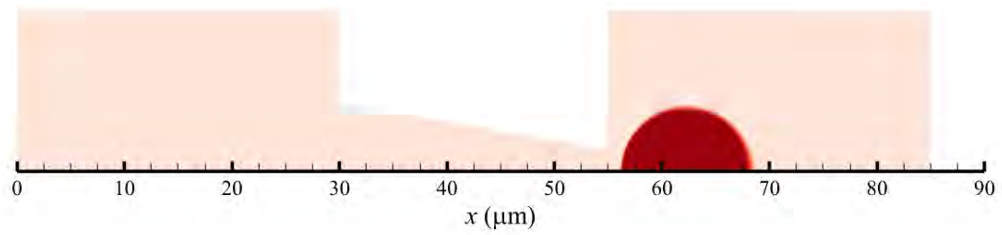
(e)



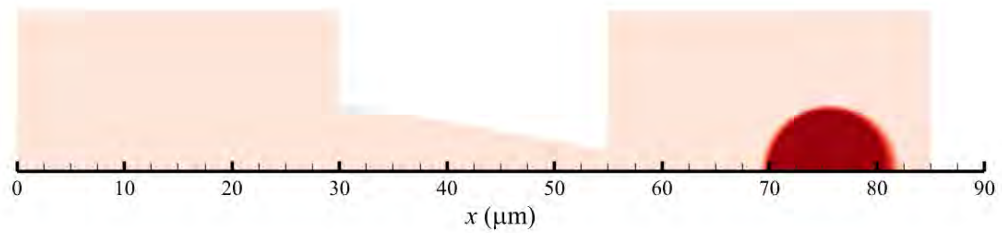
(f)



(g)



(h)



(i)

Figure 4.4: (a) Inlet pressure signature for the case: $r_f = 2 \mu\text{m}$, $\sigma = 2 \text{ mN/m}$ and $D = 12 \mu\text{m}$, (b)-(i) cell volume fraction showing cell position and deformation at different times during passage through the filter.

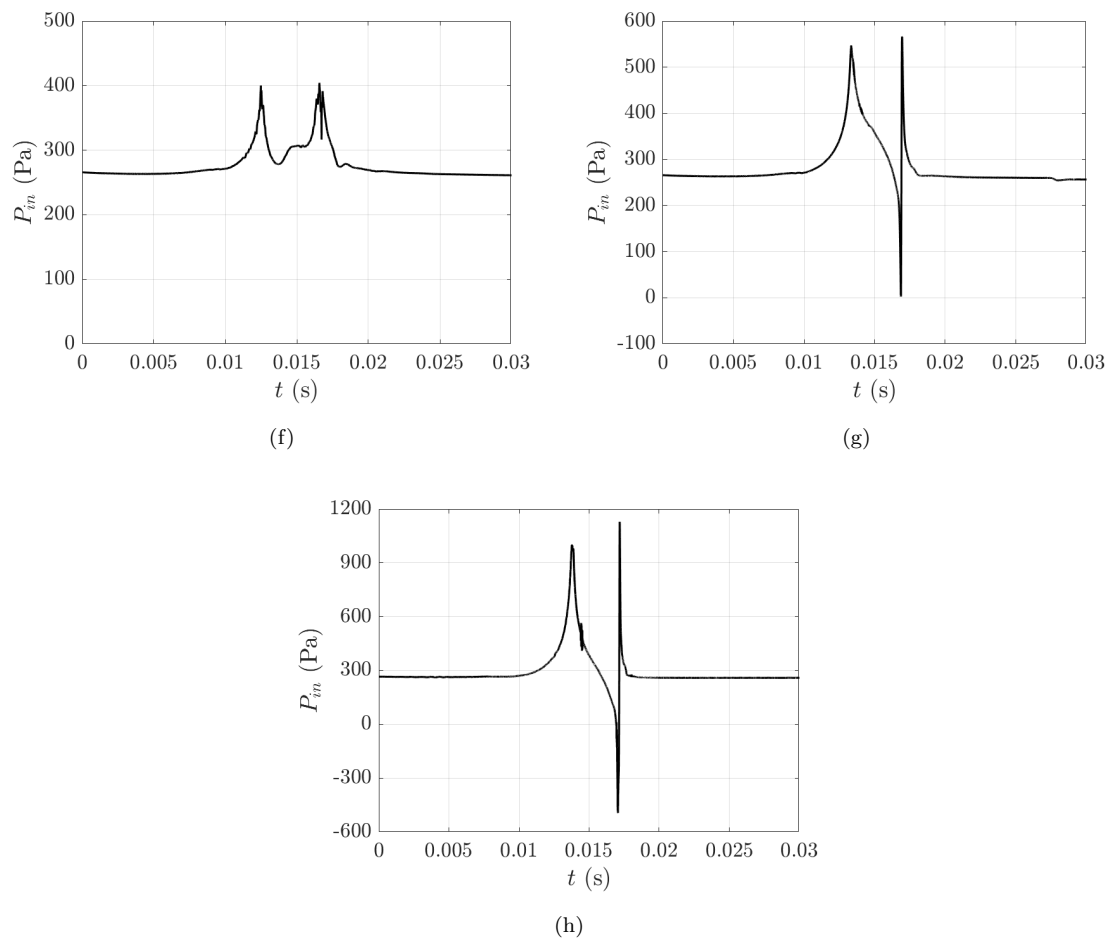


Figure 4.5: Inlet Pressure signature for the cases: $r_f = 2 \mu\text{m}$ and $D = 12 \mu\text{m}$, (a) $\sigma = 0.2 \text{ mN/m}$, (b) $\sigma = 0.4 \text{ mN/m}$ and (c) $\sigma = 1.1 \text{ mN/m}$.

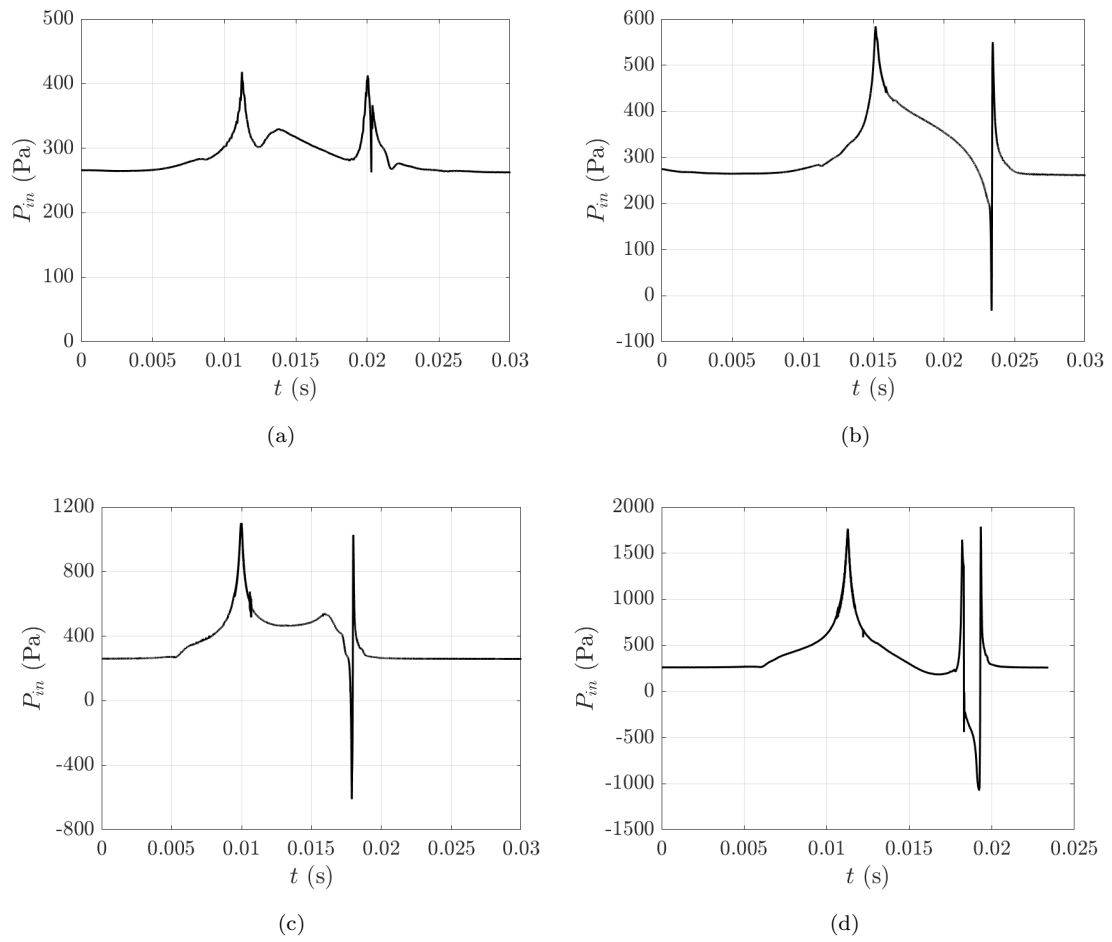


Figure 4.6: Inlet Pressure signature for the cases: $r_f = 2 \mu\text{m}$ and $D = 16 \mu\text{m}$, (a) $\sigma = 0.2$ mN/m, (b) $\sigma = 0.4$ mN/m, (c) $\sigma = 1.1$ mN/m and (d) $\sigma = 2$ mN/m.

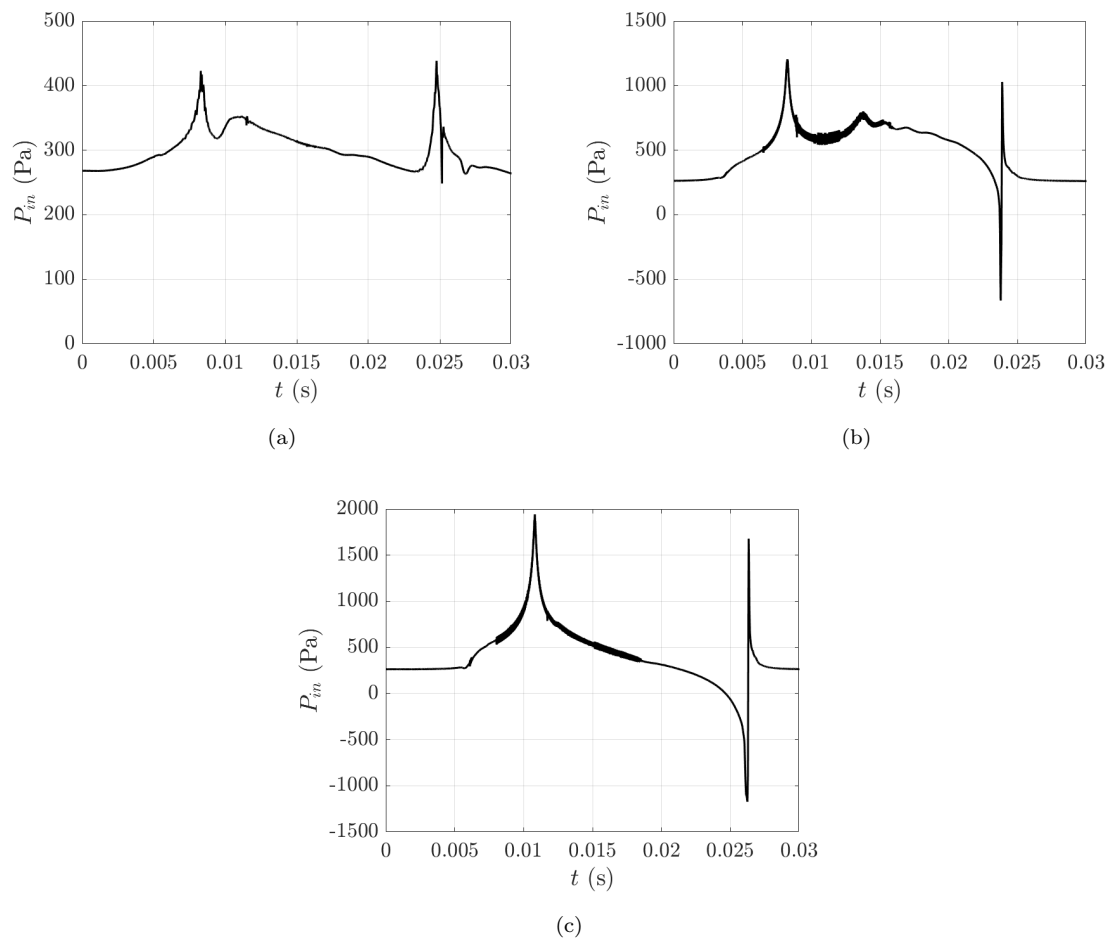


Figure 4.7: Inlet Pressure signature for the cases: $r_f = 2 \mu\text{m}$ and $D = 20 \mu\text{m}$, (a) $\sigma = 0.2$ mN/m, (b) $\sigma = 1.1$ mN/m and (c) $\sigma = 2$ mN/m.

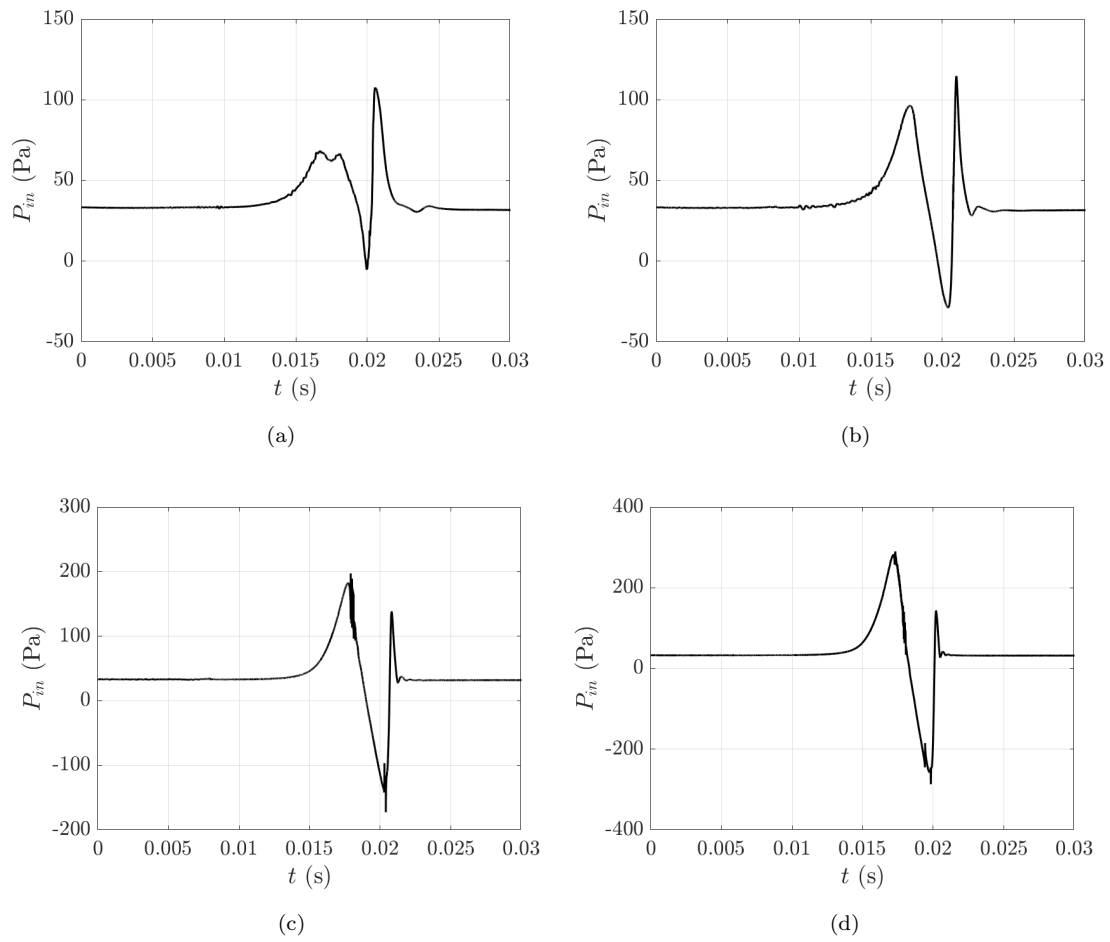


Figure 4.8: Inlet Pressure signature for the cases: $r_f = 4 \mu\text{m}$ and $D = 12 \mu\text{m}$, (a) $\sigma = 0.2$ mN/m, (b) $\sigma = 0.4$ mN/m, (c) $\sigma = 1.1$ mN/m and (d) $\sigma = 2$ mN/m.

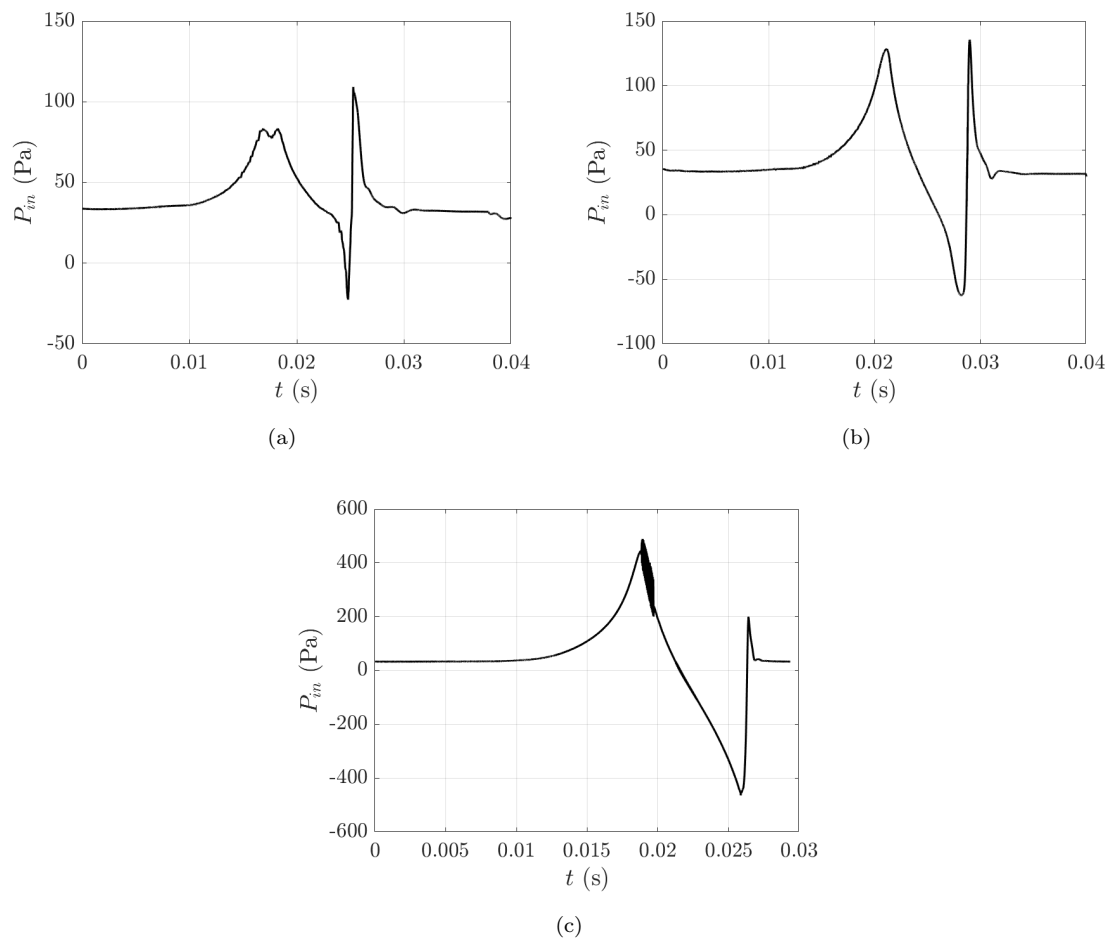


Figure 4.9: Inlet Pressure signature for the cases: $r_f = 4 \mu\text{m}$ and $D = 16 \mu\text{m}$, (a) $\sigma = 0.2$ mN/m, (b) $\sigma = 0.4$ mN/m and (c) $\sigma = 2$ mN/m.

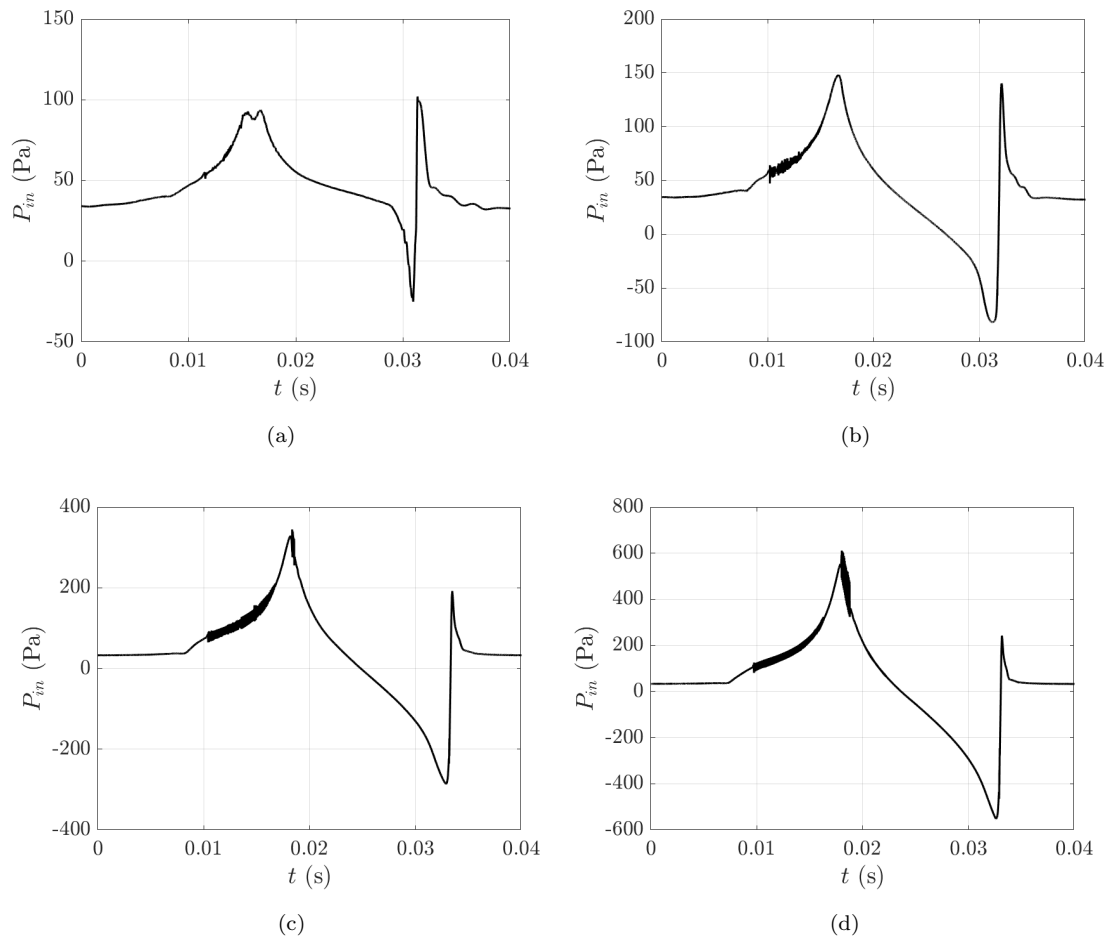


Figure 4.10: Inlet Pressure signature for the cases: $r_f = 4 \mu\text{m}$ and $D = 20 \mu\text{m}$, (a) $\sigma = 0.2$ mN/m, (b) $\sigma = 0.4$ mN/m, (c) $\sigma = 1.1$ mN/m and (d) $\sigma = 2$ mN/m.

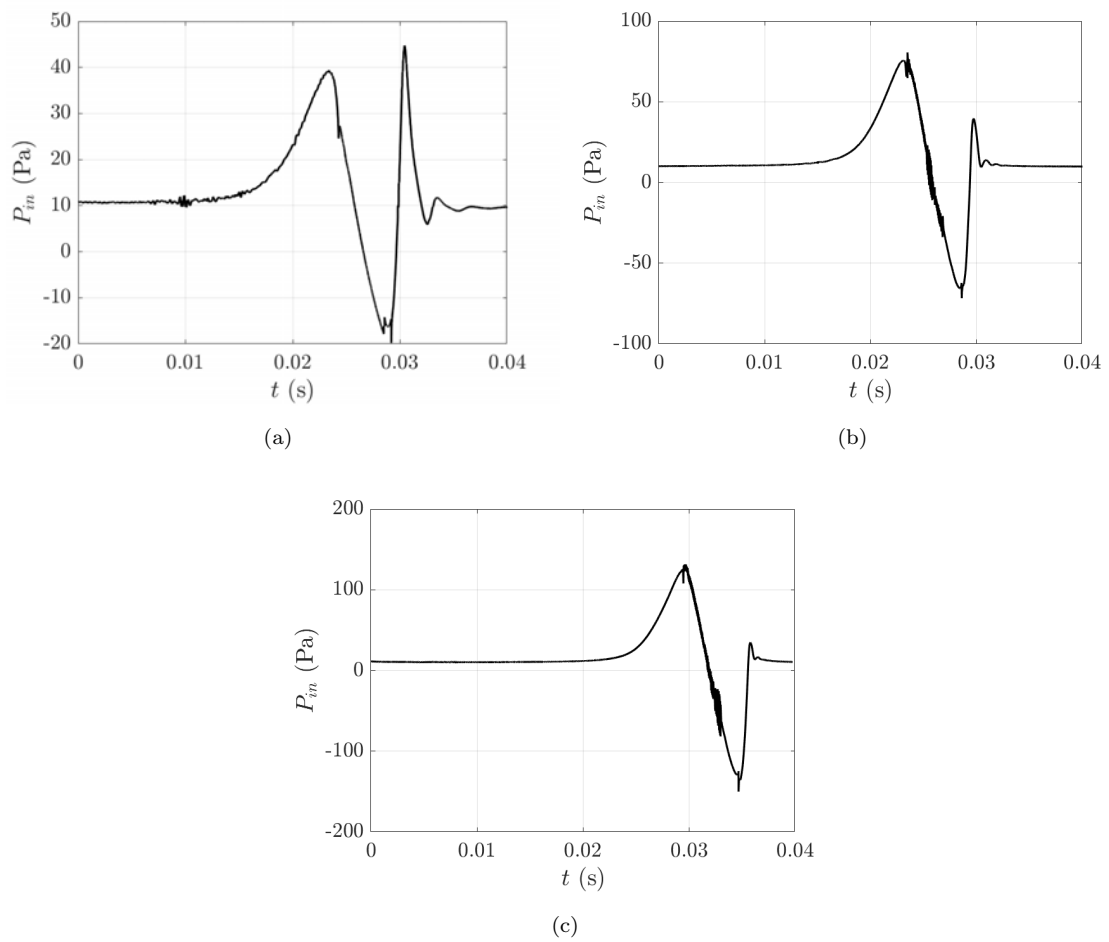


Figure 4.11: Inlet Pressure signature for the cases: $r_f = 6 \mu\text{m}$ and $D = 16 \mu\text{m}$, (a) $\sigma = 0.4$ mN/m, (b) $\sigma = 1.1$ mN/m and (c) $\sigma = 2$ mN/m.

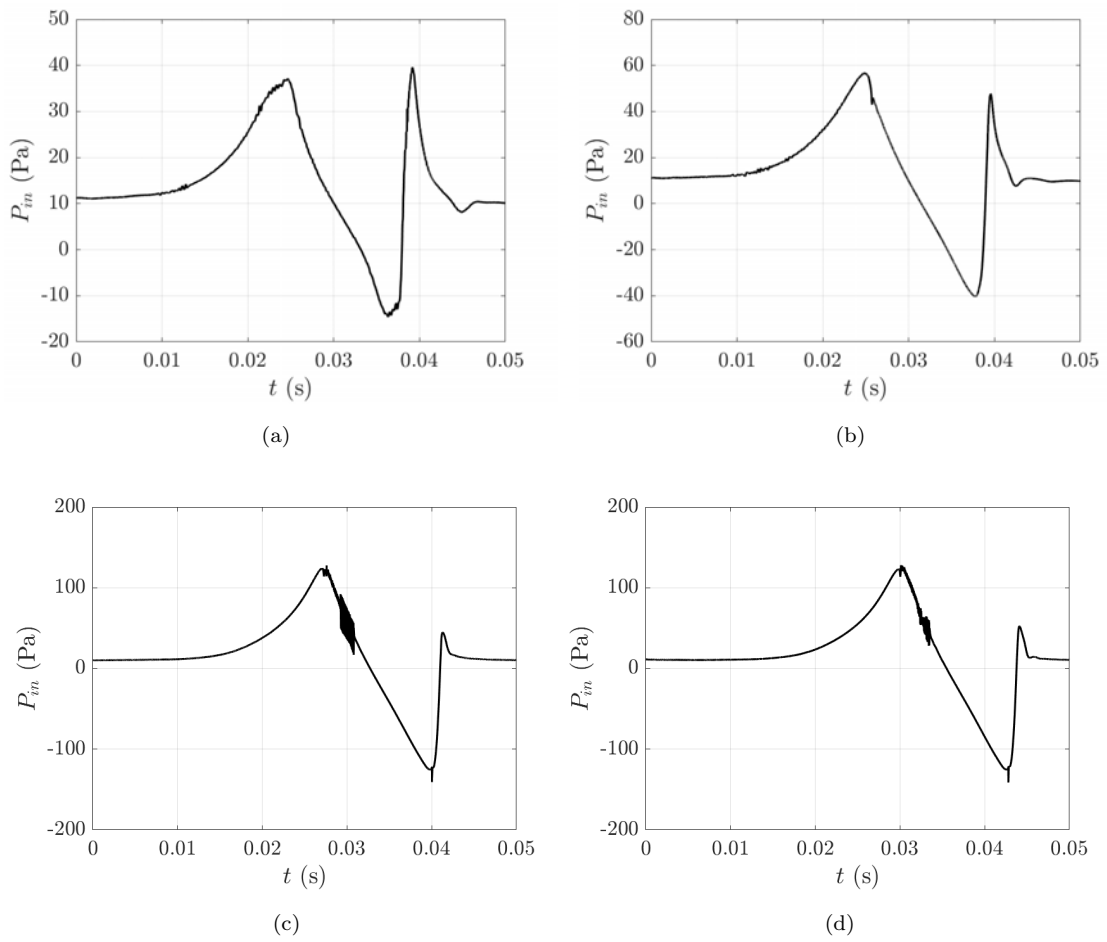


Figure 4.12: Inlet Pressure signature for the cases: $r_f = 6 \mu\text{m}$ and $D = 20 \mu\text{m}$, (a) $\sigma = 0.2$ mN/m, (b) $\sigma = 0.4$ mN/m, (c) $\sigma = 1.1$ mN/m and (d) $\sigma = 2$ mN/m.

4.2 Threshold pressure dependence on filter geometry and cell physical property

Total pressure signatures presented in the previous section have been used to calculate threshold passing pressure $P_{\text{threshold}}$ using the equation 3.1:

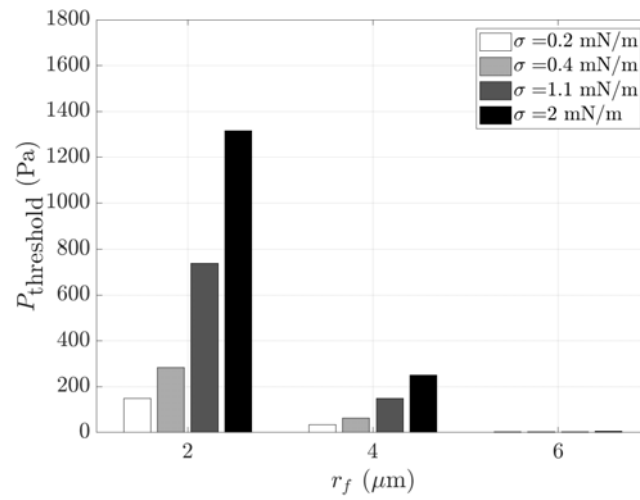
$$P_{\text{threshold}} = P_{\text{in}} - P_{\text{viscous}} \quad (4.3)$$

P_{in} was taken from the first peak of the pressure signature and P_{viscous} was calculated from the initial value of P_{in} when $P_{\text{cortical-tension}}$ is zero. The results are summarized in Figure 4.13. $P_{\text{threshold}}$ values are plotted against filter pore radius r_f with each group of bars showing variation of $P_{\text{threshold}}$ with σ for a fixed value of r_f . The results for cell diameter, D are shown in separate plots. $P_{\text{threshold}}$ has a strong dependence on r_f . Filter funnels with smaller pore radius force the CTCs to deform more. This was also evident in deformation quantification presented in Section 3.3. As a result of this deformation, the threshold pressure required to pass a smaller-sized filter funnel is higher. The values of r_f are linearly spaced. But the variation in threshold pressure moving from a large funnel to a small funnel shows a big jump for the smallest value of r_f . This means smaller funnels produce a very large value of threshold pressure. This is true for all the cell sizes. The case with $r_f = 6\mu\text{m}$ and $D = 12\mu\text{m}$ shows negligible amount of threshold pressure. This is because, $D = 2r_f$, and thus, the cells should pass without any resistance. But the cells deform axially as they pass through the filter exit. This causes them to slightly touch the filter wall, resulting in a small value of threshold pressure.

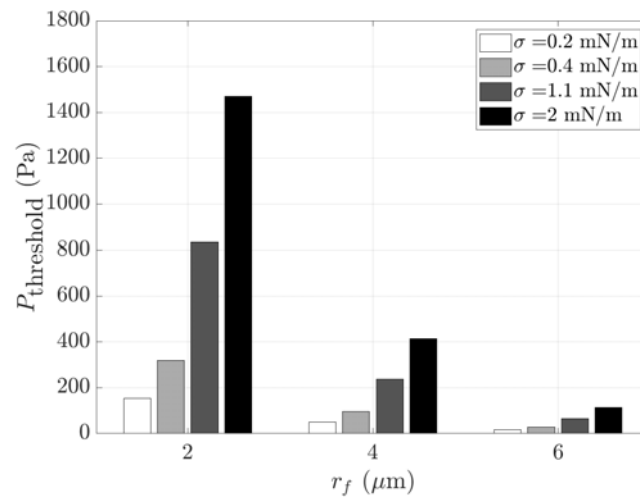
$P_{\text{threshold}}$ also depends strongly on cell cortical tension, σ . For the same amount of deformation, it requires more pressure for a stiffer cell to pass through a filter pore of a given dimension. This is reflected in Figure 4.13. For a given value of r_f , $P_{\text{threshold}}$ is higher for stiffer cells. Finally, cell diameter, D has a somewhat weaker influence on $P_{\text{threshold}}$, with larger cells of constant σ requiring more pressure to pass a filter funnel of given pore radius, r_f . But the change in threshold pressure is much small compared to the other parameters. It is to be noted that the range

of σ considered in this study is much higher than the range of D . The stiffest cell ($\sigma = 2$ mN/m) is 10 times stiffer than the softest cell ($\sigma = 0.2$ mN/m). On the other hand, the largest cell ($D = 20$ μm) is just about 1.5 times larger than the smallest cell ($D = 12$ μm).

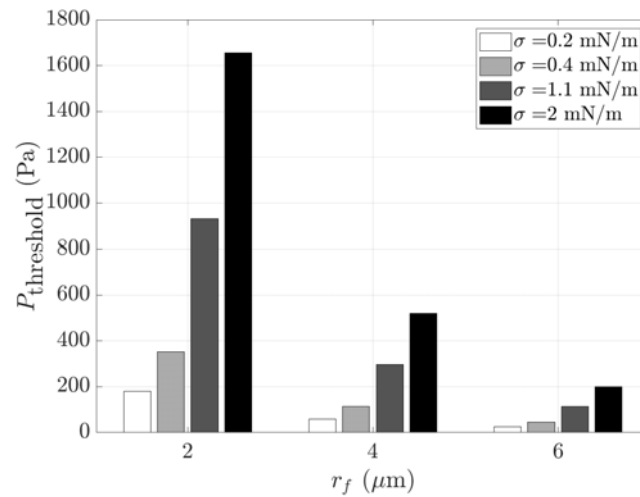
The method to obtain threshold pressure from pressure signature has been used in many other previous studies. Zhang et al. [71] studied the effect of 3D constriction geometry on CTC passing pressure. They considered two types of cells, differing in cortical tension. Aghaamoo et al. [73] reported threshold forward and backward passing pressure in a conical funnel for different funnel pore half angles, θ . They set a fixed value for σ . Zhang et al. [72] studied the effect of viscosity ratio, λ on CTC passing pressure at different inlet velocities. They found threshold pressure to vary with viscosity ratio and flow rate. The flow rate was also shown to affect CTC passing pressure in another study by Zhang et al. [102] At high flow rates, the formation of lubrication layer, which depends on Ca and the change in the leading edge curvature can lead to variation in maximum pressure. But the cortical tension, σ values simulated in these studies are quite high (30- 50 mN/m). In comparison, the highest value of σ used in this study is only 2 mN/m. The inlet flow rate, thus, was selected to be low enough such that it resulted in a variation of Ca within the range of 0.0014- 0.13. In contrast Zhang et al. [102] considered CTCs with Ca in the range of 0.008- 2.



(a)



(b)



(c)

Figure 4.13: Threshold pressure dependence on filter pore radius and cell cortical tension for (a) $D = 12 \mu\text{m}$, (b) $D = 16 \mu\text{m}$ and (c) $D = 20 \mu\text{m}$.

4.3 Establishment of filter characteristics

The results presented in Figure 4.13 can be reorganized to show cortical tension, σ against threshold pressure, $P_{\text{threshold}}$. This is showcased in Figure 4.14. Each line indicates a cell of a given diameter, D passing through a filter funnel of a given pore radius, r_f . Lines for smaller r_f are shifted towards the right indicating higher values of $P_{\text{threshold}}$ required to pass the filter funnel. Similarly, there are shifts in the lines due to increases in D , with the shift being higher at the higher values of σ .

The objective of rearranging the threshold pressure data is to show that the σ - $P_{\text{threshold}}$ graph is divided into regions by the lines indicating the same value of r_f . It will be easier to understand if only a cell for a given value of D is considered. For example, $D=16\ \mu\text{m}$ gives three lines (as does any other value of D) for funnels 1, 2, and 3. The values on a given line give $P_{\text{threshold}}$ for a given value of σ . If the applied pressure is larger than this value of $P_{\text{threshold}}$, the cell will pass through the filter funnel. If the value is less, then the cell will get trapped. Thus, for a given line, the region at the right indicates cells passing through that filter funnel, whereas the region at the left indicates cells getting trapped. Now, for a filter funnel array, there will be as many lines as the number of filter funnels. Funnels with smaller r_f will have lines shifted right as they require higher pressure. If the funnels are arranged such that the r_f gradually decreases, a cell that passes a given funnel can be trapped in the next funnel that has a smaller value of r_f and thus a larger value of $P_{\text{threshold}}$. For each funnel, its characteristic line divides the σ - $P_{\text{threshold}}$ graph into two regions: pass and no-pass. For the next funnel in the funnel array with a smaller r_f , the characteristic line sits at the pass zone of the previous funnel. The region in between thus indicates cells getting trapped between the two funnels.

The entire σ - $P_{\text{threshold}}$ graph can be divided into multiple regions depending upon the number of funnels. For this study, three filter funnels were considered for the array. This means there are four regions: cells getting trapped in filter 1, between filter 1 and 2 (indicated as filter 2), between filter 2 and 3 (indicated as filter 3), and cells passing all the filter funnels to the exit chamber. The regions are shown in Figure 4.15 for all the values of cell diameter, D . The red region indicates cells

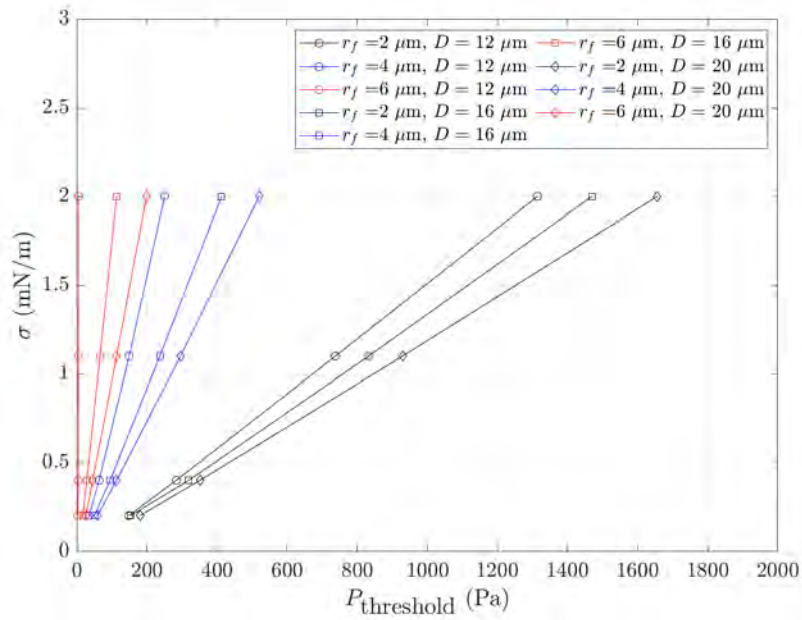
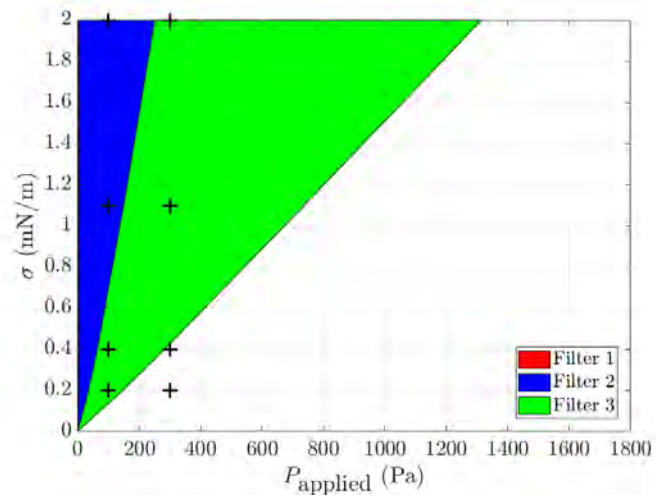


Figure 4.14: Threshold pressure dependence on cell cortical tension for different pore radius and cell size.

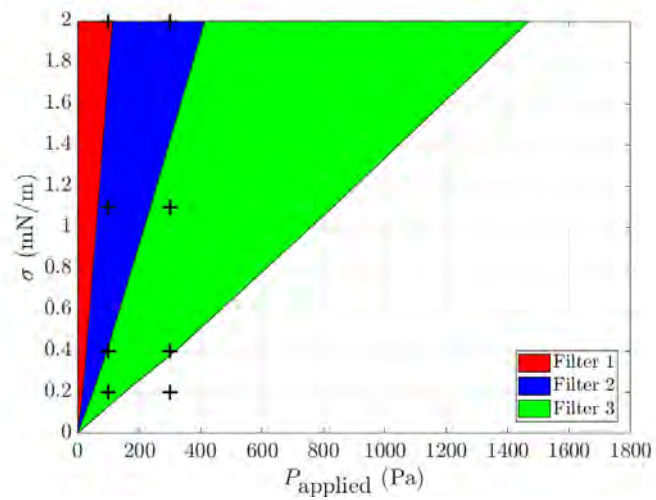
getting trapped in filter 1, the blue in filter 2, and the green in filter 3. The white region at the right indicates the exit chamber. The regions are shifted for an increase in D . The array simulation cases are shown with symbols. It is apparent that the cases are separated and thus sorted into different regions based on the applied inlet pressure, P_{applied} , cell cortical tension, σ , and cell diameter, D .

The utility of the charts in 4.15 is in both operation and design of a filter device for capturing cancer cells in a specific range of physical properties. It was shown in the chapter 3 that CTC trapping and sorting in different filter funnels depend on the applied pressure. This can be readily seen from Figure 4.15. A vertical line at any pressure value intersects the region boundaries at different values of σ . These values will give the ranges of cell cortical tension, which will get trapped in different filter funnels. Taking another vertical line for a different applied pressure leads to a different range of σ . It is to be remembered that this range will be shifted by a change in cell diameter, D .

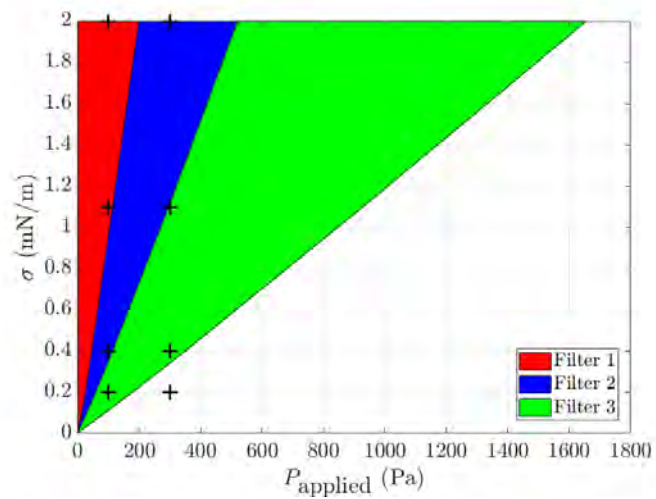
This study only considered three filter funnels. More funnels can be incorporated in the device with a more gradual change in r_f , giving a higher resolution of the ranges of σ and D . For a given filter design, the chart gives ranges of CTC physical



(a)



(b)



(c)

Figure 4.15: Filter characteristic chart for (a) $D = 12 \mu\text{m}$, (b) $D = 16 \mu\text{m}$, (c) $D = 20 \mu\text{m}$.

properties for a given applied pressure. Cell viability after sorting [29] is important for subsequent analysis and characterization of CTCs. Cells experiencing higher pressure during deformation or trapping can lead to cell damage. This brings constraints on the applied pressure range that can be used. For such cases, for a given range of applied pressure, filters can be designed based on the charts given in Figure 4.15, so that CTCs of particular ranges of physical properties can be trapped and sorted.

Chapter 5

Conclusions

5.1 Summary

In the present work, motion and deformation of circulating tumor cells (CTCs) in conical microfluidic filters were studied in order to demonstrate isolation and sorting in a filter array device according to cell physical properties. Filter operating characteristics were established from the threshold pressure required for a CTC to pass a single filter funnel. Cell passing through the filters was modeled as a two-phase flow while cell mechanical behavior was simulated by a Newtonian droplet with constant cortical tension and viscosity. Numerical simulations were conducted for different values of filter pore size and CTCs having a range of cortical tension and diameter.

Trapping and isolation of CTCs were simulated by pressure-driven flow in a filter array device consisting of funnels with progressively smaller pore radius. Two different inlet pressures were used to investigate the effect of driving pressure. The cells were found to be trapped in different filter funnels. Cell trapping was demonstrated by inlet flow rate and cell center of mass position history. In the trapped phase, cell position became fixed, with the inlet flow rate decreasing to zero. The specific funnel in which a cell got trapped depended on both cell size and cortical tension. Smaller and softer cells were found to be trapped further forward in the

funnel array device in progressively smaller-sized filter funnels. Whereas larger and stiffer cells were trapped earlier in funnels with larger filter pore radius. This indicates that these cells require more pressure to be able to deform and pass through funnels. Thus, the cells were sorted in the filter funnels according to their physical properties under study. The specific sorting pattern changed when the applied inlet pressure was increased. The increased driving pressure enabled the cells to move further forward towards smaller funnels. This means the ranges of physical properties of the sorted cells in specific filter funnels are dependent upon the inlet driving pressure. Some softer cells were found to escape the funnel array device, indicating that lower pressure is required to trap them in a funnel.

Cell deformation in filter funnels was quantified by using the cell axial deformation index. The index is an indicator of cell elongation in the axial direction compared to their original size. Axial deformation index history for several cases showed that deformation depends primarily on the filter funnel a cell gets trapped in. Cells traveling to smaller funnels undergo more deformation. For 300 Pa driving pressure, the axial length of the deformed cells was found to be up to 2.5 times the original diameter. The maximum value was about 2 for 100 Pa driving pressure. As mentioned above, under higher driving pressure, cells can travel towards smaller funnels and thus produce more deformation. For some cases, especially for 300 Pa driving pressure, axial deformation was also found to be less than 1. This indicates axial squeezing of the cells. The squeezing occurs when the cells recoil after coming out of filter funnels.

Simulations at a constant inlet flow rate of 0.27 nL/s were performed to calculate threshold passing pressure from inlet total pressure signatures. The threshold pressure values were shown to be highly dependent on filter funnel pore radius and cell cortical tension. Cell diameter also had an effect on the threshold passing pressure. Threshold pressure was higher for smaller funnels indicating more deformation of a CTC in a funnel. The jump in pressure between funnels of smaller pore size is also higher. Similarly, threshold pressure was found to increase with cortical tension, indicating stiffer cells requiring more pressure to pass through a funnel. On the other hand, larger cells also produced an increase in threshold pressure. But

the difference was smaller compared to funnel pore radius and cortical tension for the range of cell diameter studied. Based on the calculated threshold pressure values, the filter array device was characterized for operation at different inlet driving pressures. The specific driving pressure was shown to sort cells in different funnels according to a range in cell cortical tension. The range shifts a little for a cell of different diameters. The physical property ranges for cell sorting were shown to be dependent upon the inlet total pressure, which corroborates findings from filter array simulations.

5.2 Contributions

The current study had the objective to explicate the dependence of circulating tumor cell trapping patterns on physical properties in a microfluidic filter array device. In addition, a method was to be established to predict how this trapping pattern changes under different filter operating conditions.

The first part of this study revealed that CTCs could not only be detected but also be sorted in a filter array device according to their size and cortical tension. CTC detection and enumeration have great value in the early detection and treatment management of cancer. In addition, changes in deformability have also been reported to indicate the metastatic potential of CTCs in some forms of cancer. Together, the filter array device can facilitate detection and biomechanical characterization before a further biological study is undertaken. Changes in sorting patterns under different driving pressure gave clues to customization of device operational parameters for targeted detection and sorting of CTCs within a predetermined physical property range.

In the second part of this study, the filter array device was characterized by finding the threshold pressure required for CTCs of different physical properties and filter pore size. The device characterization confirmed the change in CTC sorting pattern under different driving pressure. The characterization works as a predictive tool that can lead to optimization in use by the selection of driving pressure for a filter

of a given geometry. Driving pressure can be adjusted so that CTCs of a specific physical property range can be trapped. A similar characterization process can be performed for different filter geometric parameters before the construction of a practical device. This will lead to optimization in design for detection of CTCs of a particular physical property range. The physical property range can also be finely resolved by using of more pores in the filter array. In addition, cell viability for subsequent analysis can also be ensured in the design phase by the limitation of pressure felt by a cell while passing through the filter pores.

In conclusion, The present work provides a method for both operation and design of microfluidic filter array devices for trapping and sorting of CTCs having a range of cortical tension and size.

5.3 Possible application of the filter array device

As discussed previously, practical microfluidic filter devices [51, 61, 62] with arrays of funnels have been constructed to demonstrate the isolation of cancer cells from peripheral blood. Guo et al. [59] measured cell physical properties using microfluidic funnel constrictions. The present work combines these two types of studies to show that a filter array device can both isolate and sort circulating tumor cells based on their physical properties. For funnel geometry, conical funnels were selected for this study. Patient blood samples can be collected and driven through the device under pressure to trap CTCs (if any) in peripheral blood. Detection and enumeration of CTCs in blood have been shown to have importance in early cancer detection and treatment management. The trapped cells can be unclogged under reverse pressure and collected for further study. In addition, the sorted cells in specific funnels reveal information about their physical properties. Properties like deformability have been shown to be an indicator of metastatic potential in some forms of cancer.

5.4 Limitations and scope of future work

The CTC was modeled as a Newtonian droplet having a constant viscosity equal to that of plasma. But there is experimental evidence that cancer cells are highly viscous [93]. The effect of cell viscosity on CTC passing pressure has been studied before [72]. This study only focuses on cell size and stiffness. Studies can be performed by including cell viscosity as another physical property. The cell behavior model in this study used surface tension to emulate cell cortical tension. This model neglects any internal structure of the cell. But CTCs can have large nuclear to cytoplasmic ratio [25] and the nucleus affects CTC deformation through micro-constrictions [115]. Numerical studies incorporating cell nuclei in the cell behavior model can be performed to predict the effect of the nucleus on cell deformability in microfilters. The Newtonian droplet model is adequate for predicting pressure and large cell deformation in microfilters [58]. For transient deformation behavior of cells, viscoelastic or solid models can be used [95].

For the filter array device, only three filters were considered. Although three filters were enough to demonstrate cell trapping and sorting in an array device, adding more filters with a gradual change in filter pore diameter, r_f will give better resolution in physical properties of the captured cells. The current work only considered 2D axisymmetric conical filters. A conclusion similar to this study can also be made for three-dimensional filters. As discussed previously, cell viability after filtration is important for further analysis and characterization of the captured cells, which has been considered by a few previous studies [65, 67]. The stresses felt by a cell during its passage through a micro-constriction can be used to study cell viability by incorporating cell damage models. Adjustment to the applied inlet pressure or filter geometry can be made based on cell viability studies.

Bibliography

- [1] J. Ferlay, M. Ervik, F. Lam, M. Colombet, L. Mery, and M. Piñeros, “Global cancer observatory: Cancer today, international agency for research on cancer.” <https://gco.iarc.fr/today/>, accessed September, 2021.
- [2] W. H. Organization, “Cancer.” <https://www.who.int/news-room/fact-sheets/detail/cancer>, accessed September, 2021.
- [3] C. Alix-Panabières, H. Schwarzenbach, and K. Pantel, “Circulating tumor cells and circulating tumor dna,” *Annual review of medicine*, vol. 63, pp. 199–215, 2012.
- [4] K. Pantel and M. Speicher, “The biology of circulating tumor cells,” *Oncogene*, vol. 35, no. 10, pp. 1216–1224, 2016.
- [5] C. L. Chaffer and R. A. Weinberg, “A perspective on cancer cell metastasis,” *science*, vol. 331, no. 6024, pp. 1559–1564, 2011.
- [6] R. A. Weinberg, *The biology of cancer*. Garland science, 2013.
- [7] T. Iwamoto, “Clinical application of drug delivery systems in cancer chemotherapy: review of the efficacy and side effects of approved drugs,” *Biological and pharmaceutical bulletin*, vol. 36, no. 5, pp. 715–718, 2013.
- [8] G. Delaney, S. Jacob, C. Featherstone, and M. Barton, “The role of radiotherapy in cancer treatment: estimating optimal utilization from a review of evidence-based clinical guidelines,” *Cancer: Interdisciplinary International Journal of the American Cancer Society*, vol. 104, no. 6, pp. 1129–1137, 2005.

- [9] S. J. Oiseth and M. S. Aziz, “Cancer immunotherapy: a brief review of the history, possibilities, and challenges ahead,” *Journal of cancer metastasis and treatment*, vol. 3, pp. 250–261, 2017.
- [10] E. Heitzer, S. Perakis, J. B. Geigl, and M. R. Speicher, “The potential of liquid biopsies for the early detection of cancer,” *NPJ precision oncology*, vol. 1, no. 1, pp. 1–9, 2017.
- [11] J. D. Schiffman, P. G. Fisher, and P. Gibbs, “Early detection of cancer: past, present, and future,” *American Society of Clinical Oncology Educational Book*, vol. 35, no. 1, pp. 57–65, 2015.
- [12] H. Cho, A. B. Mariotto, L. M. Schwartz, J. Luo, and S. Woloshin, “When do changes in cancer survival mean progress? the insight from population incidence and mortality,” *Journal of the National Cancer Institute Monographs*, vol. 2014, no. 49, pp. 187–197, 2014.
- [13] C. Alix-Panabières and K. Pantel, “Clinical applications of circulating tumor cells and circulating tumor dna as liquid biopsy,” *Cancer discovery*, vol. 6, no. 5, pp. 479–491, 2016.
- [14] F. S. Iliescu, D. P. Poenar, F. Yu, M. Ni, K. H. Chan, I. Cima, H. K. Taylor, I. Cima, and C. Iliescu, “Recent advances in microfluidic methods in cancer liquid biopsy,” *Biomicrofluidics*, vol. 13, no. 4, p. 041503, 2019.
- [15] P. R. Gascoyne, S. Shim, J. Noshari, F. F. Becker, and K. Stemke-Hale, “Correlations between the dielectric properties and exterior morphology of cells revealed by dielectrophoretic field-flow fractionation,” *Electrophoresis*, vol. 34, no. 7, pp. 1042–1050, 2013.
- [16] S. E. Cross, Y.-S. Jin, J. Rao, and J. K. Gimzewski, “Nanomechanical analysis of cells from cancer patients,” *Nature nanotechnology*, vol. 2, no. 12, pp. 780–783, 2007.
- [17] J. Guck, S. Schinkinger, B. Lincoln, F. Wottawah, S. Ebert, M. Romeyke, D. Lenz, H. M. Erickson, R. Ananthakrishnan, D. Mitchell, *et al.*, “Optical

- deformability as an inherent cell marker for testing malignant transformation and metastatic competence,” *Biophysical journal*, vol. 88, no. 5, pp. 3689–3698, 2005.
- [18] W. J. Allard, J. Matera, M. C. Miller, M. Repollet, M. C. Connelly, C. Rao, A. G. Tibbe, J. W. Uhr, and L. W. Terstappen, “Tumor cells circulate in the peripheral blood of all major carcinomas but not in healthy subjects or patients with nonmalignant diseases,” *Clinical cancer research*, vol. 10, no. 20, pp. 6897–6904, 2004.
- [19] D. Marrinucci, K. Bethel, R. H. Bruce, D. N. Curry, B. Hsieh, M. Humphrey, R. T. Krivacic, J. Kroener, L. Kroener, A. Ladanyi, *et al.*, “Case study of the morphologic variation of circulating tumor cells,” *Human pathology*, vol. 38, no. 3, pp. 514–519, 2007.
- [20] M. Marcuello, V. Vymetalkova, R. P. Neves, S. Duran-Sanchon, H. M. Vedeld, E. Tham, G. van Dalum, G. Flügen, V. Garcia-Barberan, R. J. Fijneman, *et al.*, “Circulating biomarkers for early detection and clinical management of colorectal cancer,” *Molecular Aspects of Medicine*, vol. 69, pp. 107–122, 2019.
- [21] M. Ilie, V. Hofman, E. Long-Mira, E. Selva, J.-M. Vignaud, B. Padovani, J. Mouroux, C.-H. Marquette, and P. Hofman, ““sentinel” circulating tumor cells allow early diagnosis of lung cancer in patients with chronic obstructive pulmonary disease,” *PloS one*, vol. 9, no. 10, p. e111597, 2014.
- [22] B. Rack, C. Schindlbeck, J. Jückstock, U. Andergassen, P. Hepp, T. Zwingers, T. W. Friedl, R. Lorenz, H. Tesch, P. A. Fasching, *et al.*, “Circulating tumor cells predict survival in early average-to-high risk breast cancer patients,” *Journal of the National Cancer Institute*, vol. 106, no. 5, p. dju066, 2014.
- [23] S. H. Lim, T. M. Becker, W. Chua, N. J. Caixeiro, W. Ng, N. Kienzle, A. Tognela, S. Lumba, J. E. Rasko, P. De Souza, *et al.*, “Circulating tumour cells and circulating free nucleic acid as prognostic and predictive biomarkers in colorectal cancer,” *Cancer letters*, vol. 346, no. 1, pp. 24–33, 2014.

- [24] L. Antonuzzo, G. Meoni, and F. Di Costanzo, "Are circulating tumor cells a new, valid prognostic marker in neuroendocrine tumors?," *Journal of clinical oncology: official journal of the American Society of Clinical Oncology*, vol. 31, no. 19, pp. 2518–2518, 2013.
- [25] S. Meng, D. Tripathy, E. P. Frenkel, S. Shete, E. Z. Naftalis, J. F. Huth, P. D. Beitsch, M. Leitch, S. Hoover, D. Euhus, *et al.*, "Circulating tumor cells in patients with breast cancer dormancy," *Clinical cancer research*, vol. 10, no. 24, pp. 8152–8162, 2004.
- [26] M. G. Krebs, J.-M. Hou, T. H. Ward, F. H. Blackhall, and C. Dive, "Circulating tumour cells: their utility in cancer management and predicting outcomes," *Therapeutic advances in medical oncology*, vol. 2, no. 6, pp. 351–365, 2010.
- [27] E. A. Punnoose, S. Atwal, W. Liu, R. Raja, B. M. Fine, B. G. Hughes, R. J. Hicks, G. M. Hampton, L. C. Amler, A. Pirzkall, *et al.*, "Evaluation of circulating tumor cells and circulating tumor dna in non-small cell lung cancer: Association with clinical endpoints in a phase ii clinical trial of pertuzumab and erlotinib," *Clinical Cancer Research*, vol. 18, no. 8, pp. 2391–2401, 2012.
- [28] P. Mirabelli, L. Coppola, and M. Salvatore, "Cancer cell lines are useful model systems for medical research," *Cancers*, vol. 11, no. 8, p. 1098, 2019.
- [29] C. Jin, S. M. McFaul, S. P. Duffy, X. Deng, P. Tavassoli, P. C. Black, and H. Ma, "Technologies for label-free separation of circulating tumor cells: from historical foundations to recent developments," *Lab on a Chip*, vol. 14, no. 1, pp. 32–44, 2014.
- [30] J. G. Moreno, S. M. O'Hara, S. Gross, G. Doyle, H. Fritsche, L. G. Gomella, and L. W. Terstappen, "Changes in circulating carcinoma cells in patients with metastatic prostate cancer correlate with disease status," *Urology*, vol. 58, no. 3, pp. 386–392, 2001.
- [31] H. K. Lin, S. Zheng, A. J. Williams, M. Balic, S. Groshen, H. I. Scher, M. Fleisher, W. Stadler, R. H. Datar, Y.-C. Tai, *et al.*, "Portable filter-based

- microdevice for detection and characterization of circulating tumor cells,” *Clinical Cancer Research*, vol. 16, no. 20, pp. 5011–5018, 2010.
- [32] L. Wang, P. Balasubramanian, A. P. Chen, S. Kummar, Y. A. Evrard, and R. J. Kinders, “Promise and limits of the cellsearch platform for evaluating pharmacodynamics in circulating tumor cells,” in *Seminars in oncology*, vol. 43, pp. 464–475, Elsevier, 2016.
- [33] K. Polyak and R. A. Weinberg, “Transitions between epithelial and mesenchymal states: acquisition of malignant and stem cell traits,” *Nature Reviews Cancer*, vol. 9, no. 4, pp. 265–273, 2009.
- [34] D. R. Gossett, W. M. Weaver, A. J. Mach, S. C. Hur, H. T. K. Tse, W. Lee, H. Amini, and D. Di Carlo, “Label-free cell separation and sorting in microfluidic systems,” *Analytical and bioanalytical chemistry*, vol. 397, no. 8, pp. 3249–3267, 2010.
- [35] S. Seal, “Silicone flotation: A simple quantitative method for the isolation of free-floating cancer cells from the blood,” *Cancer*, vol. 12, no. 3, pp. 590–595, 1959.
- [36] R. Gertler, R. Rosenberg, K. Fuehrer, M. Dahm, H. Nekarda, and J. R. Siewert, “Detection of circulating tumor cells in blood using an optimized density gradient centrifugation,” in *Molecular Staging of Cancer*, pp. 149–155, Springer, 2003.
- [37] T. Scheinin and A. Koivuniemi, “Large benign cells in circulating blood and their significance in the identification of cancer cells,” *cancer*, vol. 15, no. 5, pp. 972–977, 1962.
- [38] S. K. Arya, B. Lim, and A. R. A. Rahman, “Enrichment, detection and clinical significance of circulating tumor cells,” *Lab on a Chip*, vol. 13, no. 11, pp. 1995–2027, 2013.

- [39] A. Alazzam, I. Stiharu, R. Bhat, and A.-N. Meguerditchian, “Interdigitated comb-like electrodes for continuous separation of malignant cells from blood using dielectrophoresis,” *Electrophoresis*, vol. 32, no. 11, pp. 1327–1336, 2011.
- [40] M. Wu, A. Ozcelik, J. Rufo, Z. Wang, R. Fang, and T. J. Huang, “Acoustofluidic separation of cells and particles,” *Microsystems & nanoengineering*, vol. 5, no. 1, pp. 1–18, 2019.
- [41] W. S. Low and W. A. B. Wan Abas, “Benchtop technologies for circulating tumor cells separation based on biophysical properties,” *BioMed research international*, vol. 2015, 2015.
- [42] P. Li, Z. Mao, Z. Peng, L. Zhou, Y. Chen, P.-H. Huang, C. I. Truica, J. J. Drabick, W. S. El-Deiry, M. Dao, *et al.*, “Acoustic separation of circulating tumor cells,” *Proceedings of the National Academy of Sciences*, vol. 112, no. 16, pp. 4970–4975, 2015.
- [43] M. Abkarian, M. Faivre, R. Horton, K. Smistrup, C. A. Best-Popescu, and H. A. Stone, “Cellular-scale hydrodynamics,” *Biomedical materials*, vol. 3, no. 3, p. 034011, 2008.
- [44] B. M. Dincau, A. Aghilinejad, X. Chen, S. Y. Moon, and J.-H. Kim, “Vortex-free high-reynolds deterministic lateral displacement (dld) via airfoil pillars,” *Microfluidics and Nanofluidics*, vol. 22, no. 12, pp. 1–9, 2018.
- [45] H. W. Hou, M. E. Warkiani, B. L. Khoo, Z. R. Li, R. A. Soo, D. S.-W. Tan, W.-T. Lim, J. Han, A. A. S. Bhagat, and C. T. Lim, “Isolation and retrieval of circulating tumor cells using centrifugal forces,” *Scientific reports*, vol. 3, no. 1, pp. 1–8, 2013.
- [46] E. Sollier, D. E. Go, J. Che, D. R. Gossett, S. O’Byrne, W. M. Weaver, N. Kummer, M. Rettig, J. Goldman, N. Nickols, *et al.*, “Size-selective collection of circulating tumor cells using vortex technology,” *Lab on a Chip*, vol. 14, no. 1, pp. 63–77, 2014.

- [47] S. Zheng, H. Lin, J.-Q. Liu, M. Balic, R. Datar, R. J. Cote, and Y.-C. Tai, “Membrane microfilter device for selective capture, electrolysis and genomic analysis of human circulating tumor cells,” *Journal of chromatography A*, vol. 1162, no. 2, pp. 154–161, 2007.
- [48] S. J. Tan, L. Yobas, G. Y. H. Lee, C. N. Ong, and C. T. Lim, “Microdevice for the isolation and enumeration of cancer cells from blood,” *Biomedical microdevices*, vol. 11, no. 4, pp. 883–892, 2009.
- [49] H. Chen, Z. Zhang, and B. Wang, “Size-and deformability-based isolation of circulating tumor cells with microfluidic chips and their applications in clinical studies,” *AIP Advances*, vol. 8, no. 12, p. 120701, 2018.
- [50] H. Mohamed, L. D. McCurdy, D. H. Szarowski, S. Duva, J. N. Turner, and M. Caggana, “Development of a rare cell fractionation device: application for cancer detection,” *IEEE transactions on nanobioscience*, vol. 3, no. 4, pp. 251–256, 2004.
- [51] H. Mohamed, M. Murray, J. N. Turner, and M. Caggana, “Isolation of tumor cells using size and deformation,” *Journal of Chromatography A*, vol. 1216, no. 47, pp. 8289–8295, 2009.
- [52] J. S. Bagnall, S. Byun, S. Begum, D. T. Miyamoto, V. C. Hecht, S. Maheswaran, S. L. Stott, M. Toner, R. O. Hynes, and S. R. Manalis, “Deformability of tumor cells versus blood cells,” *Scientific reports*, vol. 5, no. 1, pp. 1–11, 2015.
- [53] J. P. Beech, S. H. Holm, K. Adolfsson, and J. O. Tegenfeldt, “Sorting cells by size, shape and deformability,” *Lab on a Chip*, vol. 12, no. 6, pp. 1048–1051, 2012.
- [54] S. M. Ahmmed, S. S. Bithi, A. A. Pore, N. Mubtasim, C. Schuster, L. S. Gollahon, and S. A. Vanapalli, “Multi-sample deformability cytometry of cancer cells,” *APL bioengineering*, vol. 2, no. 3, p. 032002, 2018.

- [55] L. Pang, S. Shen, C. Ma, T. Ma, R. Zhang, C. Tian, L. Zhao, W. Liu, and J. Wang, “Deformability and size-based cancer cell separation using an integrated microfluidic device,” *Analyst*, vol. 140, no. 21, pp. 7335–7346, 2015.
- [56] S. Byun, S. Son, D. Amodei, N. Cermak, J. Shaw, J. H. Kang, V. C. Hecht, M. M. Winslow, T. Jacks, P. Mallick, *et al.*, “Characterizing deformability and surface friction of cancer cells,” *Proceedings of the National Academy of Sciences*, vol. 110, no. 19, pp. 7580–7585, 2013.
- [57] H. W. Hou, Q. Li, G. Lee, A. Kumar, C. Ong, and C. T. Lim, “Deformability study of breast cancer cells using microfluidics,” *Biomedical microdevices*, vol. 11, no. 3, pp. 557–564, 2009.
- [58] Q. Guo, S. M. McFaul, and H. Ma, “Deterministic microfluidic ratchet based on the deformation of individual cells,” *Physical Review E*, vol. 83, no. 5, p. 051910, 2011.
- [59] Q. Guo, S. Park, and H. Ma, “Microfluidic micropipette aspiration for measuring the deformability of single cells,” *Lab on a Chip*, vol. 12, no. 15, pp. 2687–2695, 2012.
- [60] Q. Guo, S. P. Duffy, K. Matthews, A. T. Santoso, M. D. Scott, and H. Ma, “Microfluidic analysis of red blood cell deformability,” *Journal of biomechanics*, vol. 47, no. 8, pp. 1767–1776, 2014.
- [61] S. M. McFaul, B. K. Lin, and H. Ma, “Cell separation based on size and deformability using microfluidic funnel ratchets,” *Lab on a chip*, vol. 12, no. 13, pp. 2369–2376, 2012.
- [62] B. K. Lin, S. M. McFaul, C. Jin, P. C. Black, and H. Ma, “Highly selective biomechanical separation of cancer cells from leukocytes using microfluidic ratchets and hydrodynamic concentrator,” *Biomicrofluidics*, vol. 7, no. 3, p. 034114, 2013.
- [63] H. A. Cognart, J.-L. Viovy, and C. Villard, “Fluid shear stress coupled with narrow constrictions induce cell type-dependent morphological and molecular

- changes in sk-br-3 and mda-mb-231 cells,” *Scientific reports*, vol. 10, no. 1, pp. 1–14, 2020.
- [64] J. S. Kuo, Y. Zhao, P. G. Schiro, L. Ng, D. S. Lim, J. P. Shelby, and D. T. Chiu, “Deformability considerations in filtration of biological cells,” *Lab on a Chip*, vol. 10, no. 7, pp. 837–842, 2010.
- [65] J. Hendriks, C. W. Visser, S. Henke, J. Leijten, D. B. Saris, C. Sun, D. Lohse, and M. Karperien, “Optimizing cell viability in droplet-based cell deposition,” *Scientific reports*, vol. 5, no. 1, pp. 1–10, 2015.
- [66] G. Kabacaoğlu and G. Biros, “Optimal design of deterministic lateral displacement device for viscosity-contrast-based cell sorting,” *Physical Review Fluids*, vol. 3, no. 12, p. 124201, 2018.
- [67] H. Li, J. Chen, W. Du, Y. Xia, D. Wang, G. Zhao, and J. Chu, “The optimization of a microfluidic ctc filtering chip by simulation,” *Micromachines*, vol. 8, no. 3, p. 79, 2017.
- [68] M. Aghaamoo, A. Aghilinejad, X. Chen, and J. Xu, “On the design of deterministic dielectrophoresis for continuous separation of circulating tumor cells from peripheral blood cells,” *Electrophoresis*, vol. 40, no. 10, pp. 1486–1493, 2019.
- [69] T. Wu, Q. Guo, H. Ma, and J. J. Feng, “The critical pressure for driving a red blood cell through a contracting microfluidic channel,” *Theoretical and Applied Mechanics Letters*, vol. 5, no. 6, pp. 227–230, 2015.
- [70] M. S. Aljaghtham, Z. L. Liu, J. J. Guo, J. He, and E. Celik, “Numerical simulations of cell flow and trapping within microfluidic channels for stiffness based cell isolation,” *Journal of biomechanics*, vol. 85, pp. 43–49, 2019.
- [71] Z. Zhang, J. Xu, B. Hong, and X. Chen, “The effects of 3d channel geometry on ctc passing pressure—towards deformability-based cancer cell separation,” *Lab on a Chip*, vol. 14, no. 14, pp. 2576–2584, 2014.

- [72] X. Zhang, X. Chen, and H. Tan, “On the thin-film-dominated passing pressure of cancer cell squeezing through a microfluidic ctc chip,” *Microfluidics and Nanofluidics*, vol. 21, no. 9, pp. 1–13, 2017.
- [73] M. Aghaamoo, Z. Zhang, X. Chen, and J. Xu, “Deformability-based circulating tumor cell separation with conical-shaped microfilters: Concept, optimization, and design criteria,” *Biomicrofluidics*, vol. 9, no. 3, p. 034106, 2015.
- [74] G. Bao and S. Suresh, “Cell and molecular mechanics of biological materials,” *Nature materials*, vol. 2, no. 11, pp. 715–725, 2003.
- [75] S. Suresh, “Biomechanics and biophysics of cancer cells,” *Acta Materialia*, vol. 55, no. 12, pp. 3989–4014, 2007.
- [76] E. Evans and A. Yeung, “Apparent viscosity and cortical tension of blood granulocytes determined by micropipet aspiration,” *Biophysical journal*, vol. 56, no. 1, pp. 151–160, 1989.
- [77] M. E. Dokukin, N. V. Guz, and I. Sokolov, “Quantitative study of the elastic modulus of loosely attached cells in afm indentation experiments,” *Biophysical journal*, vol. 104, no. 10, pp. 2123–2131, 2013.
- [78] M.-H. Lee, P.-H. Wu, J. R. Staunton, R. Ros, G. D. Longmore, and D. Wirtz, “Mismatch in mechanical and adhesive properties induces pulsating cancer cell migration in epithelial monolayer,” *Biophysical journal*, vol. 102, no. 12, pp. 2731–2741, 2012.
- [79] Q. Li, G. Y. Lee, C. N. Ong, and C. T. Lim, “Afm indentation study of breast cancer cells,” *Biochemical and biophysical research communications*, vol. 374, no. 4, pp. 609–613, 2008.
- [80] K. Hosseini, A. Taubenberger, C. Werner, and E. Fischer-Friedrich, “Emt-induced cell-mechanical changes enhance mitotic rounding strength,” *Advanced Science*, vol. 7, no. 19, p. 2001276, 2020.

- [81] M. J. Rosenbluth, W. A. Lam, and D. A. Fletcher, “Force microscopy of nonadherent cells: a comparison of leukemia cell deformability,” *Biophysical journal*, vol. 90, no. 8, pp. 2994–3003, 2006.
- [82] M. Lekka, P. Laidler, D. Gil, J. Lekki, Z. Stachura, and A. Hryniewicz, “Elasticity of normal and cancerous human bladder cells studied by scanning force microscopy,” *European Biophysics Journal*, vol. 28, no. 4, pp. 312–316, 1999.
- [83] A. Mohammadalipour, M. M. Burdick, and D. F. Tees, “Deformability of breast cancer cells in correlation with surface markers and cell rolling,” *The FASEB Journal*, vol. 32, no. 4, pp. 1806–1817, 2018.
- [84] D.-H. Lee, X. Li, N. Ma, M. A. Digman, and A. P. Lee, “Rapid and label-free identification of single leukemia cells from blood in a high-density microfluidic trapping array by fluorescence lifetime imaging microscopy,” *Lab on a Chip*, vol. 18, no. 9, pp. 1349–1358, 2018.
- [85] P. R. Gascoyne, X.-B. Wang, Y. Huang, and F. F. Becker, “Dielectrophoretic separation of cancer cells from blood,” *IEEE transactions on industry applications*, vol. 33, no. 3, pp. 670–678, 1997.
- [86] J. An, J. Lee, S. H. Lee, J. Park, and B. Kim, “Separation of malignant human breast cancer epithelial cells from healthy epithelial cells using an advanced dielectrophoresis-activated cell sorter (dacs),” *Analytical and bioanalytical chemistry*, vol. 394, no. 3, pp. 801–809, 2009.
- [87] M. Hosokawa, T. Hayata, Y. Fukuda, A. Arakaki, T. Yoshino, T. Tanaka, and T. Matsunaga, “Size-selective microcavity array for rapid and efficient detection of circulating tumor cells,” *Analytical chemistry*, vol. 82, no. 15, pp. 6629–6635, 2010.
- [88] W. H. Grover, A. K. Bryan, M. Diez-Silva, S. Suresh, J. M. Higgins, and S. R. Manalis, “Measuring single-cell density,” *Proceedings of the National Academy of Sciences*, vol. 108, no. 27, pp. 10992–10996, 2011.

- [89] Y. Zhao, H. S. S. Lai, G. Zhang, G.-B. Lee, and W. J. Li, “Measurement of single leukemia cell’s density and mass using optically induced electric field in a microfluidics chip,” *Biomicrofluidics*, vol. 9, no. 2, p. 022406, 2015.
- [90] R. J. Trudnowski and R. C. Rico, “Specific gravity of blood and plasma at 4 and 37 c,” *Clinical chemistry*, vol. 20, no. 5, pp. 615–616, 1974.
- [91] S. M. Lewis, B. J. Bain, I. Bates, and J. V. Dacie, *Dacie and Lewis practical haematology*. Churchill Livingstone, 2006.
- [92] C. Dong, R. Skalak, and K.-L. P. Sung, “Cytoplasmic rheology of passive neutrophils,” *Biorheology*, vol. 28, no. 6, pp. 557–567, 1991.
- [93] F. A. Coumans, G. Van Dalum, M. Beck, and L. W. Terstappen, “Filtration parameters influencing circulating tumor cell enrichment from whole blood,” *PloS one*, vol. 8, no. 4, p. e61774, 2013.
- [94] D. N. Macklin, N. A. Ruggero, and M. W. Covert, “The future of whole-cell modeling,” *Current opinion in biotechnology*, vol. 28, pp. 111–115, 2014.
- [95] C. Lim, E. Zhou, and S. Quek, “Mechanical models for living cells—a review,” *Journal of biomechanics*, vol. 39, no. 2, pp. 195–216, 2006.
- [96] A. Yeung and E. Evans, “Cortical shell-liquid core model for passive flow of liquid-like spherical cells into micropipets,” *Biophysical journal*, vol. 56, no. 1, pp. 139–149, 1989.
- [97] D. Theret, M. Levesque, M. Sato, R. Nerem, and L. Wheeler, “The application of a homogeneous half-space model in the analysis of endothelial cell micropipette measurements,” 1988.
- [98] M. Sato, D. Theret, L. Wheeler, N. Ohshima, and R. Nerem, “Application of the micropipette technique to the measurement of cultured porcine aortic endothelial cell viscoelastic properties,” 1990.
- [99] G. Bilodeau, “Regular pyramid punch problem,” 1992.

- [100] J. Alcaraz, L. Buscemi, M. Grabulosa, X. Trepas, B. Fabry, R. Farré, and D. Navajas, “Microrheology of human lung epithelial cells measured by atomic force microscopy,” *Biophysical journal*, vol. 84, no. 3, pp. 2071–2079, 2003.
- [101] F. Y. Leong, Q. Li, C. T. Lim, and K.-H. Chiam, “Modeling cell entry into a micro-channel,” *Biomechanics and modeling in mechanobiology*, vol. 10, no. 5, pp. 755–766, 2011.
- [102] Z. Zhang, X. Chen, and J. Xu, “Entry effects of droplet in a micro confinement: Implications for deformation-based circulating tumor cell microfiltration,” *Biomicrofluidics*, vol. 9, no. 2, p. 024108, 2015.
- [103] X. Zhang, M. A. Hashem, X. Chen, and H. Tan, “On passing a non-newtonian circulating tumor cell (ctc) through a deformation-based microfluidic chip,” *Theoretical and Computational Fluid Dynamics*, vol. 32, no. 6, pp. 753–764, 2018.
- [104] J. U. Brackbill, D. B. Kothe, and C. Zemach, “A continuum method for modeling surface tension,” *Journal of computational physics*, vol. 100, no. 2, pp. 335–354, 1992.
- [105] ANSYS Fluent, “Ansys[®].”
- [106] S. Osher and J. A. Sethian, “Fronts propagating with curvature-dependent speed: Algorithms based on hamilton-jacobi formulations,” *Journal of computational physics*, vol. 79, no. 1, pp. 12–49, 1988.
- [107] S. O. Unverdi and G. Tryggvason, “A front-tracking method for viscous, incompressible, multi-fluid flows,” *Journal of computational physics*, vol. 100, no. 1, pp. 25–37, 1992.
- [108] G. Perigaud and R. Saurel, “A compressible flow model with capillary effects,” *Journal of Computational Physics*, vol. 209, no. 1, pp. 139–178, 2005.
- [109] R. K. Shukla, C. Pantano, and J. B. Freund, “An interface capturing method for the simulation of multi-phase compressible flows,” *Journal of Computational Physics*, vol. 229, no. 19, pp. 7411–7439, 2010.

-
- [110] C. W. Hirt and B. D. Nichols, “Volume of fluid (vof) method for the dynamics of free boundaries,” *Journal of computational physics*, vol. 39, no. 1, pp. 201–225, 1981.
- [111] P. J. Roache, “Quantification of uncertainty in computational fluid dynamics,” *Annual review of fluid Mechanics*, vol. 29, no. 1, pp. 123–160, 1997.
- [112] P. J. Roache, “Verification of codes and calculations,” *AIAA journal*, vol. 36, no. 5, pp. 696–702, 1998.
- [113] M. R. A. Khan and A. T. Hasan, “Design and evaluation of generic bump for flow control in a supersonic inlet isolator,” *Journal of Fluids Engineering*, vol. 143, no. 5, p. 051207, 2021.
- [114] S. Hodges, O. Jensen, and J. Rallison, “The motion of a viscous drop through a cylindrical tube,” *Journal of fluid mechanics*, vol. 501, pp. 279–301, 2004.
- [115] Y. Xia, Y. Wan, S. Hao, M. Nisic, R. A. Harouaka, Y. Chen, X. Zou, and S.-Y. Zheng, “Nucleus of circulating tumor cell determines its translocation through biomimetic microconstrictions and its physical enrichment by microfiltration,” *Small*, vol. 14, no. 44, p. 1802899, 2018.